九州大学学術情報リポジトリ
Kyushu University Institutional Repository

High Performance Design of a Contra-Rotating Axial Flow Pump with Different Rotor-Speed Combination

曹, 琳琳

https://doi.org/10.15017/1470594

出版情報：九州大学, 2014, 博士（工学）, 課程博士
バージョン：
権利関係：全文ファイル公表済

2014 Doctor Thesis

High Performance Design of a Contra-Rotating Axial Flow Pump with Different Rotor-Speed Combination

Supervisor: Prof. Watanabe, Satoshi

Cao, Linlin
Mechanical Engineering
Graduate School of Engineering
Kyushu University

Table of Contents

	Nomenclature	**iv**
Chapter 1	**Introduction**	**1**
1.1	Applications of axial flow pumps	1
1.2	Cavitation in pumps	4
1.3	Applications of contra-rotating rotor-rotor combinations	7
1.3.1	Contra-rotating rotors in aerodynamic field	8
1.3.2	Contra-rotating rotors in hydraulic field	10
1.4	Contra-rotating rotors in axial flow pumps	12
1.5	Research outlines	16
Chapter 2	**Performance experiments and numerical simulation approaches**	**19**
2.1	Performance experiment system and relevant measurement devices	19
2.1.1	Overview of performance experiment system	19
2.1.2	Variable speed driving units	22
2.1.3	Rotation speed monitoring	23
2.1.4	Torque measurement	24
2.1.5	Flow rate measurement	24
2.1.6	Pump head rise measurement	26
2.2	Internal flow field measurement	27
2.2.1	Flow measurement by 5-hole probe	27
2.2.2	Calibration of 5-hole probe	30
2.2.3	Pressure measurement devices	32
2.3	Numerical simulation method	33
2.3.1	Computational grid	34
2.3.2	Boundary conditions and domain interface	35
2.3.3	Turbulence model	37
2.3.4	Basic settings of unsteady simulations	37
2.3.5	Performance evaluation with simulation results	38

Chapter 3 Design methodology 40
3.1 Design specifications and hydraulic performances of prototype rotor pair RR2 40
3.1.1 Design specifications of prototype rotor pair RR2 40
3.1.2 Hydraulic performances of prototype rotor pair RR2 43
3.1.3 Internal flow structures of prototype rotor pair RR2 44
3.1.4 Pressure distribution properties of RR2 rotor pair 47
3.2 Different-speed design methodology 49
3.2.1 Determination of rotation speed combination 49
3.2.2 Inflow velocity profiles for RR3 rear rotor 53
3.2.3 Determination of relevant flow angles 56
3.2.4 Determination of profile geometries 57
3.3 Preliminary models for new rear rotor RR3 59
3.3.1 Geometries of three types of new rear rotors 59
3.3.2 Hydraulic performance investigation for three types of new rear rotors 61
3.3.3 Evaluation of cavitation performances by $NPSH_r$ 62
3.3.4 Cavitation simulations with two-phase flow model 65
3.4 Summary 66

Chapter 4 Performance investigation for new contra-rotating rotors 67
4.1 Hydraulic performances of new rotor pair RR3 67
4.2 Internal flow structures of new rotor pair RR3 71
4.2.1 Radial distributions of axial velocity at rear rotor inlet section 71
4.2.2 Radial distributions of circumferential velocity at rear rotor inlet section 73
4.2.3 Flow distributions at rear rotor outlet section 74
4.3 Boundary layer investigation 76
4.3.1 Limiting streamline observation by multi-color oil-film method 76
4.3.2 Limiting streamlines of front rotor at low flow rate 78
4.3.3 Limiting streamlines of RR3 rear rotor at low flow rate 80
4.3.4 Tip leakage vortices obtained by numerical simulations 84
4.4 Summary 88

Chapter 5 Rotor-rotor interactions in new contra-rotating rotors 89
5.1 Casing wall static pressure measurements 89
5.1.1 Overview of casing wall pressure measurement experiments 89
5.1.2 Pressure fluctuation measurement (PFTM) 92
5.1.3 Pressure field measurement (PFEM) 93
5.1.4 Correlation analysis 97
5.2 Prediction of frequency modes associated with rotor-rotor interactions 98
5.2.1 Derivation of frequency modes associated with rotor-rotor interactions 99
5.2.2 Predicted pressure modes for two rotation speed combinations 101
5.3 Blade passing frequency (BPF) distribution for both rotor pairs in axial direction 102
5.4 Correlation analyses on pressure data obtained at various peripheral locations 103
5.4.1 Correlation analyses results at design condition 103
5.4.2 Correlation analyses results at partial flow rate 108
5.5 Blade-to-blade pressure distribution in both rotor pairs 112
5.5.1 Pressure distributions in both rotor pairs at design condition 112
5.5.2 Pressure distributions in both rotor pairs at partial flow rate 114
5.6 Extractions of blade loading curves 117
5.7 Summary 122

Chapter 6 Conclusions 124

Acknowledgement 128

References 130

List of publications in journals/conference proceedings 137

Nomenclature

a	=	Amplitude of pressure mode [m]
C_p	=	Pressure coefficient [-]
$C(\delta)$	=	Orientation coefficients for 5-hole probe [-]
$Coh^2(f)$	=	Spectral coherence [-]
D	=	Diameter [m]
f	=	Frequency [Hz]
f_s	=	Pressure measurement sampling frequency [Hz]
$f(\delta)$	=	Calibration coefficients for 5-hole probe [-]
F	=	Blade number of front rotor [-]
H	=	Hydraulic head [m]
H_{th}	=	Theoretical Euler head [m]
i	=	Incidence angle [°]
m	=	Pressure mode [-]
n_s	=	Number of sampling data [-]
n_m	=	Experiment number [-]
N	=	Rotational speed [min^{-1}]
N_s	=	Specific speed [min^{-1}, m^3/min, m]
$NPSH_3$	=	Net positive suction head at 3% head drop [m]
$NPSH_r$	=	Required net positive suction head [m]
$NPSH_a$	=	Available net positive suction head [m]
p	=	Pressure [Pa]
p_{in}	=	Pressure at pump inlet [Pa]
P_v	=	Atmosphere [Pa]
P_{min}	=	Minimum pressure on the rotor blade [Pa]
$P(f)$	=	Pressure spectrum [-]
Q	=	Volumetric flow rate [L/s]
$Q(f)$	=	Phase angle of cross spectrum [-]
r	=	Radius [m]
R	=	Blade number of rear rotor [-]
$S(f)$	=	Cross spectrum [-]

T	=	Torque [N·m]
Δt	=	Time interval, or timestep in simulation [s]
U	=	Peripheral velocity $\omega * r$ [m/s]
V	=	Absolute velocity [m/s]
V_z	=	Axial velocity in absolute frame [m/s]
V_θ	=	Circumferential velocity in absolute frame [m/s]
W	=	Relative velocity [m/s]
x/l	=	Normalized coordinate along the chord [-]
x_f/l	=	The maximum camber location to chord length [-]

Greek

α	=	Attack angle, or orientation angle for 5-hole probe [°]
β	=	Relative flow angle [°]
β_b	=	Blade profile angle [°]
γ	=	Stagger angle [°], or specific weight $\rho * g$ [N/m^3]
λ	=	Profile coefficient, or power coefficient [-]
δ	=	Deviation angle, or orientation angle for 5-hole probe [°]
σ	=	Cavitation number, or cascade solidity [-]
σ_i	=	Cavitation inception number [-]
$\Delta\theta$	=	Relative peripheral positions of rotors [rad]
θ	=	Circumferential location [rad], or orientation angle for 5-hole probe [°]
Ω	=	Angular speed of rotor [rad/s]
ω_F	=	Angular speed of front rotor [rad/s]
ω_R	=	Angular speed of rear rotor [rad/s]
η	=	Hydraulic efficiency [-]
ϕ	=	Flow coefficient [-]
ψ	=	Head coefficient [-]

Subscripts

0	=	At moment for trigger
1	=	At inlet

2	=	At outlet
c	=	Casing wall
d	=	Design condition
f	=	Front rotor
h	=	Hub
$loss$	=	Loss
L	=	At leading edge
r	=	Rear rotor
s	=	Static, or sampling
RS	=	Rotor-stator combination
RR	=	Rotor-rotor combination
t	=	Tip

1 Introduction

Turbomachinery constitutes a large class of machines which could be found all everywhere in our civilized world [1]. With the significance of energy transfer between a continuous stream of fluid and a rotating element, the turbomachines have long been acknowledged to be essential and indispensable in both the industrial field and the civilized society [2, 3].

Such machines are most commonly categorized into two groups by function: the ones which absorb power to increase the fluid pressure or head as fans, pumps and compressors, and the others which generate power by expanding fluid to a lower pressure or a lower head as hydraulic, steam and gas turbines [2, 4]. Besides that, those machines are also classified according to the properties of the flow path. The turbomachines in which fluid moves through the passages in shaft axial direction with no radial movement are called axial flow machines whereas if the flow streamlines are essentially radial, they are called centrifugal machines.

In the present thesis, I concentrate on the hydraulic performances of a kind of novel axial flow pump with the contra-rotating rotors applied, thus the several key concepts relevant to this topic are introduced in the following sections.

1.1 Applications of axial flow pumps

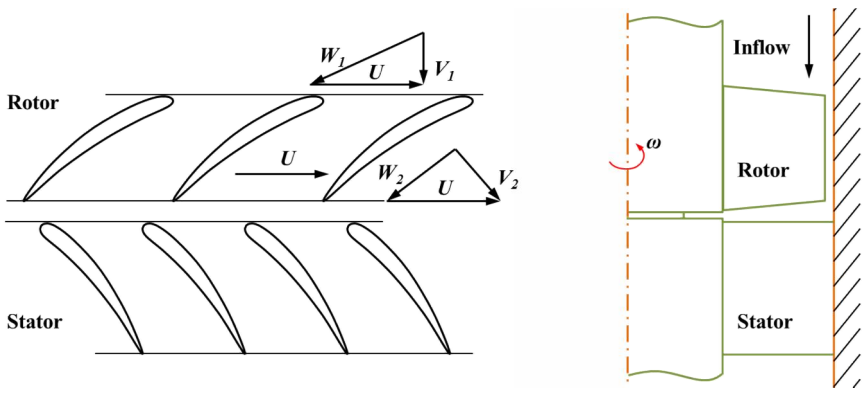

Fig. 1-1 Schematic drawing of axial flow pump

In the present thesis, the studies are primarily carried out on the axial flow pump with incompressible working fluid - water. As shown in Fig. 1-1, in this type of pump, the flow is assumed to be passing through the passages parallel to the rotating axis of the machine under the design condition, and the flow area for both inlet and outlet sections are commonly designed to be equal. The blade rows could be cylindrically developed into a linear cascade, and the pressure of liquid continuously develops during flowing over the airfoil profiles of the rotor blades [3, 5].

As an index to flow path shape for turbomachines, the specific speed N_s defined as

$$N_s = \frac{N\sqrt{Q}}{H^{3/4}} \text{ [min}^{-1}\text{, m}^3\text{/min, m]} \tag{1-1}$$

typically reflects the relationships between their overall performances and global geometries, where N denotes the rated rotation speed [min^{-1}], Q and H respectively the volume flow rate [m^3/min] and the hydraulic head rise [m] at the design condition. As shown in Fig. 1-2, the various families of pumps appear with their typical specific speed options. The appropriate flow path turns to be more axial as the specific speed increases [2, 5].

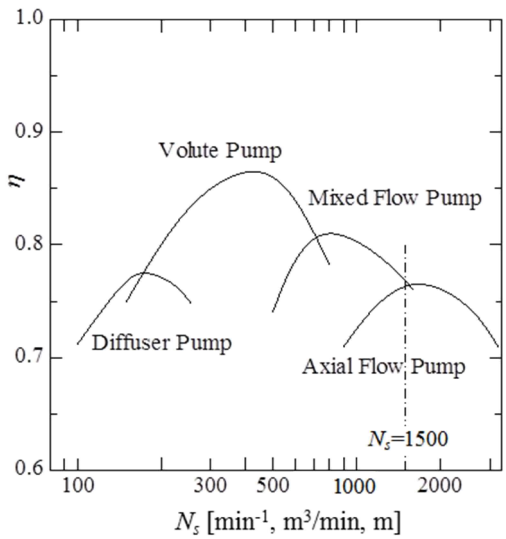

Fig. 1-2 Maximum efficiencies for various kinds of pumps

It could be easily seen that, the centrifugal pumps, which primarily take advantage of the centrifugal force effect, are more appropriate to be specified with relatively low specific speeds. In contrast, the axial flow pumps are more favorable to be designed with high specific speeds, as well as working with low head rise at relatively high flow rate, and therefore usually appear with compact structure [5]. Due to their superiorities of pumping liquid at relatively high flow rates, the axial flow pumps are significantly popular in handling drainage and irrigation for civil, industrial and commercial uses in the global world.

Besides their most common applications in the forestry and agricultural irrigation, the axial flow pumps have also been widely employed in other hydraulic engineering fields due to their strong capacity in water supplies. Toetz D. W. [6], Lawson R. and Anderson, M. A. [7], and others respectively mentioned the artificial destratification system for optimizing water mixing in various lakes with the application of axial flow pumps. In China, a great number of large-size axial flow pumps have been playing significant roles in numerous extraordinarily huge hydraulic projects, as the South-to-North Water Transfer Project [8, 9].

The axial flow pumps are also used in many fields other than for water supplies. In the marine field, the axial flow pumps of rotor-stator combination have been widely employed in various vessels to create a jet of water for propulsion [10, 11]. And due to their compact structure and superior capacities to pump large masses of liquid, they are also universally tasked as the cooling pumps, the circulation pumps in power plants, chemical industry, and other related industrial fields. With the advances of medical researches, the axial flow pumps of extraordinarily small size have been increasingly developed for the human heart assisting devices as the implantable blood pumps [12, 13].

1.2 Cavitation in pumps

As a typical phenomenon in the hydraulic machines, cavitation is defined as the appearance of the vapor bubbles in the flow regions with sufficiently low pressure [1-5]. The inception and development of cavities are rather unstable and complicated processes influenced by several elements, such as cavitation nuclei level, boundary roughness condition, environmental pressure, and even flow turbulence [5].

Figure 1-3 gives the noncavitating performance curve and the suction performance curve of a typical pump [5]. Usually, the pump's overall performances are still capable to remain on a reasonable level at the moment when the cavitation inception occurs as shown in Fig. 1-3 (b). With the pertinent development of cavitation, a large number of bubbles are conveyed with streams, which would induce great flow instabilities by growing with the reduced surrounding pressure and subsequent collapse in the higher pressure region downstream. The unstable collapse of cavitation bubbles would externally result in the significantly intense noises and vibrations of the machine. And internally, the machine solid surfaces might be severely damaged by the extremely high velocities, pressures, and temperatures resulted from the collapse process [14, 15]. In addition, the 'attached cavitation' formed by a large number of vapor bubbles adhere on the rotor blades, significantly deteriorate the pressure distribution on the blade surfaces, pertinently impacting on the blade loading and therefore the overall performances of the machine.

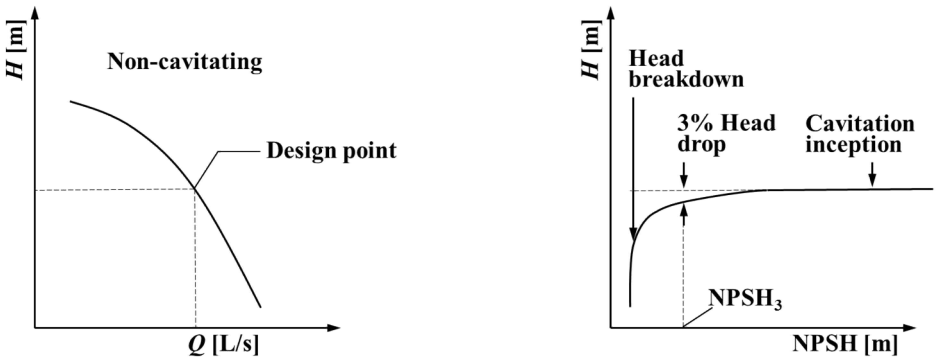

(a) Non-cavitating performance curve (b) Drop curve under cavitating

Fig. 1-3 Schematic of noncavitating performance and cavitating performance

To discuss the cavitation performances of the various kinds of pumps, two dimensionless parameters named as cavitation number σ and cavitation inception number σ_i respectively are given by

$$\sigma = \frac{(P_1 - P_v)}{\rho U_t^2/2} \tag{1-2}$$

$$\sigma_i = \frac{(P_1 - P_{min})}{\rho U_t^2/2} \tag{1-3}$$

where P_1 is defined as the averaged static pressure at the pump inlet, P_v as the vapor pressure, $P_{\min}$ as the minimum pressure on the rotor blade, and U_t as the peripheral velocity of the blade tip $\omega * r_t$ [5]. It could be seen that the cavitation number σ reflects the cavitation potential of the pump under certain inlet static pressure P_1, while the cavitation inception number σ_i evaluates the inherent cavitation properties of the pump system.

In addition, another two essential parameters the Available Net Positive Suction Head ($NPSH_a$) [m] and the Required Net Positive Suction Head ($NPSH_r$) [m] [2] are introduced as

$$\mathrm{NPSH}_a = \frac{P_1}{\rho g} + \frac{{V_1}^2}{2g} - \frac{P_v}{\rho g} \tag{1-4}$$

$$\mathrm{NPSH}_r = \lambda_1 \frac{{V_L}^2}{2g} + \lambda_2 \frac{{W_L}^2}{2g} \tag{1-5}$$

where V_1 denotes the absolute velocity at the pump inlet, V_L and W_L are specified as the absolute and the relative velocities at the impeller entrance location 'L' as shown in Fig. 1-4, λ_1 and λ_2 as the coefficients determined by the suction pipe line losses and the blade profile respectively.

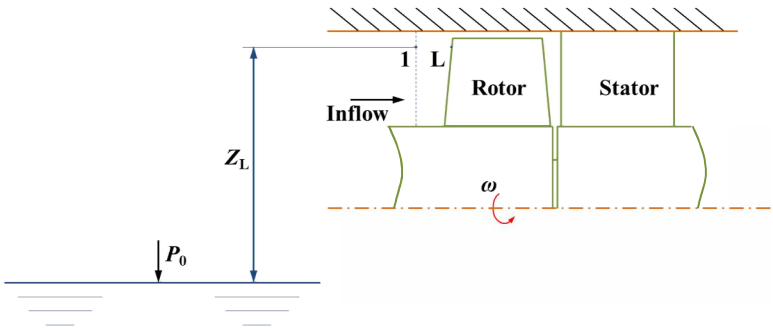

Fig. 1-4 Schematic description of Net Positive Suction Head

Instead of the cavitation number σ, $\mathrm{NPSH_a}$ is often employed in turbomachines to describe the cavitation potential under certain ambient pressure as well as the cavitation margin offered by the environment. In contrast, as the cavitation inception number σ_i, $\mathrm{NPSH_r}$ demonstrates the static pressure reduction level along the blade profile, and the least static pressure margin above the vapor pressure at the blade rows inlet to avoid cavitation. Hence, it is clear that $\mathrm{NPSH_a}$ must be kept on a level beyond $\mathrm{NPSH_r}$ to protect a pump from cavitation, while the value of $\mathrm{NPSH_r}$ appears rather difficult to be estimated as a geometric property of blade profile. Universally $\mathrm{NPSH_3}$, obtained from the pump cavitation experiments as the NPSH available corresponding to three percent head drop from the noncavitating head as marked in Fig. 1-3 (b), is adopted as the critical cavitation margin instead of $\mathrm{NPSH_r}$ [1-5].

1.3 Applications of contra-rotating rotor-rotor combinations

The application of contra-rotating rotor-rotor combination in the rotating machinery has been increasingly discussed in both the hydraulic and the aerodynamic fields, and numerous researchers have mentioned it as a promising solution to energy conservation, performance optimization as well as machine size compacting [16-18].

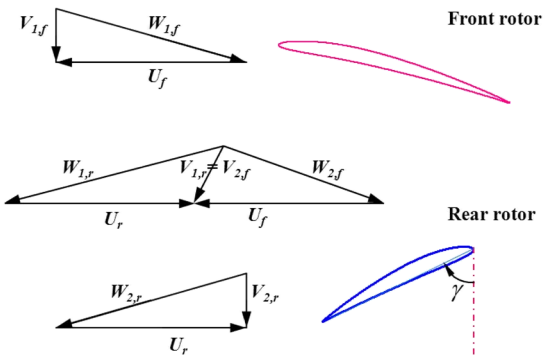

Fig. 1-5 Velocity triangles in contra-rotating rotor pairs for pumps

The representative velocity triangles in the contra-rotating rotor-rotor combination for pumps are schematically shown in Fig. 1-5, where U, V, W denote peripheral speed of rotors, absolute and relative velocities of fluid respectively, and the subscripts 1, 2 stands for the positions of inlet and outlet. It can be seen that with the outlet swirl velocity of the upstream front rotor converted into additional head rise by the downstream rear rotor, both of tandem rotors in this combination are tasked with comparable loading. Compared with the traditional rotor-stator type in which only single rotor contributes to power transmission, this combination offers the remarkably reduced machine dimension both in radial and axial directions under the same design specification. And the each rotor is capable to be designed with reduced structural strength since the overall loading is comparably shared.

1.3.1 Contra-rotating rotors in aerodynamic field

In the aviation industry, the contra-rotating rotors appeared in the aircraft engine system as compressors, propfans and turbofans decades ago. Such engine systems with the contra-rotating rotors applied showed rather complicated structures, but had been proved with a significantly increased bypass ratio and propulsive efficiency, offering a promising resolution in terms of fuel consumption reduction [19-23]. In the 1990s, Sharma, P. B. et al. parametrically investigated the aeroacoustic, aerodynamic and other related performances of a low speed contra-rotating axial flow compressor stage by the experimental approaches [19-21]. They highlighted that a contra-rotating compressor stage with an optimum speed ratio provided a high through-flow capacity, and moreover a wider stall-free operation range as well as fairly improved off-design performances, and they also identified several key factors which affect the aeroacoustic and aerodynamic performances in the contra-rotating compressor stage. Latterly, the numerical technology was increasingly employed in the studies on the internal flow of contra-rotating compressor, and various unsteady simulation methods were demanded due to the inherently unsteady blade-to-blade flow field characterized by such two oppositely rotating rotors. Chen, Y. Y. et al. investigated how the certain rotor parameters affected the performance of a contra-rotating axial flow compressor by the numerical approaches, which offered the results well agreed with their experimental data [22]. Knapke, R. D. et al. presented a three dimensional time accurate simulation for a contra-rotating aspirated compressor by a commercial CFD (Computational Fluid Dynamics) solver FINE^{TM} TURBO, which made its internal flow structures better understood, and further discussed the superior stall margin in the contra-rotating type compressors [23].

As mentioned above, driven by the corresponding contra-rotating compressors and turbines, the contra-rotating propfans were proved with considerably high bypass ratio and propulsive

efficiency compared with the traditional single rotating type due to their swirl-free exit flow condition [24-26]. Besides that, such type of propfans were also widely required due to their highlights of better power partitioning, optimum off-design condition, and reversible thrust [24]. Plenty of pertinent studies in their performances could be found in last decades, and most of them concentrated on the significant interactions and other related flow properties induced by two oppositely rotating blade rows. Such researches of the aeroacoustic performances and aerodynamic interference on this type of rotor-rotor combination has been well developed based on the studies of Hubbard, H. H., who pioneered the counter-rotation propeller noise analysis and recognized the major interference mechanisms in the 1940s [27]. Hanson, D. B. pertinently carried out the theoretical analysis and prediction for the noise generated from contra-rotating propellers [26]. In his researches, the general waveform formulas considering all the noise and loading harmonics due to the contra-rotating rotors were raised, by which the fluctuation modes associated with the rotor-rotor interactions and their corresponding frequencies were recognized, and he moreover emphasized that the acoustic and aerodynamic interferences must be treated separately due to their inherently different mechanisms. Woodward, R. P. experimentally investigated the noise generation from various unsteady aerodynamic phenomenon in two high-speed contra-rotating propellers under various operating conditions, and analysed the rotor-rotor interaction by the acoustic modes associated with the Blade Passing Frequency (BPF) of both rotors [28, 29]. With the numerical technology of Computational Fluid Dynamics (CFD) and computational aeroacoustics (CAA) coupled, the parametrical study becomes more practical to investigate the rotor-rotor interaction with various mechanisms and their individual contribution to the contra-rotating propeller noise, by which plenty of optimization concepts in both acoustic and aerodynamic performances were raised and validated [30-32].

Generally, confirmed with high bypass ratio and propulsive efficiency, the contra-rotating

type aircraft propeller system still shows the limited application due to the relatively intense noise as well as various rotor-rotor interactions. According to the researches cited above [24-33], for such passage flow field with high relative Mach number, these interactions are dominated by: 1) the interference between front rotor's viscous wakes and rear rotor, 2) the interaction between front rotor's tip vortices and rear rotor, and 3) the influence on front rotor from the shockwave originated at the leading edge of rear rotor.

In contrast, the contra-rotating rotor-rotor combination in subsonic application appears with an incompressible flow field, free of shock and the relative low rotor interaction. As the cooling or ventilation approaches, it becomes increasingly favourable due to the compact structure, and has been proved with rather wide high efficiency range compared with the rotor-stator type under the same design specification [16, 34, 35].

1.3.2 Contra-rotating rotors in hydraulic field

In contrast to those applied in the aerodynamic field, the contra-rotating rotors appear with a relatively narrower application and quite different design considerations in the hydraulic field.

In the marine industry, they have been adapted in the propulsion systems for various vessels. Compared with the aircraft propellers, the unshrouded ship propellers give the incompressible flow field with relatively low velocity, for which the researches are more concentrated in their hydraulic and cavitation performances rather than acoustic performances. With the fundamental benefits of efficient usage of outflow energy, lower loading for individual blade, etc., the contra-rotating rotor-rotor combination is moreover supposed to have superior cavitation performance, since the rotation speed of the individual rotor is well reduced compared with the traditional type under the same overall design specification. In ref. [36], Chen, B. Y. –H. and Reed, A. M. offered a brief review on the development of contra-rotating ship propeller design, and

highlighted its several advantages over the single screw ship propellers: energy recovery, high efficiency, smaller optimum diameter, lower blade loading, torque balance, and optimized cavitation performances.

The contra-rotating ship propellers were primarily designed on the basis of the empirical methods for the traditional single rotor propellers. The two tandem propellers were separately designed with the ideal loading distribution specified, and the interference between them were neglected. In the 1970s, Van Gunsteren, L. A. developed a contra-rotating propeller design method considering the interaction effects between the two oppositely rotating rotors, in which the mutually induced velocity components and pressure variation were introduced [37]. Based on that, Caster, E. B. and LaFone, T. A. proposed an advanced design program, in which the circulation distribution and other design inputs of the forward and aft propellers were no longer identically specified, and a more sophisticated calculation model for the mutually induced velocities was incorporated [38]. Later, plenty of optimized design methods were consecutively proposed with further developed computation concepts for the interaction effects, and the more detailed flow features (such as cavitation, hub effects) were also concerned in those design systems [18, 39-41]. In general, the design methodology of contra-rotating type propeller experienced a gradual transformation from the classic theories for the single rotating propeller. As the design inputs, the distributions of related parameters are respectively specified for the two propellers, with the great concerns of the influences induced by each other.

In recent decades, the concept of contra-rotating axial flow pump was raised and discussed as a promising resolution for the industrial fields in which the pumps of high specific speed and compact structure are required. With the fundamental benefits of the contra-rotating rotor, this type of axial flow pump was confirmed to have more stable performance curves and wider high efficiency operation range by the experimental approaches [42, 43], and was also proved to have

relatively reinforced blade row interaction [44, 45] as discussed in all above applications of the contra-rotating rotor-rotor combination.

Since the application of the contra-rotating rotor pair in the axial flow pump is primarily studied in the present research, the brief status is given in the next sections.

1.4 Contra-rotating rotors in axial flow pumps

The energy recycling and structure compacting have been repeatedly emphasized as the highlights of the contra-rotating rotor-rotor combination. For axial flow pumps, Furukawa, A. et al. theoretically compared the fundamental performance characteristics of the conventional axial flow pump and the contra-rotating type [45].

The theoretical hydraulic Head H_{th} (Euler Head) of axial rotors on the cylindrical surface of diameter D are presented as follows,

$$H_{th,RS} = K_1 {D_{RS}}^2 {N_{RS}}^2 (1 - \frac{K_2 Q \tan\beta_{2,RS}}{{D_{RS}}^3 N_{RS}}) \tag{1-6}$$

$$H_{th,RR} = K_1 {D_{RS}}^2 {N_{RS}}^2 \left\{ 3 \frac{{D_{RR}}^2 {N_{RR}}^2}{{D_{RS}}^2 {N_{RS}}^2} \left[1 - \frac{K_2 Q}{{D_{RR}}^3 N_{RR}} \left(\frac{2\tan\beta_{2,f}}{3} + \frac{\tan\beta_{2,r}}{3} \right) \right] \right\} \tag{1-7}$$

where the subscripts RS and RR respectively denote the conventional rotor-stator and the contra-rotating type, f and r denote the front and rear rotors in the contra-rotating type. In addition, β_2 is defined as the relative flow angle at outlet, and the coefficients K_1 and K_2 as constant values. Moreover, the both rotors in the contra-rotating axial flow pump are specified with the equal rotation speed of N_{RR} there.

For two types of axial flow pumps, given the identical design specifications of $H_{th,RS} = H_{th,RR}$ at the design flow rate Q_d, the following two expressions are derived:

$$\frac{D_{RR}N_{RR}}{D_{RS}N_{RS}} = \frac{1}{\sqrt{3}} \tag{1-8}$$

$$\left(\frac{D_{RS}}{D_{RR}}\right)^2 \left(\frac{2\tan\beta_{2,f}}{3\tan\beta_{2,RS}} + \frac{\tan\beta_{2,r}}{3\tan\beta_{2,RS}}\right) = \frac{1}{\sqrt{3}} \tag{1-9}$$

Equation (1-8) offers a quantitative relation between the two types of axial flow pump, from which it is easy to conclude that either the rotation speed N_{RR} or the rotor diameter D_{RR} could be reduced to obtain the equivalent head rise in the contra-rotating axial flow pump. And as described by Eq. (1-9), the relative outflow angle β_2 for two contra-rotating rotors are also linked with the rotor diameter and the corresponding angle in the single rotor case. The reduction in either of these two parameters (N_{RR} and D_{RR}) would result in decreased rotor peripheral velocity U and in turn decreased relative velocity W as illustrated previously in Fig. 1-5. Combining the definition of $NPSH_r$ in Eq. (1-5), the contra-rotating axial flow pump is expected to be superior in the cavitation performance, since a much lower $NPSH_r$ is acquired under the comparable design specification.

Moreover, in the conventional axial flow pump, the stator is commonly designed with a rather large length, to make the water flow smoothly turn to the desired direction as well as to minimize losses during the flow turning in it. Replacing the stator, the rotating rear rotor is supposed to take a well reduced axial length [42], realizing the remarkable compact space in both radial and axial directions for the contra-rotating rotor pair.

Additionally, the theoretical head rise of the contra-rotating axial flow pump at the full flow rate range could also been derived as,

$$H_{th,RR} = K_1 {D_{RS}}^2 {N_{RS}}^2 \left[\left(1 - \frac{K_2 Q \tan\beta_{2,RS}}{{D_{RS}}^3 N_{RS}}\right) + 3\left(\frac{D_{RR}N_{RR}}{D_{RS}N_{RS}}\right)^2 \left(1 - \frac{Q}{Q_d}\right)\right] \tag{1-10}$$

Compared with the rotor-stator combination with the theoretical performance curve expressed by Eq. (1-6), the contra-rotating rotor pair inherently shows a steeper negative slope on its performance curve (Q-H curve) as described by Eq. (1-10), which was supposed to be rather favorable in terms of the operation stability of whole pumping system [4, 5]. And in ref. [42-45], this performance curve characteristic has been confirmed by numerous experiments on the prototype contra-rotating rotors.

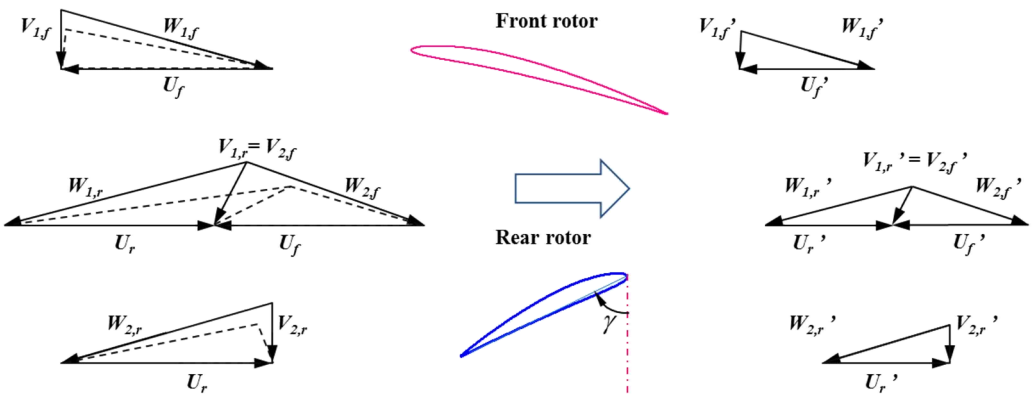

Fig. 1-6 Velocity triangles at off-design condition with RSC

With the contra-rotating rotors driven by independent motors, the contra-rotating axial flow pump presents another highlight in the individual rotation speed control (RSC) for the two rotors at the off-design condition [46]. As shown by the left-hand side part in Fig. 1-6, the reduced flow rate results in the deviated velocity triangles, and the nonzero flow swirl appears at the rear rotor outlet. The inflow condition of the rear rotor is remarkably influenced by the flow rate variation, which indicates the increased shock losses and consequently the reduced efficiency. With the appropriate individual RSC for the two rotors, the velocity triangles at the corresponding flow rate are supposed to adjust to the optimized status as shown in the right-hand side part of Fig. 1-6. Consequently, the overall pump efficiency is in turn expected to be well improved with the realization of no swirl outflow as well as the velocity triangles

resembling those at the design flow rate. In ref. [46], Momosaki, S. et al. experimentally confirmed the improvement of the pump overall efficiency with RSC applied at the partial flow rates, but the flow similitude in terms of rotor speed was proved partly available to explain the variation of the performance and velocity distributions.

While, as previously addressed in the other applications of contra-rotating rotors, the blade row interaction in this type of axial flow pump also appeared to be relatively severe over the rotor-stator interaction in the traditional type [44-47]. In the contra-rotating axial flow pump designed with equal rotation speed ($N_f = N_r$) for both front and rear rotors, the flow pattern around the rotor-rotor interface was confirmed to be rather complicated with several large scale flow recirculation by both the experimental and simulation approaches [47, 48]. The blade-to-blade distribution of static pressure (P_s) was found to be highly unsteady especially at the partial flow rate, and the low pressure regions of the rear rotor seriously impacted on the high pressure regions of the front rotor [44].

Due to the limitation of the experiment systems, Furukawa, A. et al. investigated the cavitation inception in both types of axial flow pumps by adjusting the operation condition rather than reducing the ambient pressure [42]. The photos in Fig. 1-7 were taken after the cavitation inception occurred in two axial flow pumps at the partial flow rate $Q = 20\%Q_d$, where Q_d denotes the design flow rate of each pump.

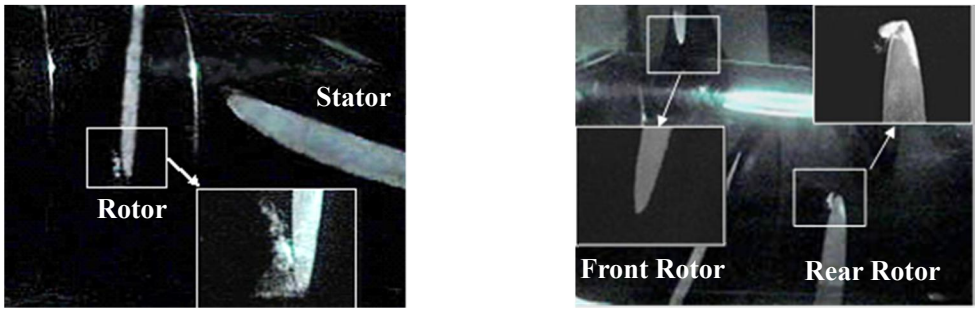

(a) Rotor-Stator type at $Q = 20\%Q_d$ (b) Rotor-Rotor type at $Q = 20\%Q_d$

Fig. 1-7 Cavitation inception in two types of axial flow pump at the off design condition

It has been discussed in the previous section 1.2, that the cavitation inception was supposed to occur around the rotor blade leading edge at the pump inlet side as observed in the rotor-stator type pump (Fig. 1-7 (a)), since the static pressure there fell to the minimum value. Nevertheless, in the contra-rotating axial flow pump as shown in Fig. 1-7 (b), the cavitation was unexpectedly found at the leading edge of the rear rotor, where it was thought to have the well raised static pressure after the flow developed through the front rotor cascade. This was majorly due to higher relative inflow for the rear rotor as can be seen from Fig. 1-6, but was partly ascribed to the great static pressure reducing in the gap between the front rotor's trailing edge and the rear rotor's leading edge, as one of the consequences lead by the significant blade-to-blade potential interaction. It implied a remarkable efficiency deficit of the rear rotor, and was quite deviated from the design expectation of the continuous head rising in the contra-rotating rotor pair.

1.5 Research outlines

From all the findings discussed in above sections, it can be understood that for the contra-rotating rotors, the theoretical advantages of energy recovery are usually accompanied with the complex internal flow structures and the significantly enhanced blade rows interactions. To enlarge the benefits of this type of rotor-rotor combination, more careful design for the relevant parameters is imperative. As mentioned in Sec. 1.3, plenty of researchers have been concentrating on the parametrical studies on the contra-rotating rotors in their specific fields, and most of them pointed out the significance of the speed ratio in improving their rotor pairs' performances.

In the axial flow pump field, based on the theoretical analyses and the investigations (by experiment and CFD) on the prototype contra-rotating axial flow pump reported before, the

work division as well as the rotor speed combination is also considered as the very important and decisive parameters to the contra-rotating rotors' performances.

Hence, the present thesis primarily discusses the possibilities to improve the hydraulic performances of the contra-rotating axial flow pump by rearranging the work division as well as the rotation speed combination in the contra-rotating rotor pair. In the following chapters all of the contents focus on such concept. They elaborate the determination method for the new speed combination, the detailed considerations in the new rear rotor design, the subsequent performances testing results of the new rotor pair, and the pertinent investigations on its internal flow structures and pressure distributions, which are briefly described as follows:

In Chapter 2, a full overview of the performance experiment system and CFD simulations will be given. An introduction of the testing system and related measurement technology for the pump performance experiments is firstly presented. Then the internal flow field investigation method using the major velocity measuring tool the 5-hole probe is introduced with its key parameters. The CFD method is finally described in detail with some key arguments and simulation models.

In Chapter 3, the design specifications of the second generation prototype contra-rotating rotors (herein named RR2 pair), designed in Flow Control Systems Laboratory of Kyushu University [42, 45], are firstly presented. The hydraulic performances, the internal flow properties as well as its pressure distributions are then discussed. Combining with the findings in RR2, the different-speed design method is proposed in expectation of the improved hydraulic performances of the contra-rotating rotors, and in this concept the rotation speed combination of the two rotors is determined based on the reduced cavitation parameter $NPSH_r$ for the rear rotor. Relying on such design idea and several other considerations about the rotor blade profile geometries, the rear rotor is then redesigned with the reduced head rise and rotation speed. To

preliminarily validate such design idea, three types of RR3 rear rotors were proposed and then their performances are investigated by the numerical simulation approaches.

In Chapter 4, the investigations into the hydraulic performances of the newly designed contra-rotating rotor pair RR3, are carried out by both experimental and CFD approaches. In addition to the performance evaluation, the discussion is made on the flow physics behind the improved or degraded performance using measured and simulated flow fields.

In Chapter 5, the rotor-rotor interactions, which often become the sources of noises and vibrations, are investigated in the newly designed contra-rotating rotor pair. As the major experimental approaches in the blade rows interaction investigations, the casing wall static pressure measurement methods are firstly introduced. Then, the axial distributions of the Blade Passing Frequency (BPF) in two types of contra-rotating rotor pairs are presented, and moreover the pressure fluctuation modes with the frequencies both synchronous and non-synchronous to the BPF components are discussed. Finally, by transferring the casing wall pressure data sampled in time domain into space domain, the ensemble averaged blade-to-blade pressure distributions at the blade tip of two contra-rotating rotors are studied, and the associated blade loading curves are presented.

Finally, the conclusions from the present researches about the contra-rotating axial flow pump with different-speed rotors are given in Chapter 6.

2 Performance experiments and numerical simulation approaches

This chapter primarily aims at introducing the testing system for the pump performance experiments. The testing system for the pump performance experiments and the related measurement devices are firstly presented here. Then the internal flow field investigation method is given, and as the major velocity measuring tool the 5-hole probe is introduced with its key parameters. The CFD (Computational Fluid Dynamics) method is finally described in detail with some key arguments and simulation models. The other important experimental approaches such as the casing wall pressure measurement, limiting streamline visualization will be respectively described in the corresponding chapters, where they are used.

2.1 Performance experiment system and relevant measurement devices

2.1.1 Overview of performance experiment system

The testing system for the pump performance experiment is schematically described in Fig. 2-1. The water is supplied to the test contra-rotating axial flow pump from an underground water reservoir by a centrifugal boost pump which is not sketched here, and eventually returns back into the same reservoir. The flow rate is measured by an orifice flow meter installed far upstream of the test pump to keep the inflow to the pump undisturbed. The flow rate (from 10% to 120% of design flow rate Q_d) is adjusted by the appropriate opening of the flow control valve installed far downstream of the test pump outlet.

A concentric shaft structure enables the two contra-rotating rotors to be driven by a couple of motors independently. The two driving systems can be recognized in Fig. 2-1, which are sketched respectively in green and purple. The front rotor (in green) fixed on the inner shaft is directly driven by a motor, while for the rear rotor (in purple) connected with the outer shaft, a

timing belt device (transmission ratio as 1:1) is employed to transmit the driving power from another motor. Between each motor and the corresponding shaft, a torque meter is installed to measure the driving torque and in turn the power consumption for the respective rotor.

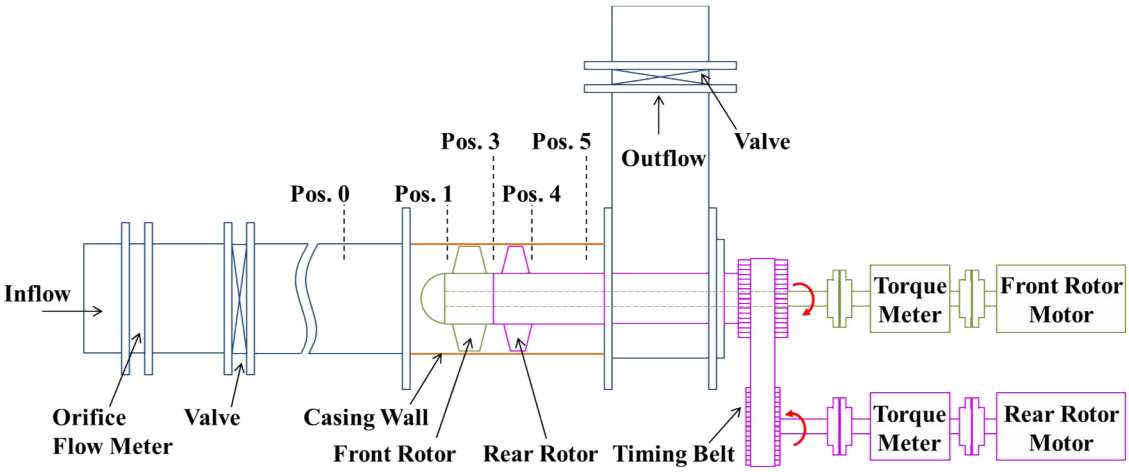

Fig. 2-1 Schematic view of experiment system for performance testing

The chief dimensions of the contra-rotating axial flow pump throughout this thesis are given in Table 2-1, where the subscripts c, h and t respectively denote the casing, the rotor hub and tip. The front and rear rotors have the same hub (D_h) and tip (D_t) diameters as shown here. The gap between two rotors is set to be 10% of the chord length of front rotor blade at hub, and then the gap near the blade tip is much larger due to the larger stagger angle and smaller axial length of the front rotor blade at tip. The detailed blade profile dimensions will be presented later. For example, those of the prototype pump will be shown in Sec. 3.1 of the following Chapter 3.

Table 2-1 Chief dimensions of prototype contra-rotating axial flow pump

D_c [mm]	D_h [mm]	D_t [mm]	D_h/D_t [-]	Tip clearance [mm]
200	100	198	0.505	1

Three sections at Pos.0, Pos.3, and Pos.5 are selected to represent the pump inlet, the front

rotor's outlet (also, the rear rotor's inlet), and the pump outlet respectively. The casing wall static pressure P_s measured at those sections are adopted in the calculation of the hydraulic head rise as described in Table 2-2. The dynamic head based only on the area averaged axial velocity $\overline{V_z}$ at the corresponding locations are considered. T and ω respectively denote the measured torque and the angular velocity of each rotor, and subscript '*loss*' represents the mechanical torque loss of the respective rotating unit.

Table 2-2 Hydraulic performance calculation from measurement results

	H [m]	η [-]
Contra-rotating pump	$\frac{(P_{s,5}+\frac{\rho\overline{V_{z,5}}^2}{2})-(P_{s,0}+\frac{\rho\overline{V_{z,0}}^2}{2})}{\rho g}$	$\frac{H_f+H_r}{H_f/\eta_f+H_r/\eta_r}$
Front rotor	$\frac{(P_{s,3}+\frac{\rho\overline{V_{z,3}}^2}{2})-(P_{s,0}+\frac{\rho\overline{V_{z,0}}^2}{2})}{\rho g}$	$\frac{\rho g Q H_f}{(T_f-T_{f,loss})\omega_f}$
Rear rotor	$H-H_f$	$\frac{\rho g Q H_r}{(T_r-T_{r,loss})\omega_r}$

In the following sub-sections, the major subsystems of the testing pump system are introduced in detail. Fig. 2-2 offers a schematic description about the whole measurement system, which chiefly consists of the following function modules:

1) Variable speed driving units
2) Rotation speed monitoring
3) Torque measurement
4) Flow rate measurement
5) Pump head rise measurement
6) Internal flow field measurement

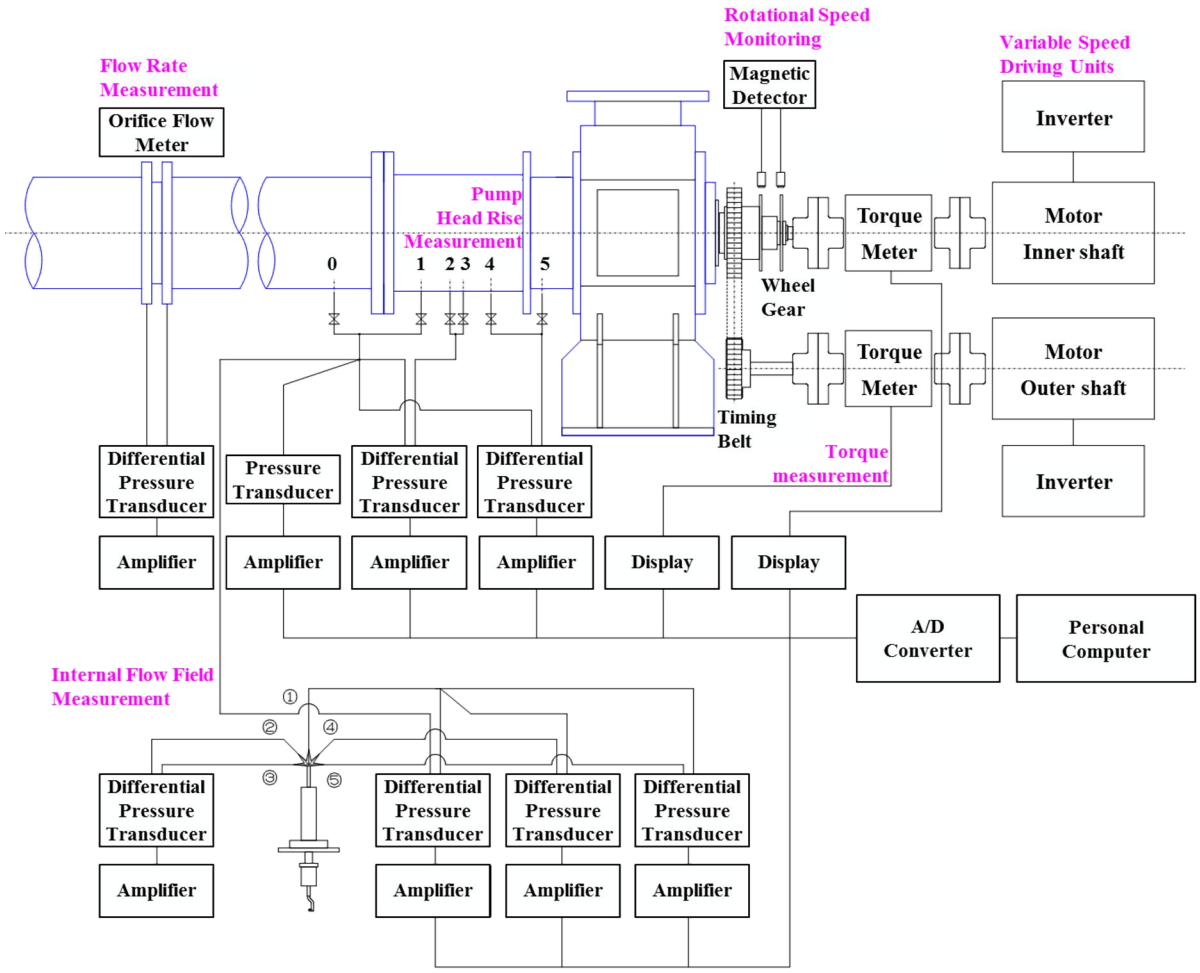

Fig. 2-2 Measuring system comprised by 6 function modules [49]

2.1.2 Variable speed driving units

As mentioned above, the front and rear rotors are driven by two 3-phase motors separately. The each motor is equipped with an inverter to establish the variable frequency drive system, which enables the corresponding motor working at the variable speed by adjusting its input voltage frequency and magnitude. In turn, driven by the respective motor at different speed, the individual rotation speed control of the contra-rotating rotors is realized. The chief parameters of the 3-phase motor and inverter employed here are given in Table 2-3 as follows.

Table 2-3 Chief parameters of driving units

General purpose	Model	Hitachi TFO-KK
3-phase motor	Power	5.5kW
	Voltage	220V
	Rated Speed	1800min^{-1}
Inverter	Model	Hitachi J300-055LF5
	Applicable Motor Capacity	5.5kW
	Output Frequency Range	0.1～400Hz
	Frequency Resolution	Digital: 0.01Hz/60Hz

2.1.3 Rotation speed monitoring

The monitor system for the each rotor's rotation speed as well as the corresponding motor speed is comprised by a rotating wheel gear (teeth number: 120) fixed at the respective shaft, a magnetic detector (ONOSOKKI MP-981) and a digital tachometer (ONOSOKKI TM-2130), whose specifications are given in Table 2-4.

Table 2-4 Specifications of rotation speed monitoring magnetic detector

Magnetic detector	Model	ONOSOKKI MP-981
	Detection Method	Hall element
	Measurement Range	1 Hz to 20 kHz (1 to 20,000 r/min)
	Detection Gear	Tooth width ≥ 3mm
	Output Waveform	Rectangular waveform
	Voltage Output	5V

2.1.4 Torque measurement

As mentioned in the overview, a torque measuring system is provided for the estimation of the driving torque as well as the power consumption. It is comprised by a torque transducer (TP-5KMCB) and its digital display (DPA-101A). The major specifications of these devices are given in following Table 2-5. Since this thesis focuses on the hydraulic performances of the pump, the mechanical torque losses are separately estimated by driving the shaft at the corresponding rotation speed in the air.

Table 2-5 Specifications of torque measurement devices

Torque Transducer	Model	TP-5KMCB
	Rated Capacity	49 N·m
	Rated Output	1.5mV/V (3000μm/m) ±0.2%
	Nonlinearity	Within ±0.2%RO
	Hysteresis	Within ±0.2%RO

2.1.5 Flow rate measurement

As one of the most popular flow rate measuring devices, an orifice flow meter estimates the flow rate from the static pressure variation across the orifice [50].

In the testing system, the orifice flow meter is installed far upstream of the test pump inlet to keep the inflow to the pump undisturbed. Given the geometries of the orifice plate (shown in Table 2-6) and the static head difference ΔH_s between the upstream and downstream of the orifice, the flow rate is estimated as the following equation, where A represents the area at the converged section $A = \pi d^2/4$,

$$Q = \alpha A\sqrt{2g\Delta H_s} \tag{2-1}$$

in which the discharge coefficient α is determined according to Japanese Industrial Standard JISB8302-1990 [51].

Table 2-6 Major geometrical features of orifice plate

Orifice	Pipe Diameter D	196 mm
	Orifice Diameter d	120 mm
	Discharge Coefficient	0.654
	Applicable Reynolds Number	$Re \geq 11\times10^4$
	Area Ratio β	$(d/D)^2=0.374$
	Discharge Coefficient α	$0.597-0.011\beta+0.432\beta^2$

The static pressure difference ΔP_s between the upstream and downstream of the orifice is directly measured by a differential pressure transducer (Kyowa PD-1KA) and then amplified by an instrumentation amplifier (WGA-710A), whose specifications are shown in Table 2-7.

Table 2-7 Chief parameters of orifice differential pressure transducers

Differential Pressure Transducers	Model	Kyowa PD-1KA
	Rated Capacity	100kPa
	Rated Output	1.5 mV/V (3000μm/m) ±1%
	Nonlinearity	Within ±0.3% RO
	Hysteresis	Within ±0.2% RO
Instrumentation Amplifier	Model	Kyowa WGA-710A
	Voltage Output	±10 V
	Nonlinearity	Within ±0.03 % FS
	Frequency Response Range	DC~10 kHz

2.1.6 Pump head rise measurement

The static pressure P_s on the casing wall is measured by the pressure transducers at five positions Pos.0 ~ 5 to capture the pressure variation through the pump rotors as illustrated in Fig. 2-2. Among those locations, only the static pressure P_s at Pos.0 is directly measured by the pressure transducer (PG-2KU) for the evaluation of the suction pressure. The static pressure variations ΔP_s from the suction pressure are acquired by the differential pressure transducer (PD-1KA) for other four locations. All of these pressure information are treated by the same type of amplifier (DPM-603A) with the specifications as listed in the following Table 2-8.

Table 2-8 Specifications of head rise measurement devices

Pressure Transducers	Model	Kyowa PG-2KU
	Rated Capacity	200kPa
	Rated Output	2 mV/V (4000μm/m) ±1%
	Nonlinearity	Within ±0.3% RO
	Hysteresis	Within ±0.3% RO
Differential Pressure Transducers	Model	Kyowa PD-1KA
	Rated Capacity	100kPa
	Rated Output	1.5 mV/V (3000μm/m) ±1%
	Nonlinearity	Within ±0.3% RO
	Hysteresis	Within ±0.2% RO
Amplifier	Model	Kyowa DPM-603A
	Voltage Output	±10 V
	Nonlinearity	Within ±0.02 % FS
	Frequency Response Range	DC~10 kHz

2.2 Internal flow field measurement

To better understand the internal flow pattern, a 5-hole probe is employed for the velocity distribution measurement. The velocity distribution is investigated in four sections of Pos.1, Pos.3, Pos.4 and Pos.5 as marked in Fig. 2-2 and Fig. 2-3, which respectively represent the flow status at the front rotor inlet, the rear rotor inlet (the front rotor outlet), the rear rotor outlet and the outlet of the whole pump. The measurement at each section is carried out at ten radial positions marked by the open circles in Fig. 2-3, which radially distribute from the hub area ($r/r_c = 0.525$) to the tip area ($r/r_c = 0.975$) with an even interval of 5mm.

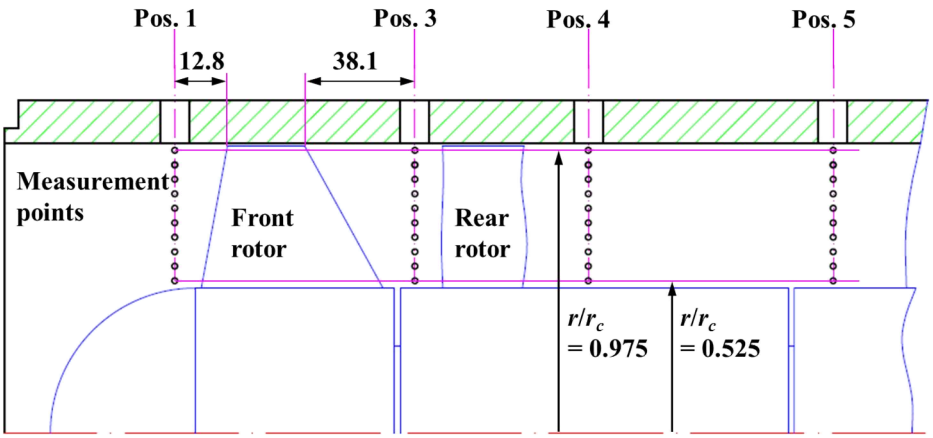

Fig. 2-3 Schematic view of velocity distribution measurement

2.2.1 Flow measurement by 5-hole probe

The 5-hole probe is a common measurement device for the flow velocity investigation, which consists of a central stagnation hole (Hole 1) and other four symmetrically displaced holes (Hole 2~5) as shown in Fig. 2-4. It is capable to obtain the local flow direction, the static pressure and the dynamic head where the incoming angle is unknown and/or significantly varying [52].

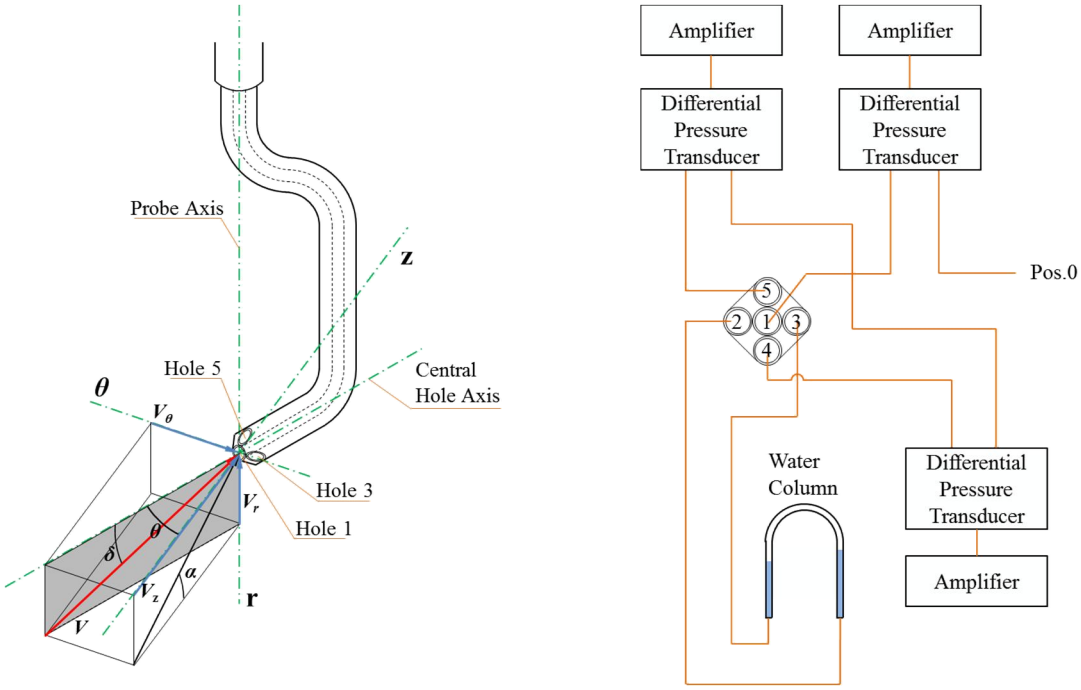

(a) Schematic of 5-hole probe and velocity vector (b) Pressure transducer connection

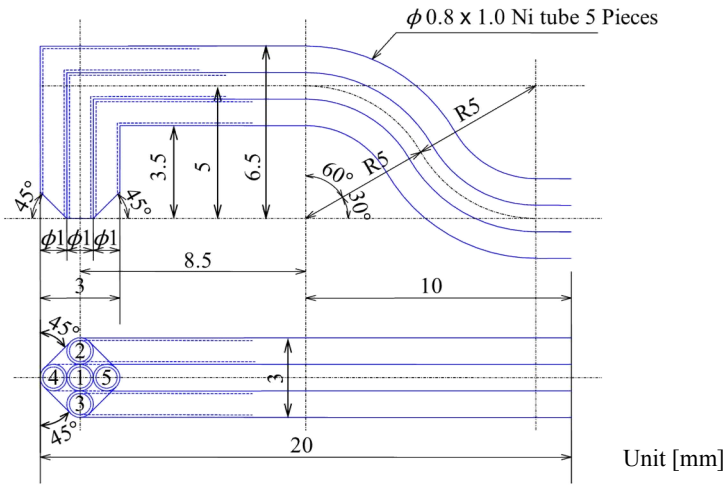

(c) Major dimensions of 5-hole probe head

Fig. 2-4 Measurement method of 5-hole probe

Generally in the present case, given the rotor's cylindrical coordinate system (r, θ, z) as shown in Fig. 2-4 (a), the probe is radially inserted in the flow field with the central hole's axis parallel to the θ-z plane, and determines the flow direction and velocity magnitude by revolving

on its probe axis. With the dimensions as shown in Fig. 2-4 (c), the probe head is thought to be rather small compared to either of those two rotors which have been designed with the hub diameter of 100 mm and the tip diameter of 198 mm. Hence, the flow disturbances due to the insert of the probe are believed to be fairly low, and the velocity distributions acquired in this way is considered to be sufficiently reliable.

The measured three dimensional velocity vector V sketched as red in Fig. 2-4 (a) could be decomposed into the axial component V_z, the radial component V_r and the tangential component V_θ as marked in blue, and the related orientation angles are defined in Table 2-9. These velocity components can be specified by the 5-hole probe in the following way.

Table 2-9 Definitions of orientation angles for velocity vector

Orientation Angles	θ	Angle between the axis z and the vertical projection of V on the θ-z plane
	δ	Angle from V to the θ-z plane
	α	Angle between the axis z and the vertical projection of V on the r-z plane

As shown in Fig. 2-4 (b), the local static pressure of each probe hole is compared with that of another position by certain differential pressure measurement devices. When the central hole axis aligns with the incoming flow direction in the θ-z plane, the probe hole 2 and 3 would offer the same static pressure reading as well as the same water level in the U tube, and the orientation angle θ is thus determined as the reading of the probe revolving angle at this moment. Moreover, the pressure differences between hole 1 and Pos. 0, hole 1 and 4 as well as hole 1 and 5 are simultaneously recorded by their respective transducers, as the inputs for the estimation of the corresponding orientation angle δ. In the next section, the estimation method for the orientation angle δ and the calibration of the 5-hole probe will be described in detail.

2.2.2 Calibration of 5-hole probe

For the precise flow measurement using 5-hole probe, the calibration curves are essential to represent the relationships between the measured pressures at the five holes and local total pressure, static pressure, dynamic pressure, and flow direction [53]. Those relationships are obtained from the calibration experiments before the probe is put into use, and usually expressed as the variation of the dimensionless pressure coefficients with the flow angularity.

For the 5-hole probe employed in the present researches, the calibration experiments were carried out in a wind tunnel with the airflow velocity as 16～128 m/s, corresponding to the water flow velocity of 1～8 m/s. And such velocity was determined according to the Reynolds number range in which the calibration data are unaffected by its variation, and in this calibration the Reynolds numbers were calculated based on the probe head diameter. Varying the angle (δ) between the tunnel nozzle axis and the central hole axis of the probe from -45° to 45°, the pressures at all probe holes were simultaneously recorded by the corresponding pressure transducers, and then the correlative dimensionless parameters were calculated as listed in Table 2-10 [54].

In Table 2-10, P_s represents the static pressure of the incoming airflow, P_{hi} denotes the pressure measured at the probe hole i. By such calibration experiments, the present 5-hole probe's response characteristics to a known flow field is obtained as shown in Fig. 2-5, based on which the flow orientation angle δ and the velocity components could in turn be estimated with the static pressure P_{hi} measured at probe holes.

Table 2-10 Key parameters in 5-hole probe calibration experiments

Orientation Coefficient	$C_i(\delta) = \dfrac{P_{hi}/\gamma - P_s/\gamma}{V^2/2g}$
Calibration Coefficient	$f_1(\delta) = \dfrac{C_1(\delta) - C_5(\delta)}{C_1(\delta) - C_4(\delta)} = \dfrac{P_{h1} - P_{h5}}{P_{h1} - P_{h4}}$
	$f_2(\delta) = \dfrac{1}{C_1(\delta) - C_4(\delta)}$
	$f_3(\delta) = 1 - C_1(\delta)$

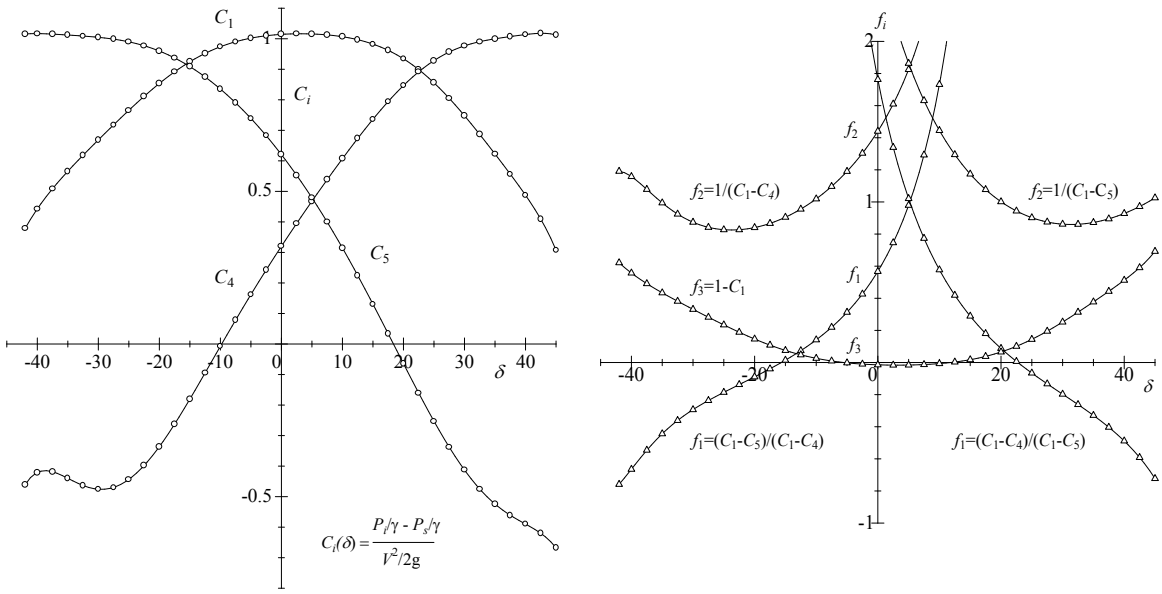

(a) Orientation coefficient $C_i(\delta)$ and angle δ (b) Calibration coefficient $f_i(\delta)$ and angle δ

Fig. 2-5 Calibration curves of 5-hole probe [54]

Generally in the present experiments, with the measured pressures P_{h1}, P_{h4} and P_{h5}, the characteristic $f_1(\delta)$ is calculated to evaluate the orientation angle δ, by which another parameter $f_2(\delta)$ is read from the calibration curves, and then the corresponding incoming flow velocities and total, static pressures are obtained as described in Table 2-11.

Table 2-11 Calculation of velocity components and relevant pressures

Velocity Components	$V = \sqrt{2g \cdot f_2(\delta) \cdot (P_{h1}/\gamma - P_{h4}/\gamma)}$
	$V_z = V \cos\delta \cos\theta$
	$V_\theta = V \cos\delta \sin\theta$
	$V_r = V \sin\delta$
	$\alpha = \tan^{-1}(V_r/V_z)$
Pressures	$H_t = P_{h1}/\gamma + f_3(\delta) \cdot V^2/2g$
	$H_s = H_t - V^2/2g$

2.2.3 Pressure measurement devices

As shown in Fig. 2-4 (b), except for the probe holes 2 and 3 which are connected with the water columns for the static pressure comparison, the other probe holes are respectively equipped with the differential pressure transducers and also amplifiers. For the combination of central hole 1 and upstream Pos. 0, a differential pressure transducer of larger capacity (PD-1KA) is adopted, while for the other combinations, the pressure transducers of relatively smaller capacity (PD-500GA) are employed.

Table 2-12 Specifications of 5-hole pressure measurement devices

Differential Pressure Transducers	Model	Kyowa PD-500GA
	Rated Capacity	50kPa
	Rated Output	1.5 mV/V (3000μm/m) ±1%
	Nonlinearity	Within ±0.3% RO
	Hysteresis	Within ±0.2% RO

Since the specifications of the transducer 'PD-1KA' and the amplifier 'DPM-603A' have been given in Sec. 2.1.6, only the type of 'PD-500GA' is described in Table 2-12.

2.3 Numerical simulation method

To further understand the internal flow properties of contra-rotating axial flow pump which is not accessible by the experimental approaches, the numerical simulations are imperative in the present researches. In this thesis, all of the simulation works were done with the commercial Computational Fluid Dynamics (CFD) code ANSYS CFX (13.0 or 14.0). The modeling and computational grid generations were done by ANSYS Turbogrid (13.0 or 14.0).

Based on the most common CFD solution method - finite volume technique, ANSYS CFX derives a full picture of the flow behavior by discretizing and iteratively resolving a series of essential partial differential equations in each control volume. Those equations include three components of Navier-Stokes equations describing the momentum conservation of fluid, the continuity equation describing the mass conservation law, and the energy equation, the last of which is solved if necessary [55]. To resolve the complex turbulent flow with limited computer resources, it is common to employ the turbulence model. Although the large eddy simulation is available in ANSYS CFX, for this study, two equation eddy viscosity model is used by coupling the Reynolds Averaged Navier-Stokes (RANS) equations instead of directly simulating Navier-Stokes equations.

For the contra-rotating axial flow pump case in the present researches, both the steady-state and unsteady-state simulations were conducted with the CFX module of Turbomachinery. The former one was commonly adopted for the preliminary estimation of pump performance, while the unsteady-state simulations appeared to be more reliable to offer the detailed internal flow structures since the internal flow of contra-rotating axial flow pump has been known as fairly

unsteady due to the rotor-rotor interaction.

The numerical simulation results for two pairs of contra-rotating rotors are discussed later in this thesis. These two pairs share the identical simulation settings, and only differ in the computation mesh due to the varied blade profiles.

2.3.1 Computational grid

ANSYS Turbogrid was employed to build the computation meshes for the contra-rotating axial flow pumps. For the steady-state computation only one blade passage for each rotor could be modeled, while for the unsteady simulation, the entire front and rear rotors with full annuluses were built to much more precisely reproduce the complicated flow structure at the rotor-rotor interface. As shown in Fig. 2-6, the each mesh is comprised by two oppositely rotating domains. The inlet boundary is located $4D_c$ upstream of the front rotor's leading edge, while the outlet boundary is placed $1.3D_c$ downstream from the trailing edge of the rear rotor. Between the blade tip and the cylindrical casing, i.e. tip clearance, 10 nodes are radially distributed in expectation of capturing the tip leakage flow.

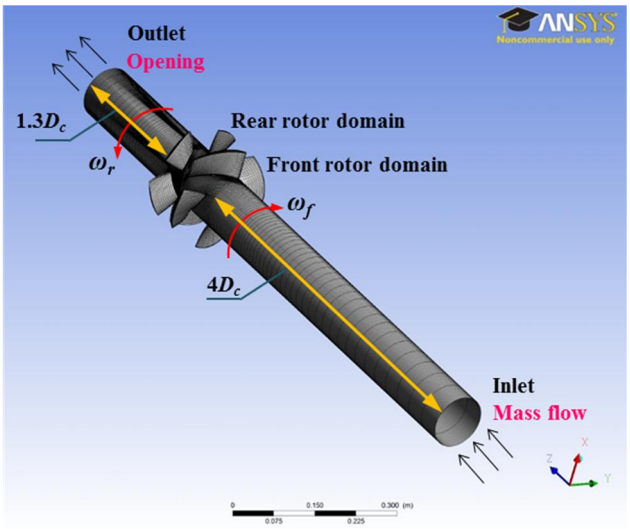

Fig. 2-6 Computational model of contra-rotating rotors

In general, for the model with the two entire rotors, the total number of the calculation nodes goes up to around 1.41 million for both the prototype pump mesh and the newly designed pump mesh, in which the node accounts for the front rotor domain and the rear rotor domain are 0.69 million and 0.72 million respectively. And they were both proved sufficiently fine to offer the simulation results of low grid-dependence.

2.3.2 Boundary conditions and domain interface

Both the steady and unsteady simulations adopted the similar boundary conditions as shown in Table 2-13, while at the interface between two rotors' domains, the quite different frame change models were respectively specified according to their different computation purposes.

Table 2-13 Boundary conditions and domain interface setting [56]

Inlet Boundary	**Steady & Unsteady Simulations**	**Type:** Mass flow **Flow Direction:** Normal to the boundary **Turbulence:** Medium
Outlet Boundary	**Steady & Unsteady Simulations**	**Type:** Opening (2 way flow allowed) **Mass and Momentum:** Entrainment / Static Pressure as Atmosphere The pressure value is taken to be static pressure for both the inflow and outflow, and the direction is obtained by enforcing the velocity gradient perpendicular to the boundary to be zero [56]. **Turbulence**: Zero Gradient (Fully developed turbulence condition)
Wall Condition	**Steady & Unsteady Simulations**	**Mass and Momentum:** No slip wall The fluid immediately next to the wall assumes the velocity of wall. The near wall fluid of low Reynolds number is treated according to the k-ω based SST Model (turbulence model mentioned in Sec. 2.3.3).

	Steady Simulation	**Frame Change:** Stage **Application:** Preliminary performance prediction near the design operation conditions with only one passage applied. **Description:** It performs a circumferential averaging of the fluxes through bands on the interface, and accounts for the time average interaction effects, but neglects the transient interaction effects. It is highly appropriate when the circumferential variation of the flow is of the order of the component pitch.
Domain Interface	**Steady Simulation**	**Frame Change:** Frozen Rotor **Application:** To acquire the initialization for a transient analysis. **Description:** The two frames connect with the relative position fixed throughout the computation, but with proper equation transformations made. It produces a steady state solution to the multiple frame case with very limited account of the frame interactions.
	Unsteady Simulation	**Frame Change:** Transient Rotor-Stator **Application:** Detailed simulation for the internal flow structures and rotor-rotor interactions. **Description:** It predicts the more plausible transient interaction of the flow between the domains with different speed, in which the relative position of the grids on each side of the interface is updated each timestep.

2.3.3 Turbulence model

In the present investigations, great emphasis was placed on the phenomenon of secondary flow and flow separation, which always originate from the boundary layer under the great adverse pressure gradient, since they were believed to be rather critical to induce the pump performance deficiency. For the limitation in the computation resources, the economical eddy-viscosity turbulence models based on the Reynolds Averaged Navier-Stokes (RANS) equations are preferred in this study. Hence, as the most prominent two-equation models proficient in the flow separation predictions, the k-ω based SST (Shear Stress Transfer) Model was employed in all of the simulation works. It applies the k-ε model in the far field free shear flows, and adopts the k-ω formulation in the near wall treatment for low-Reynolds number computations [56].

In both the k-ε and k-ω models, k [m^2/s^2] represents the turbulence kinetic energy as well as the variance of the fluctuations in velocity. And ε [m^2/s^3] is defined as the turbulence eddy dissipation which means the dissipating rate of the velocity fluctuations, ω [s^{-1}] as the turbulent frequency. The turbulence viscosity μ_t in the SST model is calculated by,

$$\mu_t = \rho \frac{k}{\omega}.$$

2.3.4 Basic settings of unsteady simulations

In the unsteady simulations, the discretization algorithm for the advection scheme and the transient scheme were respectively specified as High Resolution and Second Order Backward Euler Scheme.

As a key characteristic to track the progress of real time during simulations, the timestep was set to be a constant value with the consideration of the both rotors' rotation. It corresponded to the real time duration of 1° relative rotation between the front and rear rotors, which could be

calculated by the following equation,

$$\Delta t = \frac{1}{360}\frac{60}{N_f + N_r} \tag{2-2}$$

For the preliminary calculation beginning with a long meaningless flow fluctuation period, the total time duration must be specified with a sufficient length to obtain satisfied convergence. While in the latter runs for the performance evaluation, the time duration t should also be determined with special care in order to acquire sufficiently accurate time averaged values. In the present simulations, it was set as the real time to finish at least 4 full relative revolutions between two rotors as follows,

$$t = n \cdot \frac{60}{N_f + N_r} \tag{2-3}$$

where n denotes any integer greater than or equal to 4 in this study.

2.3.5 Performance evaluation with simulation results

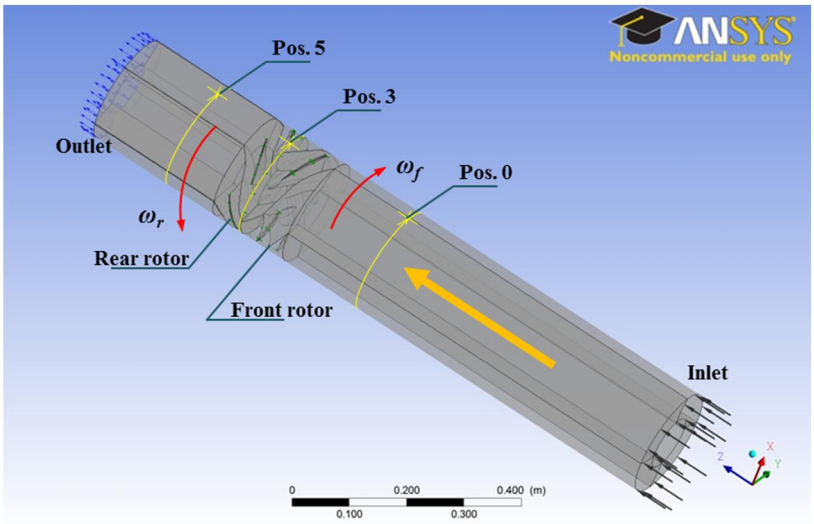

Fig. 2-7 Performance evaluation with simulation results

The locations which were used for the hydraulic performance calculation in the experiments as mentioned in Sec. 2.1.1, were again adopted to evaluate the related pump performance from

the simulation results.

The head rise was respectively evaluated with the circumferentially averaged static pressure P_s, and the mass flow averaged total pressure P_t at Pos.0, Pos.3 and Pos.5. The former one is similar to the experimental evaluation method, and the latter one seems more theoretically reasonable. The evaluation results of these two methods had been confirmed to be rather close with a deviation around 2% at the design flow rate, and the results adopted in this thesis were majorly based on the first evaluation method.

The efficiencies were also calculated based on the equations in Table 2-2, while the measured torque $T - T_{loss}$ for each rotor was replaced by the sum of the torque picked up at such rotor's all blades and hub surface $T_{blade} + T_{hub}$. Taking the rear rotor (in Fig. 2-8) as an example, T_{blade} is the overall torque around pump axis z calculated with all the blade surfaces considered, and T_{hub} with the whole rear rotor hub surface considered.

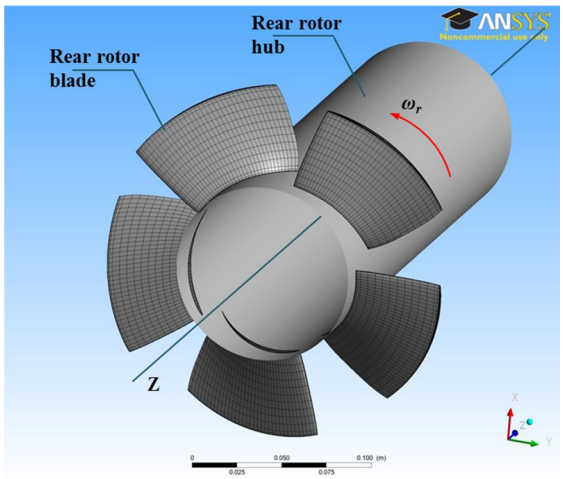

Fig. 2-8 Torque picking up for the rear rotor model

3 Design methodology

In this chapter, the design specifications of the secondary generation prototype contra-rotating rotors (herein named RR2 pair), designed in Flow Control Systems Laboratory of Kyushu University [42, 45], are firstly presented. The hydraulic performances, the internal flow properties as well as its pressure distributions are then discussed. Combining with the findings in RR2, the different-speed design method for the contra-rotating axial flow pump is proposed in expectation of the improved hydraulic performances of the contra-rotating rotors. In this concept the rotation speed combination of the two rotors is determined based on the reduced cavitation parameter $NPSH_r$ for the rear rotor. Relying on such design idea and several other considerations about the rotor blade profile geometries, the rear rotor is then re-designed and the rotor pair employing new rear rotor is herein named RR3 pair. To preliminarily validate this whole design concept, three types of RR3 rear rotors were proposed and then investigated by the numerical simulation approaches.

3.1 Design specifications and hydraulic performances of prototype rotor pair RR2

3.1.1 Design specifications of prototype rotor pair RR2

As mentioned in the introduction part (Sec. 1.1), the axial flow pumps are beneficial to be designed with high specific speeds, and reach the efficiency peak around N_s=1500 [min^{-1}, m^3/min, m] as shown in Fig. 1-2. Given the principal design specifications of H_d=4.0 m and Q_d=4.2 m^3/min, the prototype contra-rotating axial flow pump with RR2 applied was specified with the same individual rotor specific speed of 1500 [min^{-1}, m^3/min, m] for both front and rear rotors, resulting in the rotor rotation speeds of N_f=N_r=1225 min^{-1} and equally assigned head rise H_f=H_r=H_d/2. Then the overall specific speed of this combination (RR2) is N_s=1775

[min^{-1}, m^3/min, m] as calculated by the following Eq. (3-1).

$$N_s = \frac{(N_f + N_r)\sqrt{Q_d}}{{H_d}^{3/4}} \quad (3\text{-}1)$$

In Table 3-1, the major design specifications of this rotor pair RR2 are presented with two dimensionless characteristics ψ and ϕ defined by the following Eq. (3-2) and (3-3) respectively, where U_t denotes its blade tip peripheral velocity of the individual rotor.

Head coefficient: $$\psi = \frac{Hg}{{U_t}^2} \quad (3\text{-}2)$$

Flow coefficient: $$\phi = \frac{Q}{\mathrm{A}U_t} \quad (3\text{-}3)$$

Table 3-1 Design specifications of prototype contra-rotating rotors RR2

	H [m]	Q [m^3/min]	N [min^{-1}]	ψ [-]	ϕ [-]
Front Rotor	2.0	4.2	N_f = 1225	0.122	0.234
Rear Rotor	2.0	4.2	N_r = 1225	0.122	0.234
Axial Flow Pump	4.0	4.2	—	—	—

With the specifications described in Table 3-1, the front and rear rotors were respectively designed by a traditional two-dimensional design method, which has been widely used in the design of axial flow turbomachinery blades [57-59].

The ideal flow situation is considered, and the incoming flow for the front rotor were specified to be uniformly distributed in both radial and circumferential directions, so that the classic 'free vortex' model [2-4] assuming radial equilibrium condition was applied to describe the distributions of the Euler Head as well as the velocity swirl $V_{\theta 2,f}$ along the blade span. Subsequently, the ideal front rotor outflow profile calculated based on the 'free vortex' model was adopted as the inflow condition for the rear rotor design. The camber geometries at various

spanwise sections were then determined based on the given velocity distributions, and the sophisticated NACA series airfoil profiles were employed.

The blade shapes of the front and rear rotors in the RR2 combination are schematically shown in Fig. 3-1, and several key parameters of their blade profiles are given in Table 3-2. It could be seen that, designed with a relatively high rotation speed, the rear rotor shows a remarkably increased stagger angle compared with the downstream stator in the conventional rotor-stator type axial flow pump [42], suggesting the enhanced potential interferences between the two blade rows.

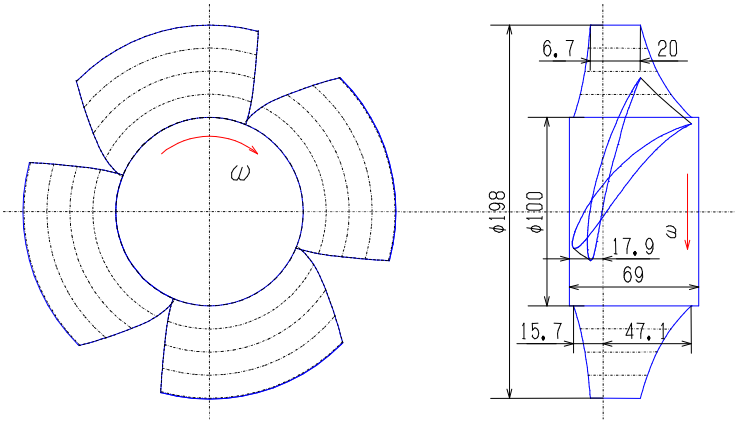

(a) Front rotor

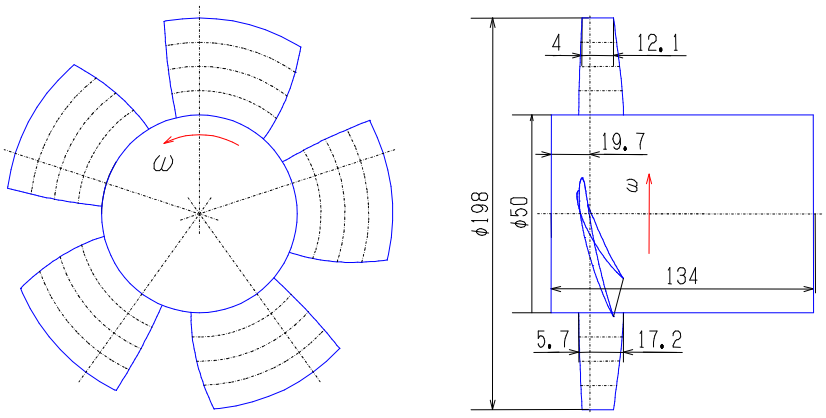

(b) Rear rotor RR2

Fig. 3-1 Schematic views of front and rear rotor blades shape in RR2

Table 3-2 Blade profile parameters of prototype contra-rotating rotors RR2

	Blade Number	Diameter [mm]		Profile	Solidity	Stagger Angle γ (°)
Front	4	Hub	100	NACA4410	1.290	51.72
Rotor		Mid-Span	150	NACA4408	0.898	68.48
		Tip	198	NACA4406	0.700	75.85
Rear	5	Hub	100	NACA4410	0.840	64.24
Rotor		Mid-Span	150	NACA4408	0.720	72.54
		Tip	198	NACA4406	0.600	77.56

3.1.2 Hydraulic performances of prototype rotor pair RR2

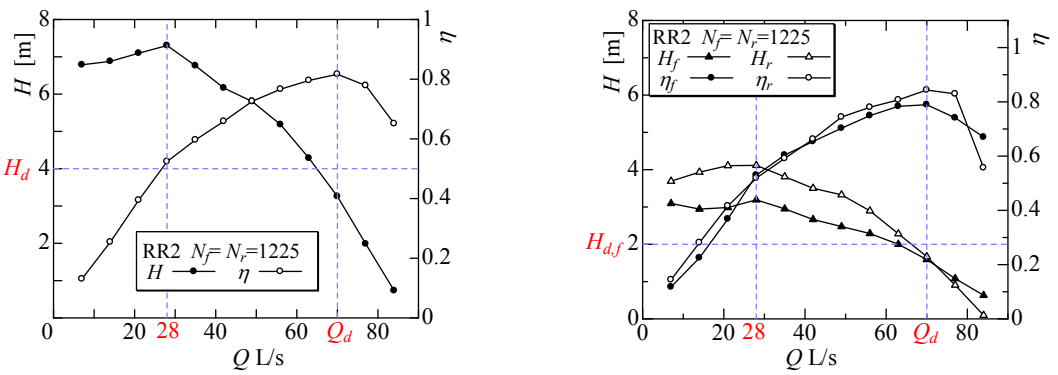

(a) Overall performance (b) Individual performance of each rotor

Fig. 3-2 Performance curves of prototype contra-rotating rotors RR2

With the experimental approaches discussed in Chapter 2, the hydraulic performance curves of the RR2 rotor pair were obtained as shown in Fig. 3-2, in which the flow rate Q is presented in the unit [L/s]. The superiorities of the contra-rotating axial flow pump over the traditional type are not emphasized here, since they have been repeatedly mentioned in the introduction part as well as several other reports [42, 45]. I only focus on some performance curve

characteristics of this rotor-rotor combination, which are majorly summarized as follows:

1) In terms of the hydraulic head rise H, the entire pump (H=3.25 m) and the individual rotors (H_f=1.59 m and H_r=1.67 m) all fail to meet the design specifications (H_d=4 m) at the design flow rate Q_d. The front rotor seems to operate with the maximum efficiency at the flow rate slightly lower than Q_d.

2) The front rotor generally appears with the inferior hydraulic efficiencies in the whole flow range (7 L/s<Q<84 L/s).

3) At the design flow rate, the rear rotor presents the head rise almost equal to that of the front rotor, but a quite steeper negative slope on its individual head curve, so that the head rise of the rear rotor goes up to a relatively higher level at the partial flow rate (Q<70 L/s).

4) In the rather low flow rate range (Q<28 L/s), the pump shows an unfavorable positive slope on its overall head rise curve, and this is supposed to be chiefly ascribed to the rear rotor which offers relatively larger hydraulic head and also an apparent positive slope.

Generally, designed with the same rotation speed as the front rotor, the rear rotor appears to be dominant in the flow pressure elevation at the partial flow rates. And although the contra-rotating rotors' inherent steeper negative slope of the Q-H curve is rather favorable in terms of the pumping system operation stability, it also means the difficulty to satisfy the design head accurately and implies that the more sophisticated design is required to meet the design specifications [45].

3.1.3 Internal flow structures of prototype rotor pair RR2

The radial distributions of the axial and circumferential components of the absolute velocity V_z and V_θ at Pos.1 and Pos.3, obtained by the 5-hole probe measurements and CFD simulations, are plotted in Fig. 3-3. The sections of Pos.1 and Pos.3 correspond to the inlet and

outlet of the front rotor respectively as mentioned previously. The Y-coordinate denotes the radial location r normalized by the casing radius r_c. The rotation direction of the front rotor is set to be positive for the circumferential velocities.

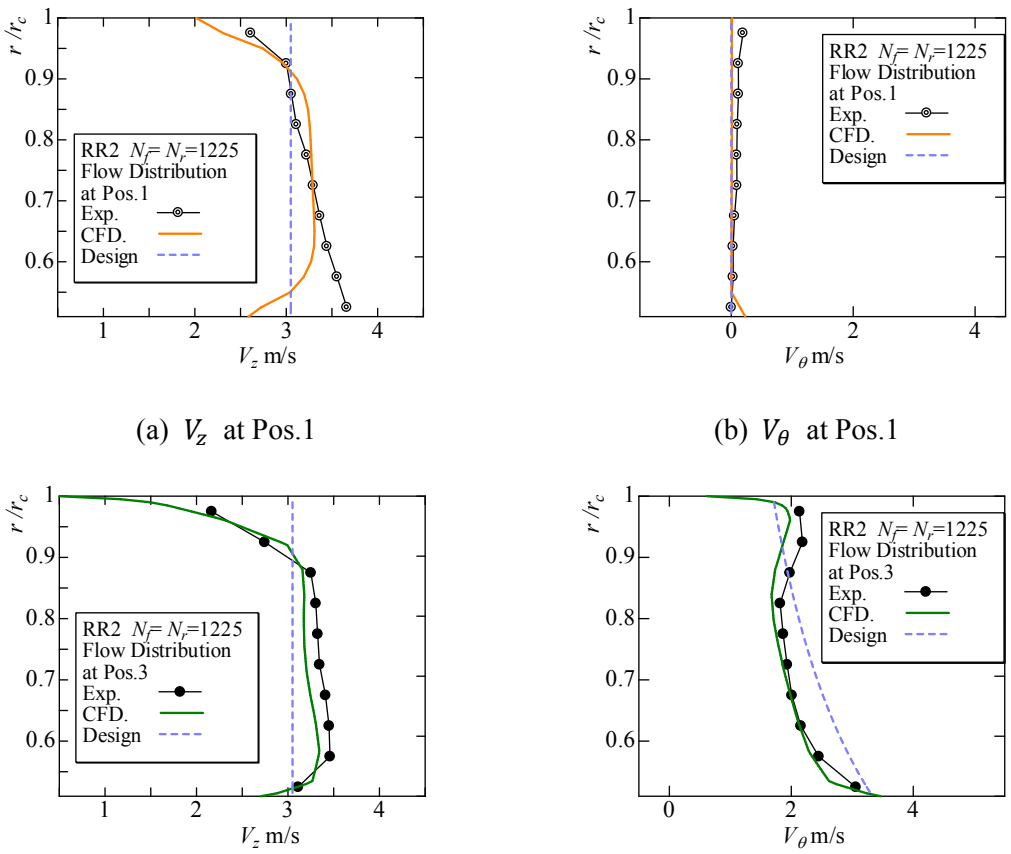

(a) V_z at Pos.1

(b) V_θ at Pos.1

(c) V_z at Pos.3

(d) V_θ at Pos.3

Fig. 3-3 Velocity distributions at inlet and outlet of front rotor under design flow rate

By both investigation approaches, it was found that the velocity distributions considerably were deviated from the design profile 'free vortex' (blue dashed lines). Compared with those at the outlet section, the velocity deviations at the front rotor inlet were relatively minor, and merely detectable for the axial velocity in the regions near to the hub and tip. The boundary layer effect was thought to mostly contribute to such velocity deficits there, while at Pos.3 the reason for the deviated velocity distributions was believed to be more complicated.

As plotted in Fig. 3-3 (c), the axial velocity V_z showed a well enlarged deficit content at the tip area, in which the flow distribution was supposed to be doubly impacted by the casing boundary layer and moreover the front rotor's tip leakage vortex. And the circumferential velocity V_θ in this region was in turn affected (raised) due to the low energy fluid stacked there entrained by the blade rotation as shown in Fig. 3-3 (d). The local flow rate was consequently enlarged in the radially inner flow region ($0.55 \leq r/r_c \leq 0.875$) due to the complex blockage at the upper near tip region, resulting in the pertinent deformation of the circumferential velocity profile there.

Designed with the ideal inflow profile (blue dashed lines in Fig. 3-3 (c) and (d)), the RR2 rear rotor left such front rotor's complex outflow structure out of consideration. Despite operating at the design flow rate with the rated speed, it was believed to be far from working under the design condition, which was thought to be one of the potential reasons for its limited hydraulic performance as shown in Fig. 3-2.

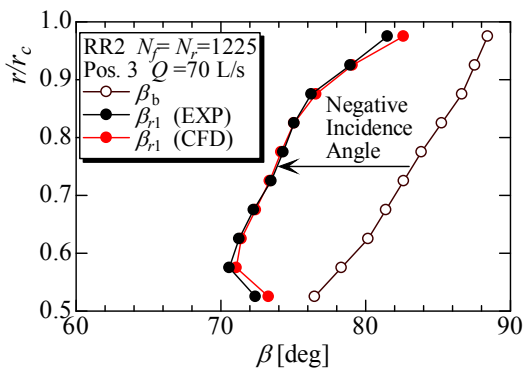

Fig. 3-4 Inflow angle distributions of rear rotor RR2

In Fig. 3-4, the radial distributions of the blade inlet angle β_{b1}, and the flow inlet angle β_{r1} obtained by the experimental and numerical approaches are plotted for the RR2 rear rotor. Given the incidence angle defined as $i = \beta_{r1} - \beta_{b1}$, it is rather obvious that the rear rotor had the negative incidence angles (i<0) in its whole spanwise range, which was known to be fairly

unfavorable to the cavitation performances [5]. And this could partly explain the cavitation inception occurred at the leading edge of the rear rotor as mentioned in Sec. 1.4.

3.1.4 Pressure distribution properties of RR2 rotor pair

As mentioned in the introduction part, the contra-rotating rotor pairs are all characterized by the considerable rotor-rotor interaction, and the interaction mechanisms vary with their specific applications. As a type of shrouded hydraulic turbomachinery, the contra-rotating axial flow pump takes the shockwave interference [24-33] and the mutually-induced velocities [37-41] out of consideration, and the wake effect originated from the upstream front rotor is also relatively powerless, since it decays sufficiently due to the relatively large gap between two rotors at tip section. In the previous study, the rotor-rotor interaction in this type of contra-rotating pump was believed to be dominated by the potential interaction between the pressure fields of two blade rows [44].

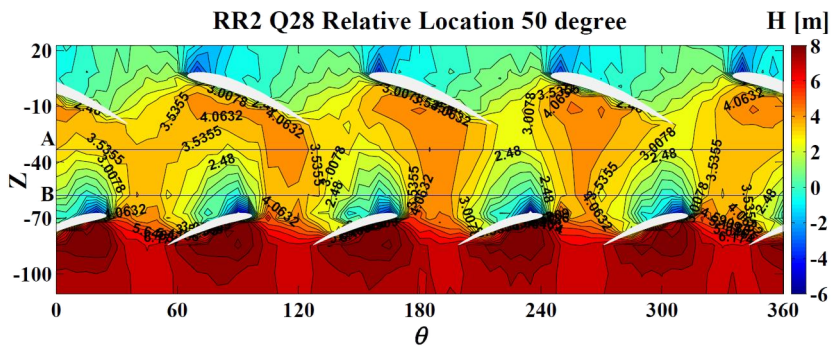

Fig. 3-5 Blade-to-blade pressure distribution of RR2 rotor pair at partial flow rate

To further discuss the rotor-rotor interaction in this contra-rotating rotor pair, a measured blade-to-blade pressure distribution at the rather low flow rate Q_d=28 L/s is given in Fig. 3-5, from which a significant potential interaction between two blade rows could be seen. Since the rear rotor RR2 has the fairly high blade stagger angles and the low pressure fields straightly towards upstream. The high pressure regions of the front rotor blades appear to be rather

vulnerable compared with the low pressure regions of the rear rotor, and are severely impacted due to the blade passing of the rear rotor.

This leads us to consider the possibility to suppress the rotor-rotor interaction and moreover maintain the contra-rotating pump's inherent performance superiorities by rearranging the design speed ratio between two rotors.

The pressure properties of the rear rotor RR2 is also emphasized here. In Fig. 3-6, the static pressure distribution around the RR2 blade tip profile at Q_d=70 L/s was obtained by the casing wall static pressure measurement experiments and CFD simulations, and the measurement method will be comprehensively explained in Chapter 5.

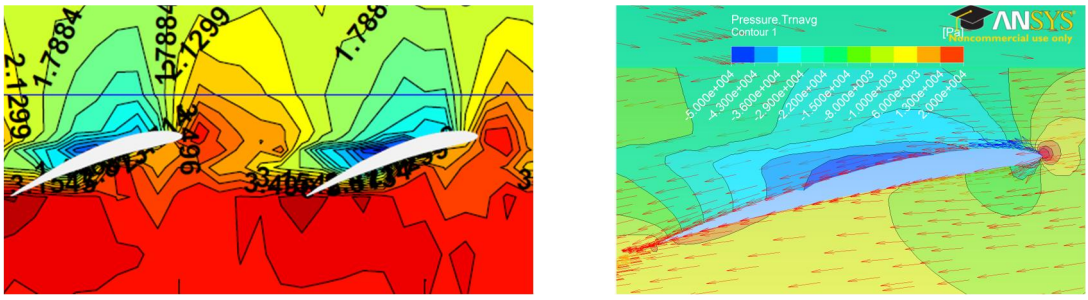

(a) By experiment (casing wall pressure)　　(b) By CFD simulation (r/r_c=0.975)

Fig. 3-6 Pressure distributions of RR2 rear rotor at design flow rate

It can be seen from both the experiment and simulation results that, the RR2 rear rotor blades show the aft-loading situation at the tip sections. And although the stagnation points are insufficiently clear to be recognized by the experiment due to the limited spatial resolution of the measurement (Fig. 3-6 (a)), they are believed to locate at the blade suction surfaces rather than the pressure surfaces as can be recognized by CFD method as shown in Fig. 3-6 (b). Those findings well coincide with the negative incidence angles discussed in above Sec. 3.1.3, and moreover suggest the cavitation inception at its pressure surface in the case that the ambient pressure reduces to a rather low level.

3.2 Different-speed design methodology

In the previous section, by the comprehensive analyses on the prototype contra-rotating axial flow pump, the inherent weaknesses of the equal speed contra-rotating rotors were understood, and several design concerns in the contra-rotating design were found. In this section, a new design method for the contra-rotating rotor pairs is introduced based on all above observations.

3.2.1 Determination of rotation speed combination

In the related investigations about the contra-rotating rotor-rotor combinations, numerous researchers had mentioned the significance of the speed ratio to the rotor pair's performances, and tried to find out the optimum speed combination for their specific applications [16-24]. Nevertheless, most of their studies were based on the experiments, and the theoretical analyses on the most beneficial speed ratio can hardly be found.

In the contra-rotating pump case, with the velocity triangles given in Fig. 1-5 and various analyses in the previous section, it was concluded that the rotation speed combination is decisive to the head division between two oppositely rotating rotors, and directly influential to the rotor geometries such as β_b, γ, and etc. And these are all crucial parameters in terms of the rotor-rotor interaction and in turn the overall pump performances. Instead of concentrating on the experimental explorations, it will be tried in this section to build an optimization method for the rotor-rotor speed combination based on theoretical analyses.

A different-speed design method is proposed to quantify the more appropriate rotor speeds emphasizing especially on the improvement of the cavitation characteristics $NPSH_r$. This design concept also aims to suppress the rotor-rotor interaction and moreover maintain the contra-rotating rotors' inherent performance superiorities by reducing the rotation speed of the

rear rotor to a reasonable level.

From the velocity triangles of the contra-rotating rotors (Fig. 1-5), it could be easily found that, designed with the equal rotation speed (U_f=U_r), the rear rotor RR2 represents relatively larger absolute ($V_{1,r}$>$V_{1,f}$) and relative ($W_{1,r}$>$W_{1,f}$) velocities at the inlet. Given the Required Net Positive Suction Head ($NPSH_r$) defined in Eq. (1-5), and only taking account of the profile coefficient λ_2 (λ_1=1 λ_2≠1), the cavitation characteristics of the two contra-rotating rotors respectively expressed as follows.

Front rotor: $$\mathrm{NPSH}_{r,f} = \frac{{V_{1,f}}^2}{2g} + \lambda_f \frac{{W_{1,f}}^2}{2g} \quad (3\text{-}4)$$

Rear rotor: $$\mathrm{NPSH}_{r,r} = \frac{{V_{1,r}}^2}{2g} + \lambda_r \frac{{W_{1,r}}^2}{2g} - H_f \quad (3\text{-}5)$$

where λ_f and λ_r denote the profile loss coefficients of the front and rear rotors respectively. And according to the velocity triangles, it could be easily obtained that,

$$V_{1,f} = V_z$$

$${V_{2,f}}^2 = {V_{1,r}}^2 = {V_{\theta 1,r}}^2 + {V_z}^2$$

where V_z represents the axial velocity through the pump rotors, and $V_{\theta 1,r}$ represents the circumferential component of the absolute velocity at the rear rotor inlet.

In expectation of the cavitation inception occurred at the leading edge of the front rotor, the condition of $\mathrm{NPSH}_{r,f}$>$\mathrm{NPSH}_{r,r}$ must be ensured, which takes the form as follows.

$$\lambda_f \frac{{W_{1,f}}^2}{2g} - \lambda_r \frac{{W_{1,r}}^2}{2g} - \frac{{V_{\theta 1,r}}^2}{2g} + H_f > 0$$

Since the level of minimum pressure around the blade in each rotor is essentially dominated by the corresponding relative velocity, an essential specification of $W_{1,f}$=$W_{1,r}$ is introduced to emphasize the purpose of the cavitation performance improvement for the rear rotor, and give

the assumption of $\lambda_f = \lambda_r$, then

$$H_f - \frac{{V_{\theta 1,r}}^2}{2g} > 0 \tag{3-6}$$

Combining the Euler equation as well as the no-swirl inflow and outflow conditions, the overall hydraulic head rise of the pump could be expressed as,

$$H = H_f + H_r = \eta_f \frac{U_f V_{\theta 2,f}}{g} + \eta_r \frac{U_r V_{\theta 1,r}}{g} = \frac{V_{\theta 1,r}}{g}(\eta_f U_f + \eta_r U_r) \tag{3-7}$$

where it has been set that $V_{\theta 2,f} = V_{\theta 1,r}$. Then, the above Eq. (3-6) takes the form,

$$\frac{V_{\theta 1,r}}{2g}\left(2\eta_f U_f - V_{\theta 1,r}\right) > 0 \tag{3-8}$$

Back to the velocity triangles,

$${W_{1,f}}^2 = {V_z}^2 + {U_f}^2$$

$${W_{1,r}}^2 = {V_z}^2 + (V_{\theta 1,r} + U_r)^2$$

the following equation is obtained by setting $W_{1,r} = W_{1,f}$,

$$U_f = V_{\theta 1,r} + U_r \tag{3-9}$$

Simplifying the efficiencies of the whole pump and the individual rotors as $\eta = \eta_f = \eta_r$, the following equation can be obtained from Eq. (3-7),

$$\frac{Hg}{\eta_f} = \left(U_f + U_r\right) V_{\theta 1,r} \tag{3-10}$$

by substituting Eq. (3-9) and the definition of head coefficient expressed by $\psi_f = \eta_f V_{\theta 1,r} / U_f$ into Eq. (3-10), the following equation is obtained

$$\frac{Hg}{\eta_f} = {U_f}^2 - \left(U_f - \frac{\psi_f U_f}{\eta_f}\right)^2 \tag{3-11}$$

Hence, given the design overall head rise H and the estimated hydraulic efficiency η, the redesigned rotation speed for the front rotor is determined by,

$$N_f = \frac{60 \cdot U_f}{\pi D} = \frac{60}{\pi D}\sqrt{\frac{Hg/\eta_f}{1-(1-\psi_f/\eta_f)^2}} \tag{3-12}$$

where D denotes the diameter of the blade tip cylinder.

Combining this equation with Eq. (3-9), the rear rotor's rotation speed could be determined as follows,

$$N_r = \frac{60}{\pi D}\left(1-\frac{\psi_f}{\eta_f}\right)\sqrt{\frac{Hg/\eta_f}{1-(1-\psi_f/\eta_f)^2}} \tag{3-13}$$

In general, for the above derivation of the new rotation speeds N_f and N_r, the cavitation performance improvement for the rear rotor is emphasized throughout. With such consideration, the relative velocity $W_{1,r}$ which essentially dominates the minimum static pressure P_{min} and in turn the cavitation inception around the rear rotor's blade is reduced to be equal to $W_{1,f}$, and this consequently results in the different rotation speeds for the front and rear rotors as Eqs. (3-12) and (3-13).

To validate this different-speed design idea, a new pair of contra-rotating rotors with above rotation speeds applied is discussed in the following sections. This new rotor pair (named as RR3 pair) is comprised of the identical front rotor which was employed in the prototype pump, and a new rear rotor which was designed with the new rotation speed and other considerations described in the following sections.

The same overall design specifications of H_d=4.0 m and Q_d=70 L/s were given to this new rotor pair. In addition, to ensure the front rotor work with the maximum efficiency at the design condition, $\eta_{f,max}$=0.796 and the corresponding $\psi_{f,max}$=0.114, which were acquired from its

dimensionless curves (Fig. 3-7), were substituted into the speed equations, Eqs. (3-12) and (3-13). Generally, the new rotor pair RR3 appears with a reduced rotation speed for the rear rotor as listed in Table 3-3.

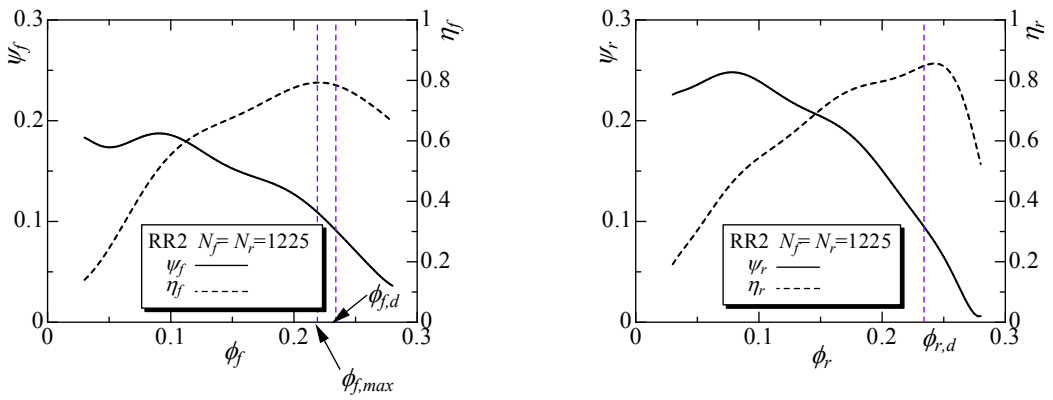

(a) Front rotor (b) Rear rotor

Fig. 3-7 Dimensionless performance curves of front and rear rotors in RR2

Table 3-3 Design specifications of new contra-rotating rotors RR3

	H [m]	Q [m^3/min]	N [min^{-1}]	ψ [-]	ϕ [-]
Front Rotor	2.15	4.2	N_f = 1311	0.114	0.219
Rear Rotor	1.85	4.2	N_r = 1123	0.134	0.255
Axial Flow Pump	4.0	4.2	—	—	—

3.2.2 Inflow velocity profiles for RR3 rear rotor

As mentioned in Sec. 3.1.3, despite operating at the design flow rate with the rated speed, the rear rotor RR2 was far from working under the design condition due to the considerable deviations from the specified inflow velocity profile.

Since the ideal front rotor outflow profile based on the ‘free vortex’ law was found to be inadequate to model the design inflow profile of the rear rotor, the ‘forced vortex’ law [2-4] was

introduced in the new rear rotor design. Both of these two models are very classical in the design of axial flow turbomachineries, in which the spanwise variation laws for the Euler head H_{th} as well as the swirl velocity are specified. Commonly with the normal inflow condition for the rotor blades in axial flow machines, the radial distributions of cylindrical velocity components could be described as Table 3-4, and $C_1 \sim C_4$ all denote arbitrary constants.

Table 3-4 Velocity distributions specified by two fundamental models

	V_r	V_θ	V_z	H_{th}
Free Vortex	0	$V_\theta r = C_1$	$V_z = C_2$	$H_{th} = \omega C_2$
Forced Vortex	0	$\frac{V_\theta}{r} = C_3$	$V_z = \sqrt{(C_4 - 2{C_3}^2 r^2)}$	$H_{th} = \omega r^2 C_3$

It is distinctive that in the 'forced vortex' design, the circumferential velocity V_θ increases proportional to the radius, while the axial velocity V_z decreases with it, and the theoretical Euler head grows rapidly in the radial direction. The velocity distributions described by this model highly resemble to the observed front rotor outflow profiles in the tip region which was plotted in Fig. 3-3 (c) and (d).

Hence, in the new rear rotor design, a 'integrated model' combined by 'free vortex' and 'forced vortex' was employed as described in Table 3-5, where r_c and r_h respectively denote the radii of the pump casing and hub, and C_1, C_2, Ω, K are all constants. The joint section between two models was determined at the cylindrical surface with r_m=0.875 r_c, since around this position the velocities were experimentally and numerically confirmed to start deviating regardless of the rotation speed as shown in Fig. 3-3 (c) and (d). It should be noted that this location is probably dependent on the design condition and pump size, but it can be determined simply by the numerical simulations of the preceding front rotor.

Table 3-5 Integrated model applied in new rear rotor design

	Model	V_θ	V_z
$r_m < r < r_c$	Forced Vortex	$\frac{V_\theta}{r - r_h} = \Omega$	$V_z = \sqrt{(C_2 - 2\Omega^2(r - r_h)^2)}$
$r = r_m$	Joint	$\frac{K}{r_m} = (r_m - r_h)\Omega$	$C_1 = \sqrt{(C_2 - 2\Omega^2(r_m - r_h)^2)}$
$r_h < r < r_m$	Free Vortex	$V_\theta r = K$	$V_z = C_1$

In Fig. 3-8, the numerically simulated rear rotor inflow profiles at two rotation speeds are shown, and the flow distributions based on two design methods ('Free Vortex' and 'Integrated Model') are also plotted.

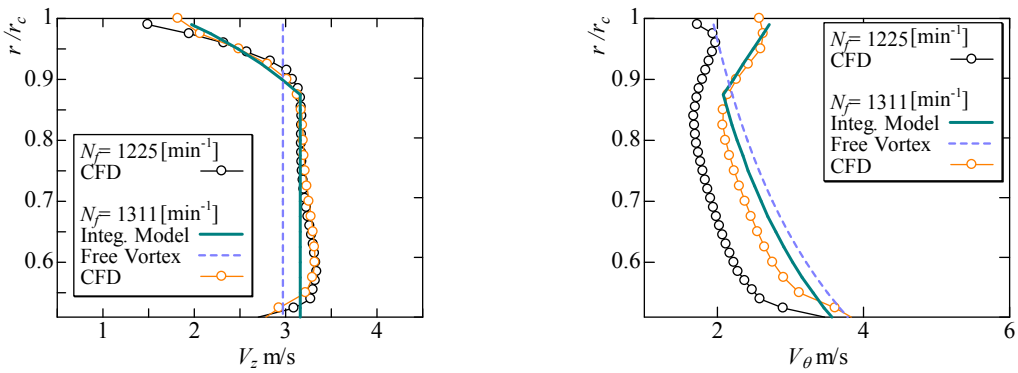

(a) V_z (b) V_θ

Fig. 3-8 Inflow velocity profiles obtained by various approaches at design flow rate

The increase in the front rotor rotation speed results in the raised theoretical head as well as the enhanced velocity swirl V_θ as shown in Fig. 3-8. Based on this rotation speed, the flow profiles (blue dashed lines) estimated by the 'free vortex' law is still inadequate, while the above proposed 'integrated model' shows the velocity distributions (green solid lines) well agreed with those obtained by the CFD simulation (orange dot lines).

3.2.3 Determination of relevant flow angles

With the inflow distributions determined above and the ideal non-swirl outflow condition, the relevant flow angles are defined as Fig. 3-9 and Table 3-6.

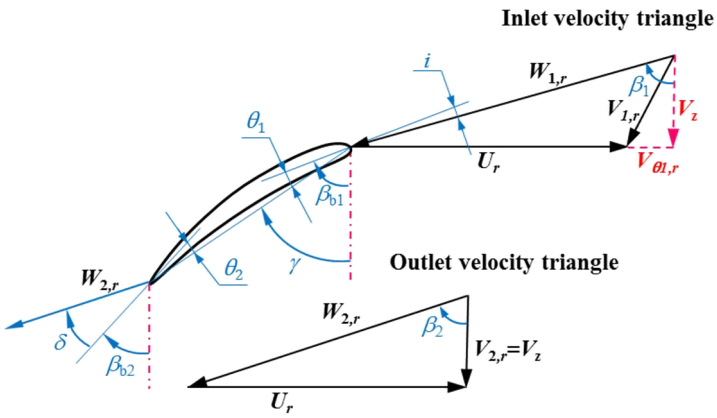

Fig. 3-9 Schematic flow angles for rear rotor

Table 3-6 Definitions of flow angles

Flow Angle	Definition
Flow Inlet Angle	$\beta_1 = \tan^{-1}(\frac{V_{\theta 1} + U_r}{V_z})$
Incidence Angle	$i = 2°$
Blade Inlet Angle	$\beta_{b1} = \beta_1 - i$
Flow Outlet Angle	$\beta_2 = \tan^{-1}(\frac{U_r}{V_z})$
Deviation Angle	$\delta = \Delta\beta + 13.05\left(\frac{x_f}{l} - 0.4\right)$ （3-14）
Blade Outlet Angle	$\beta_{b2} = \beta_2 - \delta$

Since the previous RR2 rear rotor was found with the rather large negative incidence angles (in Sec. 3.1.3) which was believed to be fairly unfavorable to the cavitation performances, the positive incidence angles (i>0°) are herein emphasized as one of the essential design

considerations for the new rear rotor. Considering the possible gentle variation of the water supply capacity which would result in the incidence angle deviation, the incidence angles were set as a value slightly greater than zero (i=2°) at the design flow rate, to minimize the inlet shock and moreover to keep it still above zero when the system flow rate suffers from the unexpected increase.

With the classic deviation angle model of

$$\delta = m_c(\beta_{b1} - \beta_{b2})\sigma^{-n_c}$$

applied where m_c=0.26, n_c=0.5 as in the axial flow compressors and σ represents the cascade solidity [54], the outflow velocities of the new rear rotor were found with small circumferential components in the numerical simulations. By the parametric studies using CFD technology, a new empirical equation (Eq. (3-14) in Table 3-6) is proposed for the deviation angle δ in expectation of correcting the outflow to the non-swirl condition. In this equation, x_f/l denotes the maximum camber location x_f relative to the chord length l, and $\Delta\beta$ is defined as the flow turning angle $\Delta\beta$=$\beta_1 - \beta_2$.

3.2.4 Determination of profile geometries

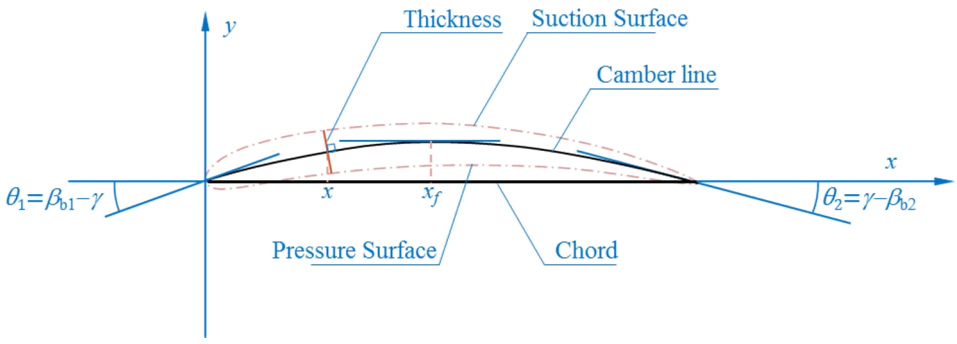

Fig. 3-10 Schematic camber line geometry

The airfoil camber line geometry at any blade section as schematically illustrated in Fig.

3-10 is expressed by a typical quadratic parabola for simplicity as,

$$\theta(x)=ax^2+bx+c \tag{3-15}$$

where a, b, and c respectively denote any arbitrary constants, x ranges from 0 to the chord length l, and θ represents the local gradient angle of the camber curve with the condition of $\tan\theta = dy/dx$. Given the above specified flow distributions and the limitations of

$$\theta(x=0)=\beta_{b1}-\gamma$$

$$\theta(x=l)=\beta_{b2}-\gamma$$

$$\theta(x=x_f)=0$$

the camber line geometry and the stagger angle γ were obtained through the iterative calculation. As an essential parameter for the camber line geometry, the special care was given to the maximum camber location x_f/l in the new rear rotor design.

In the 1990s, Zangeneh, M. et al. raised a set of guidelines to suppress the secondary flow as well as to make the outflow field uniform for the mixed flow and centrifugal turbomachineries [60, 61]. They described the optimum pressure distribution model for the impellers in terms of the suppression of secondary flow, and proposed that it is beneficial to respectively increase the blade aft part loading at the hub section and decrease that at the tip area.

Based on this concept, the RR3 blades with the tip profiles of fore-loading and the hub profiles relatively aft loaded are considered. This is realized by the idea of varying maximum camber location along spanwise, in which the value of x_f/l gradually reduces from 60% at the hub section to 40% at the tip section. The thickness evolution law of NACA 4* series [62] as expressed by Eq. (3-16) was adopted,

$$\frac{y_t(x)}{l}=5\frac{t}{l}\left\{a_0\sqrt{\frac{x}{l}}+a_1\frac{x}{l}+a_2\left(\frac{x}{l}\right)^2+a_3\left(\frac{x}{l}\right)^3+a_4\left(\frac{x}{l}\right)^4\right\} \tag{3-16}$$

where $y_t(x)/l$ represents the relative thickness at any arbitrary position of x/l, and $a_0 \sim a_4$ are given by the NACA4* profile data. With the calculated thickness perpendicularly growing at the corresponding camber point to both sides, the outlines of the pressure and suction surfaces are generated as shown in Fig. 3-10. In expectation of better flow turning, the blade row solidity σ is increased up to 1.2 times of that in RR2.

3.3 Preliminary models for new rear rotor RR3

3.3.1 Geometries of three types of new rear rotors

To preliminarily validate the design ideas of the inflow profile optimization and secondary flow suppression, three types of RR3 rear rotors were designed with such ideas separately or comprehensively applied as shown in Table 3-7.

Table 3-7 Blade profile geometries of three types of RR3

Type	Design Ideas		Section	1(Hub)	2	3	4	5(Tip)
	Inflow	x_f/l	D [m]	0.100	0.125	0.150	0.175	0.198
RR2	Free	Constant	$\sigma(l/t)$	0.840	0.780	0.720	0.660	0.600
	Vortex		x_f/l	0.40	0.40	0.40	0.40	0.40
			γ[°]	64.24	68.86	72.54	75.34	77.56
			α[°]	5.17	3.08	1.56	0.53	-0.23
RR3-Z	Integrated	Variable	$\sigma(l/t)$	1.008	0.936	0.864	0.792	0.720
	Model		x_f/l	0.60	0.55	0.50	0.45	0.40
			γ[°]	64.95	67.05	69.73	72.33	71.88
			α[°]	3.414	3.793	3.292	2.529	8.613
RR3-F	Free	Variable	$\sigma(l/t)$	1.008	0.936	0.864	0.792	0.720
	Vortex		x_f/l	0.60	0.55	0.50	0.45	0.40
			γ[°]	65.44	67.26	69.73	72.15	74.24
			α[°]	3.734	4.270	3.890	3.236	2.512
RR3-40	Integrated	Constant	$\sigma(l/t)$	1.008	0.936	0.864	0.792	0.720
	Model		x_f/l	0.40	0.40	0.40	0.40	0.40
			γ[°]	58.71	65.14	69.47	72.53	71.88
			α[°]	9.654	5.703	3.552	2.329	8.613

In Table 3-7, it is clear that the design considerations are distinctively reflected by the geometries of various blade profiles.

1) As expected previously, with the reduced rotation speed, all the RR3 types appear with relatively smaller stagger angles at most of their sections, which is beneficial to weaken the rotor-rotor interaction. While designed with the maximum camber locations varying in the spanwise direction, RR3-Z and RR3-F represent comparable stagger angles with RR2 in the hub region, which could be easily explained with the flow inlet angle written into the following form,

$$\beta_1 = \gamma + \theta_1 + i \tag{3-17}$$

with the maximum camber location more backward (60%), the hub profile presents the reduced inlet camber angle θ_1, and in turn results in the increased stagger angle, since the inflow angle β_1 and incidence angle i are both fixed by the designed flow distributions.

2) For all the RR3 types, the positive incidence angle design results in the increased attack angle, which is defined as illustrated in Fig. 3-11.

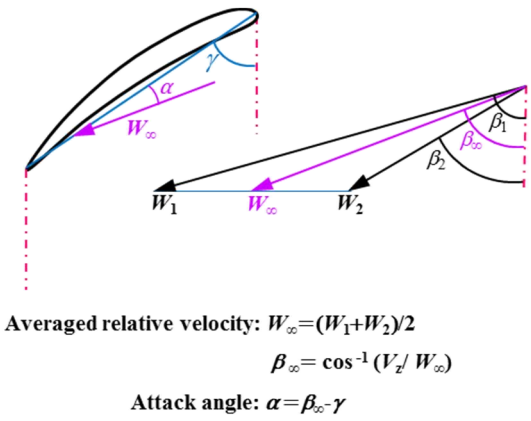

Fig. 3-11 Definition of attack angle

With the integrated inflow model considering the forced vortex design near the tip, the type

of RR3-Z and RR3-40 get remarkably increased attack angles α at the tip area. This is believed to be induced by the well reduced axial velocities and increased circumferential velocities in that model. Based on the velocity triangles, it is easy to understand that such inflow profile results in the sharply increased inflow angle β_1, which would in turn lead to the steep increase in the averaged flow angle β_∞ and eventually in the attack angle.

3.3.2 Hydraulic performance investigation for three types of new rear rotors

With the unsteady CFD simulation methods mentioned in Chapter 2, the basic hydraulic performances of three types of RR3 rotor pairs at the design flow rate Q_d=70 L/s (4.2 m^3/min) were obtained as shown in Fig. 3-12.

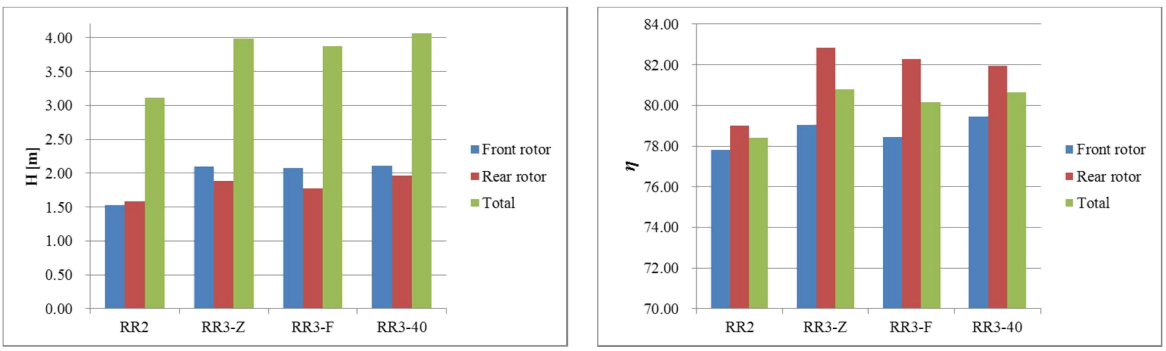

(a) Hydraulic head rise (b) Hydraulic efficiency

Fig. 3-12 Numerical simulated performances of RR3 and RR2 at design flow rate

With the several design ideas applied, three types of new contra-rotating rotors were all found to highly satisfy the design specifications with the superior efficiencies compared to the prototype rotor pair RR2, and in all three pairs, the front rotor offered the hydraulic head rise around 2.1m fairly close to the design head 2.15m.

The RR3-40 type showed highest individual rotor head rise as well as the overall pump head rise, but the lowest individual efficiency among the three rotors. With the irrational inflow

profile, the RR3-F type presented relatively higher stagger angle and smaller attack angle at the tip area as described in Table 3-7. Among the three rotor pairs, it turned out with the most inferior performances in head rises as well as efficiencies. As discussed previously, operating with the inflow profile deviated from the design condition was believed to be the major reason for such inadequate performances, since various kinds of losses always result from that. In contrast, although the RR3-Z type with both design ideas applied appeared to be slightly inferior in head rise, it shows much obvious superiority with the highest efficiency of 82.84%.

3.3.3 Evaluation of cavitation performances by $NPSH_r$

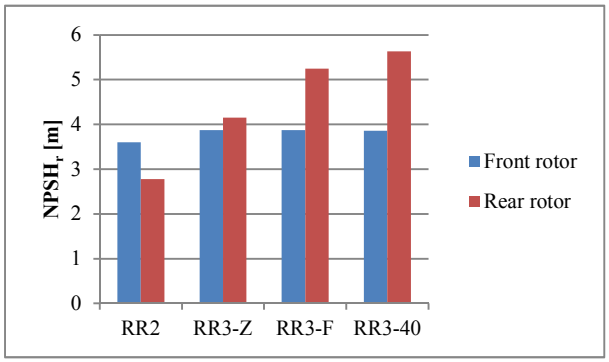

Fig. 3-13 $NPSH_r$ for RR2 pair and three types of RR3 pairs (by CFD)

For the rotor pairs of RR2 and three types of RR3, the property of cavitation inception were studied by unsteady CFD simulations with the parameter of $NPSH_r$ (required net positive suction head) as shown in Fig. 3-13, which was calculated under their respective design conditions by the following Eq. (3-18),

$$\mathrm{NPSH}_r = \frac{P_{t,1} - P_{min}}{\rho g} \qquad (3\text{-}18)$$

where $P_{t,1}$ represents the total pressure at the pump inlet, and P_{min} the minimum pressure obtained around the blades of each rotor.

Due to the increased rotation speed (N_f=1311 [min^{-1}]) as well as the improved head rise

under the design condition, the front rotor appeared with the higher $NPSH_r$ in the RR3 rotor pairs. Nevertheless, with the reduced design rotation speed (N_r=1123 [min^{-1}]), the three types of RR3 rear rotors presented much increased $NPSH_r$ compared with the RR2 rear rotor. This is probably due to the fact that they are all designed with the positive incidence angle (i=2 [°]) and the subsequently enlarged attack angles (Table 3-7).

Hence from Fig. 3-13, all the RR3 rear rotors seem to be inferior in terms of the cavitation inception, which means they are very likely to suffer the cavitation inception earlier than the RR2 type when the ambient pressure reduces to a rather low level. But they are still believed to have better cavitation performances as the design expectations in terms of the head drop NPSH condition rather than the required NPSH evaluated by the cavitation inception. The low pressure regions as well as the cavitation regions can be well limited on the blade suction surfaces due to the positive incidence angle design in RR3 rear rotors as can be seen later by the steady cavitation simulations in the next section. Avoiding cavitation on pressure side is supposed to be beneficial to delay the head drop against decreasing NPSH.

In contrast, the RR2 rear rotor, which showed the negative incidence angles in its whole spanwise range (Fig. 3-4), is supposed to be loaded at the blade aft part and have low pressure regions on the pressure surfaces. With the ambient pressure reducing to a rather low level, it would suffer cavitation at both suction and pressure surfaces, which significantly deteriorate the pressure distribution on its blade surfaces as well as the hydraulic performances. By the pressure distribution studies for the two types of rotor pairs, which would be presented in Chapter 5, these predictions are pertinently confirmed.

Among three types of RR3 rear rotors, the RR3-Z appeared with the lowest value of $NPSH_r$ as shown in Fig. 3-13, which indicates the best cavitation performance in terms of cavitation inception. Designed with the integrated inlet velocity profile and the varying maximum camber

location along the span as described in Table 3-7, this type of rear rotor presented the smaller attack angles in the hub region and the larger ones in the tip region. In contrast, with large attack angles in the whole spanwise range, the RR3-40 type is supposed to have rather large blade loading as well as the fairly low minimum pressure on its blades, which would result in earlier cavitation inception (Fig. 3-13).

By now as the design expectations, the RR3-Z with several design ideas applied seems to be a good compromise between the hydraulic performances and the cavitation performances. To further validate the design methodology proposed above, the RR3-Z type is manufactured and its relevant performances are pertinently studied by both the experimental and CFD approaches. From the schematic view of RR3-Z rear rotor shown in Fig.3-14, it could be seen that the RR3 rear rotor has reduced stagger angles compared with the prototype RR2 rear rotor. In the following chapters it will be addressed as RR3 for short.

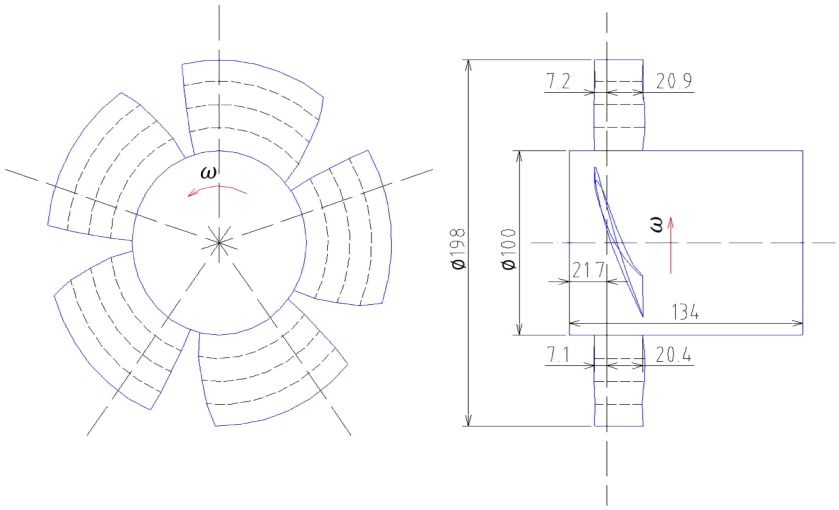

Fig. 3-14 Schematic views of RR3-Z rear rotor

3.3.4 Cavitation simulations with two-phase flow model

A series of steady cavitation simulations with multiphase model applied gave the better visual representation about the cavitation performances of the RR2 rear rotor and newly designed RR3 rear rotor (RR3-Z).

Based on the one-passage steady simulation with the rotor-rotor domain interface set as 'stage' (Sec. 2.3), these cavitation simulations were carried out with the classic Rayleigh-Plesset model employed to describe the growth of gas bubbles [56], which was implemented in ANSYS CFX. The cavitation was triggered at two rotor pairs' design flow rate by reducing the static pressure at the pump outlet.

In Fig. 3-15, for the both contra-rotating rotor pairs under the same inlet static pressure as P_1=17 [kPa], the locations inside the flow passages where the vapor volume fraction grows up to 10% are depicted by the isosurfaces. As predicted in the above section, the cavitation was observed near the leading edge of the pressure surface for the RR2 rear rotor, which would result in remarkable deterioration of the blade loading as well as the pump performances. In contrast, the RR3 rear rotor designed with the positive incidence angles presented the intensive vapor bubbles only limited in small regions around the blade tip and near the leading edge of the suction surface.

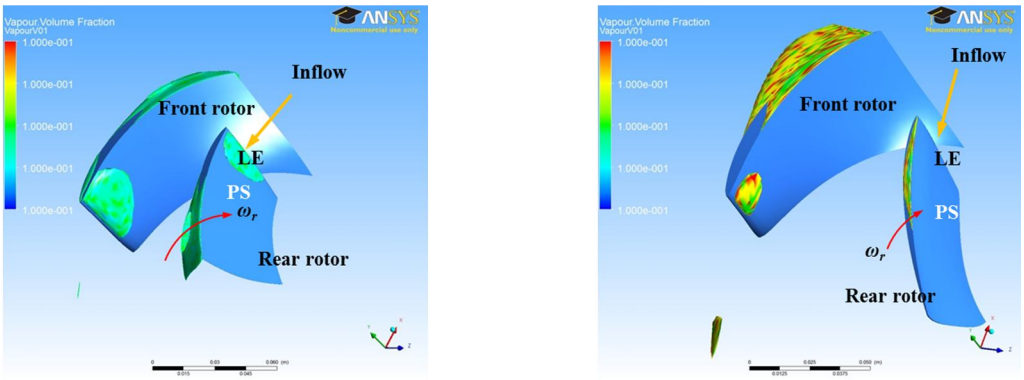

(a) RR2 (b) RR3

Fig. 3-15 Isosurface of vapor volume fraction as 10% in flow passage of contra-rotating rotors

3.4 Summary

In this chapter, the hydraulic performances and internal flow structures of the prototype RR2 contra-rotating rotor pair was analyzed. Designed with the equal rotation speeds for both front and rear rotors, the RR2 rotor pair failed to meet the design specifications, and the both rotors showed the maximum hydraulic efficiencies at the flow rates deviated from the design ones. Based on the findings in the equal speed contra-rotating rotors, the different-speed rotor pair was supposed to be superior in the cavitation performances and the suppression of blade rows interactions. Hence, the different-speed design method was proposed with the cavitation performance improvement emphasized throughout, and the new speed combination with reduced rotation speed for the rear rotor was derived and believed to be beneficial to the cavitation performance of the rear rotor. With the optimized inflow velocity profile, as well as the design ideas of positive incidence angle and secondary flow suppression, the new rear rotor RR3 was found to highly satisfy the design specifications with the superior efficiencies compared to the prototype rotor pair RR2. Although the RR3 was confirmed to have the increased required net positive suction head, which indicates the earlier cavitation inception, it was still supposed to be superior in the cavitation performances since the cavitation could be well limited on the suction surfaces. The other detailed properties about its internal flow and pressure distribution which are essential to the pump performances would be pertinently investigated in the following chapters.

4 Performance investigation for new contra-rotating rotors

This chapter majorly concentrates on the investigations of the hydraulic performances and related internal flow fields of the newly designed contra-rotating rotor pair RR3 (RR3-Z) based on both the experimental and CFD results. The experimentally obtained performance curves are firstly presented, from which it can be found that the new rotor pair RR3 has the impressive performances throughout a rather large flow rate range, but shows a more pronounced positive slope in the low flow rates (Q<28 L/s). The experimental and numerical results of its internal flow properties at such low flow rates are subsequently presented. The internal flow structures obtained by the 5-hole probe measurements at various flow rates are given, and then on the rotor surfaces which were unreachable for the measurements using probes, the limiting streamlines visualized by the multi-colored oil-film method are provided. Finally, based on these investigation results, the underlying sources for the performance deficiencies at such low flow rates are discussed.

4.1 Hydraulic performances of new rotor pair RR3

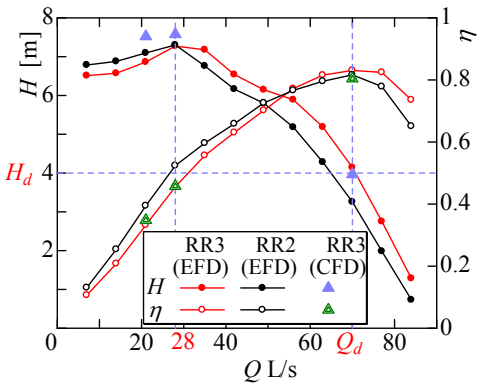

Fig. 4-1 Overall performance curves of contra-rotating rotor pairs RR3 and RR2

In Fig. 4-1, the experimentally acquired overall performance curves are presented for both contra-rotating rotor pairs RR2 and RR3. The unsteady CFD simulation results are also plotted

but only at the flow rates of Q=70 L/s (the design flow rate), 28 L/s, 21 L/s for the new rotor pair. By both the experimental and simulation approaches, the newly designed rotor pair RR3 was confirmed to highly satisfy the design specification (H_d=4.0 m) with a relatively higher efficiency. And in a rather wide flow rate range including Q_d (the design flow rate) (Q>28 L/s), it appeared with the well increased hydraulic head rise over the RR2 type; while in the fairly low flow rate range (Q<28 L/s), it suffered from a more pronounced positive slope on its head curve. In contrast to the favorable head rise, any distinctive benefits in terms of the hydraulic efficiency could not be obtained, and only the limited efficiency improvement could be observed in the high flow rate range (Q≥56 L/s).

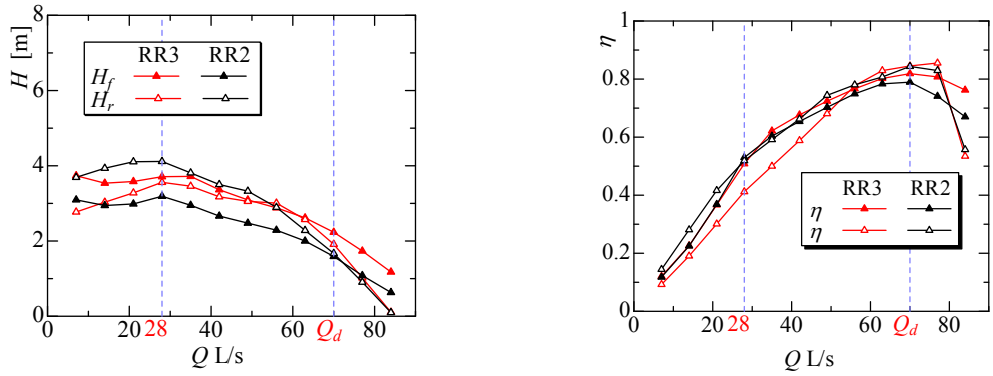

(a) Head performances of each rotors (b) Efficiencies of each rotors

Fig. 4-2 Performance curves of individual rotors in RR3 and RR2 pairs (by experiment)

From the experimentally obtained performance curves of the individual rotors in Fig. 4-2, more benefits of the new rotor pair as well as the different-speed design methodology could be found. The effectiveness of the different-speed design method could be preliminarily reflected by the improved performances of the rear rotor RR3 at the design flow rate, which presented a satisfied head rise and raised efficiency despite being designed with the reduced rotation speed.

It could also be seen that the front and rear rotors appear with quite different hydraulic head properties in two contra-rotating rotor pairs. The front rotor persistently offered the higher head

rise over the rear rotor for almost the whole flow range in the RR3 pair, while in the RR2 pair its head rise was exceeded by that of the rear rotor in the full partial flow range and even at the design flow rate (Q≤70 L/s). As on the head curve of the entire pump, a steeper positive slope was observed on the individual head curve of the RR3 rear rotor in the identical flow rate range, indicating the dominant role of the rear rotor in such performance deficiency.

Working at an increased rotation speed (N_f=1311 min^{-1}) in the RR3 pair, the front rotor operated with the comparable efficiencies in the partial flow rates, and obviously superior efficiencies in the over flow rates in contrast with that in the RR2 pair. Hence, the RR3 pair's efficiency inferiorities in the large partial flow range (Q≥56 L/s) was believed to be ascribed to the rear rotor, which shows well depressed efficiencies in the corresponding flow rate range.

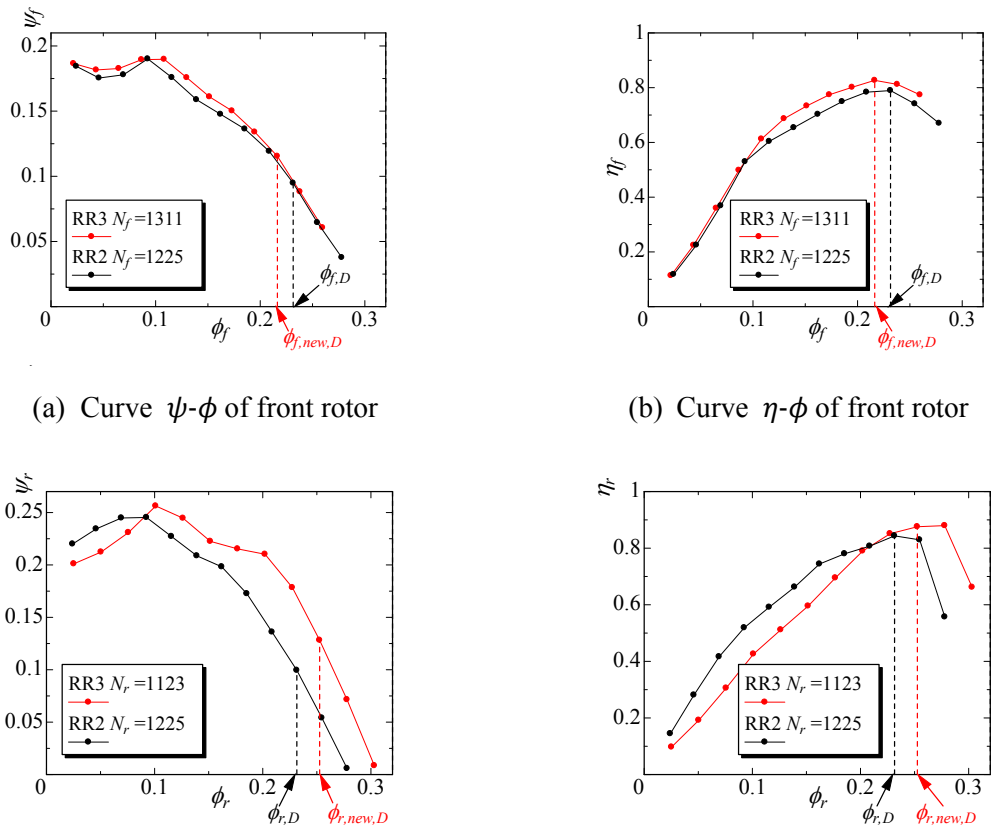

(a) Curve ψ-ϕ of front rotor

(b) Curve η-ϕ of front rotor

(c) Curve ψ-ϕ of rear rotors

(d) Curve η-ϕ of rear rotors

Fig. 4-3 Dimensionless performance curves of individual rotors in RR3 and RR2 (by experiment)

Given the dimensionless performance curves of the individual rotors calculated from the performance tests, the relevant performances of the rotor pairs RR3 and RR2 could be more reasonably compared in Fig. 4-3. Here, ψ and ϕ represents the head and flow coefficients respectively, which were introduced in the previous chapter. The design dimensionless flow rates of the individual rotors are denoted by $\phi_{f,D}$ and $\phi_{r,D}$ for the RR2 pair, while $\phi_{f,new,D}$ and $\phi_{r,new,D}$ for the new RR3 pair.

Since the identical front rotor is applied with two different rotation speeds in the RR2 and RR3 pair, it was supposed to have the consistent dimensionless performance curves (ψ-ϕ and η-ϕ) according to the similarity law [1-5]. While equipped with the new rear rotor RR3 in the downstream, it presented a set of quite varied non-dimensional performance curves as shown in Fig. 4-3 (a) and (b), in which both the working capacity (ψ) and the hydraulic efficiency (η) received obvious improvements in the full flow range. Then, the rear rotor's influences in the upstream direction were pertinently confirmed here, but this does not mean the invalidity of flow similitude, and the head evaluation based on casing wall static pressure may be a reason for this discrepancy. The variations between such two sets of dimensionless performance curves were believed to be the reflections of the effectiveness of different speed rotor design with weakened rear rotor's impacts due to the reduced speed design.

In addition, the new rear rotor moreover showed the sharply improved working capacity in the fairly large flow range (Fig. 4-3 (c)), as being designed with well increased attack angles. Nevertheless, it is quite depressing to see the more pronounced positive slope and the remarkably reduced efficiency in the partial flow range as observed on the dimensional performance curves. To further understand its internal flow properties, the various measurements were carried out and discussed in the following sections.

4.2 Internal flow structures of new rotor pair RR3

The flow field measurements by the 5-hole probe were carried out at the stream locations Pos. 1, Pos. 3 and Pos. 5 (Fig. 2-3). In Fig. 4-4, the velocity distributions at Pos. 3 (the front rotor outlet) are given for the rotor pairs of RR2 and RR3. The measurement results in which only the front rotor was applied are also shown in this figure. To compare the flow profiles in three cases more rationally, the circumferential velocity V_θ is normalized by the blade tip peripheral velocity of the front rotor $U_{t,f} = r_t \omega_f$, and the rotation direction of the front rotor is set to be positive for the circumferential velocities.

4.2.1 Radial distributions of axial velocity at rear rotor inlet section

From the axial velocity components plotted in Fig. 4-4 (a), (c) and (e), the benefits of the oppositely rotating rear rotor could be recognized from the content of the front rotor's hub back flow, which is typical and almost inevitable at the rotor outlet of axial flow pumps under rather low flow rates due to the overwhelming adverse pressure gradient there [58]. It could be found that this back flow appears at larger flow rate in the cases with the rear rotor applied (by comparing the corresponding velocity distributions at Q=42 L/s); nevertheless the growth of such back flow with the reduction of the flow rate is limited only near the hub wall in the cases with the rear rotor and rather uniform flow is observed outside of the back flow region.

In addition, it can also be noticed that the hub back flows of large content will result in the considerable blockage in the flow passages, which in turn induces the sharp increase of the local flow rate in the tip area as shown in Fig. 4-4 (a). While due to the suppression of radial growth of such back flows by the rear rotor, the relatively uniform flow distributions (in radial) could be acquired in the cases of contra-rotating rotors.

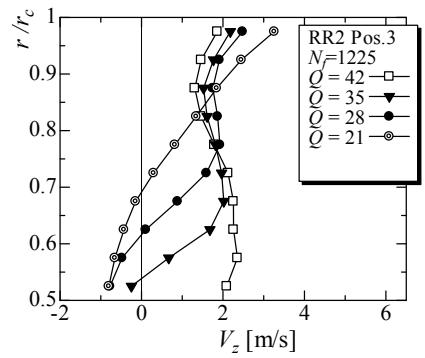

(a) Pos.3: V_z – Front rotor only

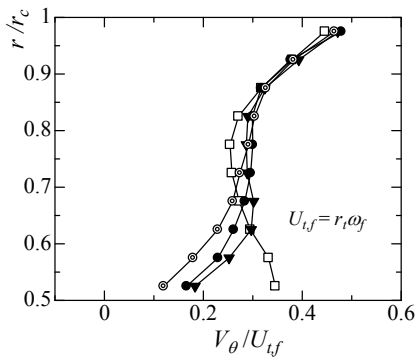

(b) Pos.3: $V_\theta/U_{t,f}$ – Front rotor only

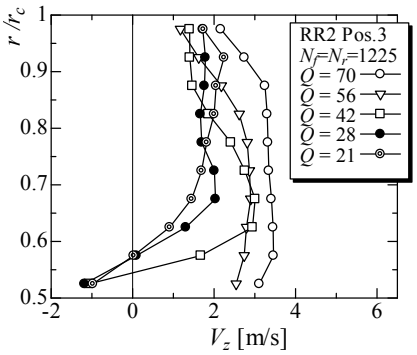

(c) Pos.3: V_z – RR2 pair

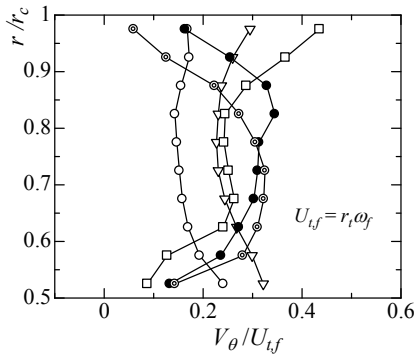

(d) Pos.3: $V_\theta/U_{t,f}$ – RR2 pair

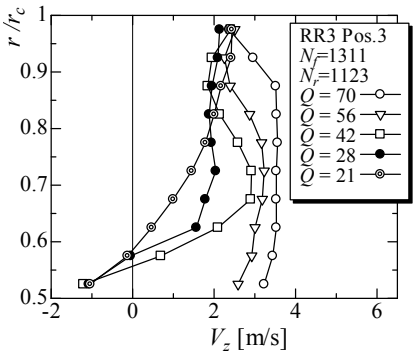

(e) Pos.3: V_z – RR3 pair

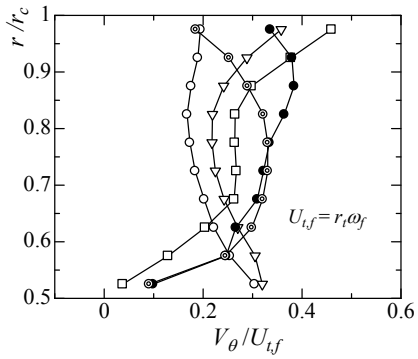

(f) Pos.3: $V_\theta/U_{t,f}$ – RR3 pair

Fig. 4-4 Velocity distributions at Pos. 3 in Front rotor only, RR2 and RR3 (by experiment)

4.2.2 Radial distributions of circumferential velocity at rear rotor inlet section

Comparing the velocity distributions in Fig. 4-4 (b), (d) and (f), the influences from the different type of rear rotors could be better understood. Basically, with the reduction of the flow rate, the circumferential velocity V_θ as well as the theoretical Euler head ($V_\theta/U_{t,f}$) are consequently raised especially in the tip area, where the flow inlet angles are relatively larger. But the actual velocity variations along the radial direction usually turn to be rather non-uniform due to the complicated flow structures. From the case that only the front rotor is applied the circumferential velocities are remarkably increased in the upper span region at Pos. 3, while in the both contra-rotating rotors such velocity components reveal a tendency to reduce with the flow rate descending to a rather low level.

From the rotors' geometries schematically illustrated in Fig. 2-3, it can be found that the front rotor takes the gradually decreasing length in axial from the root to the tip, and its exact outlet location is being further from the section Pos. 3. With the larger radius, the rear rotor presents subsequently stronger angular momentum in its rotating direction, and poses strong entrainment on the flow near to its leading edge (LE). Thus, when the flow rate descends to a sufficiently low level, such entrainment effect becomes strong enough to overcome the fluid's inertia, and is believed to result in the circumferential velocity reduction in the upper span region at this section.

Such reduction in V_θ around the tip area can be observed in the cases of Q=28 L/s and Q=21 L/s for both rotor pairs, and in the RR2 pair the decrease is supposed to start at much higher flow rate around Q=35 L/s. Thus, compared with the RR2 type, the new rear rotor RR3 is believed to place a relatively weakened entrainment on the flow at its inlet section, as well as the less influences in the upstream direction.

4.2.3 Flow distributions at rear rotor outlet section

In Fig. 4-5, the corresponding velocity distributions at Pos. 4 (the downstream of rear rotor) in the rotor pairs of RR3 and RR2 are presented, and due to the shortage of the data in the RR2 pair at some flow rates only the velocities at rather low flow rates Q=28 L/s and Q=21 L/s are plotted.

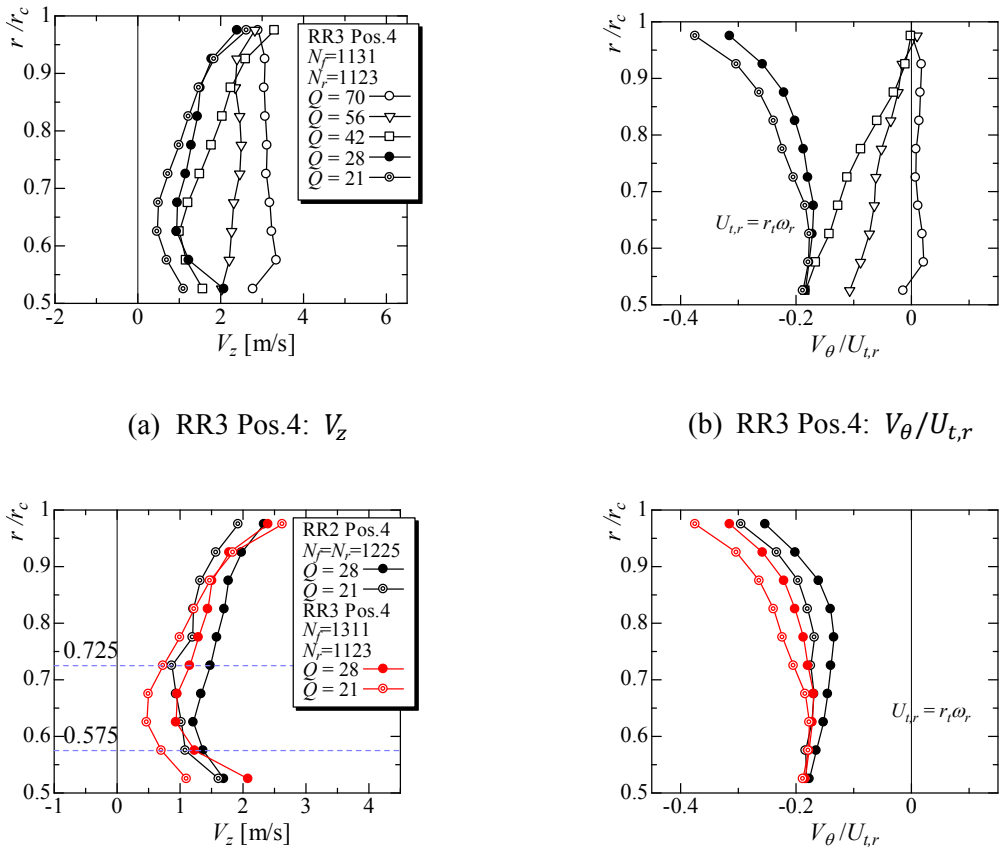

(a) RR3 Pos.4: V_z

(b) RR3 Pos.4: $V_\theta/U_{t,r}$

(c) RR3 & RR2, Pos.4: V_z

(d) RR3 & RR2, Pos.4: $V_\theta/U_{t,r}$

Fig. 4-5 Velocity distributions at Pos. 4 in RR2 and RR3 (by experiment)

At the outlet of rear rotor RR3, the non-swirl outflow situation could be basically obtained at the design flow rate Q=70 L/s as shown in Fig. 4-5 (b). And coinciding with the performance curves, the magnitude of circumferential velocities grows continuously with the reduction of flow rate. In addition, with the increase of the front rotor's hydraulic head rise, the flow in the

upper span region gains the very large circumferential velocity at the outlet section, at the flow rates of Q=28 L/s and Q=21 L/s.

From two rear rotors' inflow distributions in Fig. 4-4 (d) and (f) and outflow profiles in Fig. 4-5 (d), it can be easily found that even at the rather low flow rates (Q≤28 L/s), the RR3 rotor is capable to achieve the relatively larger flow turning ($\Delta V_\theta / U_t$). In other words, it is still believed to be superior to the RR2 type in transferring theoretical energy gH_{th} to fluid at such low flow rates. Combining with the rear rotor's performance curves in Fig. 4-3, this finding convincingly suggests that the lower hydraulic heads and efficiencies of RR3 observed in this range are not ascribed to its inherent inferior working capacity, but to any undiscovered loss mechanisms.

Moreover at such two flow rates, the axial velocity deficiencies could also been observed at the outlet sections of the both rear rotors as shown in Fig. 4-5 (a) and (c). The deficiencies concentrate in the relatively lower span range (about $0.575r_c<r<0.725r_c$), and due to their blockage effect the passage fluid is pushed more upward, resulting in well increased local flow rate in the upper span area. Compared with the RR2 type, the RR3 rear rotor suffers from such velocity decay much earlier and significantly. At Q=21 L/s, its blockage grows rather severe and large mass of fluid is consequently pushed into the near-shroud region.

Based on all above findings, the reason for the RR3's inferior hydraulic performances in the rather low flow rate range was believed to lie in its outflow condition. The velocity deficiencies at its outlet section were supposed to stem from the low speed fluid stacking there, which caused huge energy losses and eventually resulted in a more pronounced positive slope on the performance curve. Although the RR2 type is relatively inferior in working capacity, the less severe passage blockage and lower consequent losses made it perform much favorably in this flow rate range. To further validate this idea, the limiting streamline observations experiments were carried out as described in the following sections.

4.3 Boundary layer investigation

In the above sections, the flow fields measured by the 5-hole probe were discussed for two contra-rotating rotor pairs. Their internal flow structures especially at the rather low flow rates were confirmed to be highly complicated with a large mass of low-momentum fluid stacking inside the passage. To further understand such internal flow structures and the associated loss mechanisms, it is imperative to extend researches into the boundary layer flows at the rotor solid surfaces, since they are known as the essential origins of any flow turbulences and secondary flow structures [1-5].

Besides by the CFD approaches, the boundary layer's properties in the contra-rotating axial flow pump were also studied by the experiment methods. Since those solid surfaces are unreachable for the 5-hole probe measurement, the multi-color oil-film method was adopted to visualize the limiting streamlines in the rotors' boundary layers.

4.3.1 Limiting streamline observation by multi-color oil-film method

The multi-color oil-film method [63-65] is a very effective experimental way to visualize the limiting streamlines in the boundary layers by taking advantage of the oil pigment's grip on the solid surfaces.

Before the experiments, all of the surfaces of the front and rear rotors were carefully cleaned, and were undercoated by matte white using the spraying lacquer. Then, they were respectively coated with the well compounded oil-film pigments of various colors, the viscosity of which is adjusted depending on the assumed local flow velocity. And then, the pump would operate at the required flow rate with the nominal rotation speed for a certain time duration, which must be sufficient for the oil-film to comprehensively track the motion of boundary layer fluid, and also be relatively short to obtain the distinctive pictures before all the pigment are

washed away.

The oil-films were prepared by mixing the fluorescent pigment of three colors (red, blue, and yellow) with the Petroleum Hydrocarbons based lubricating oil used as solvent, the Oleic acid used as the dispersion and grease for the adjustment of stickiness. In Table 4-1, one of the oil-film recipes is given, and the mass ratio of each ingredient might be altered depending on the specific flow rate and the rotation speed of rotors. Based on the viscosity of such oil-films, three minutes of stable operation at certain constant values of Q, N_f and N_r (pump starting stage excluded) was confirmed to be an appropriate choice to obtain the sufficiently clear limiting streamlines.

Table 4-1 Oil-film ingredients for various rotor surfaces Q=28L/s

Location	Solvent Ingredient	Mass Ratio	Fluorescent Color	Mass Ratio	Dispersion Ingredient	Mass Ratio
Pressure Surface	Petroleum Hydrocarbons Based Lubricating Oil	11.8%	Blue	26.7%	Oleic Acid	34.8%
			Yellow	26.7%		
Suction Surface		15.2%	Red	56.8%		28.0%
Hub Surface		15.4%	Blue	57.1%		27.4%

The rotor pair's surface painting before and after the pump operation is shown in Fig. 4-6, and on photo (b) the secondary flow structures could be clearly observed as the hub painting brought upon the suction surfaces.

In the following sections, the experimentally obtained limiting streamlines are presented together with the CFD simulation results. To validate the previous prediction for the loss mechanism in the RR3 rotor pair, only the findings at the correlative low flow rates are discussed here.

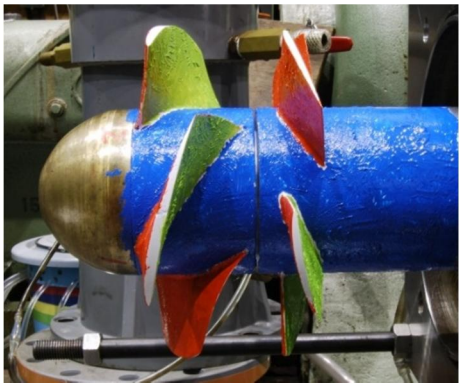

(a) Before pump operation

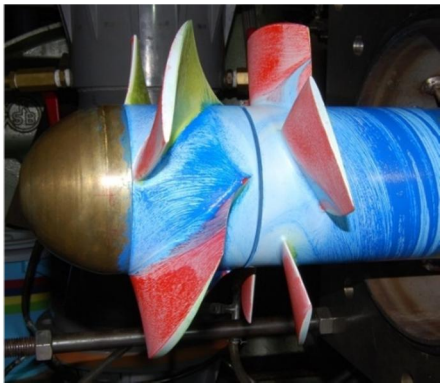

(b) After pump operation

Fig. 4-6 Limiting streamlines observation experiment

4.3.2 Limiting streamlines of front rotor at low flow rate

In contrast with the rear rotor RR3, the front rotor showed the relatively stable performance curves even at the rather low flow rates (Fig. 4-3), and its internal flow structure was believed to be less complicated compared with that of the rear rotor. The experiment and CFD results only at the typical flow rate Q=28L/s are presented in this section.

As previously mentioned in Sec. 4.2, the internal flow field of the front rotor at such low flow rate is majorly characterized by the hub back flow at its outlet. In Fig. 4-7, such hub back flow could be clearly recognized as the streamlines marked by ④, along which the flow goes in the opposite direction to the passage mainstream. It induces the severe blockage at the lower span area in full circumference, and results in the obvious boundary layer separation on the hub surface as marked by the dashed lines. The another typical tip back flow at the rotor inlet can also be captured as ①, and consequently the main passage flow is forced to advance more radially outer as marked in Fig. 4-7 (a) and (b).

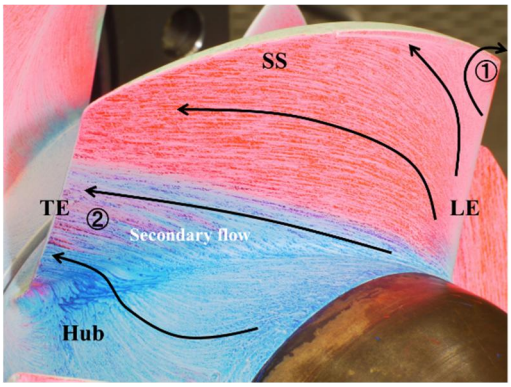

(a) Front rotor's suction surface - Exp

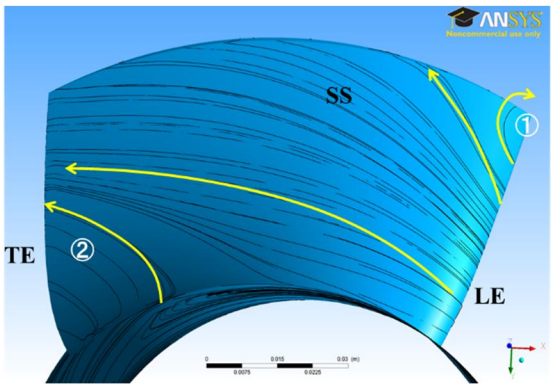

(b) Front rotor's suction surface - CFD

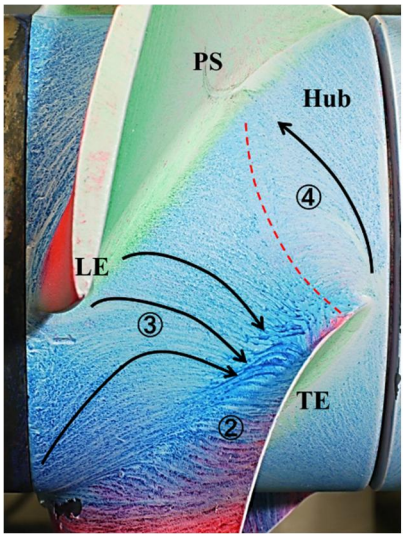

(c) Front rotor's hub surface - Exp

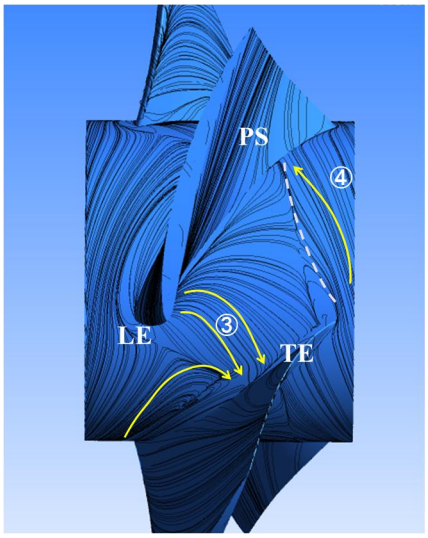

(d) Front rotor's hub surface - CFD

Fig. 4-7 Limiting streamlines on front rotor's surface at Q=28L/s

In addition, the secondary flow structures could be clearly observed in the front rotor's passage as ② and ③. Due to the overwhelming pressure gradient from one blade's pressure surface (PS) to the suction surface (SS) of its neighbor blade, the low-momentum fluid in the hub boundary layer is pushed to move almost perpendicular to the passage mainstream as marked by ③, and eventually get out the passage at the mid span part of the neighbor blade's trailing edge as ②. The incoming flow in the hub region of the passage is then obstructed, and

finally joins in such secondary flow onto the suction surface.

Generally, the both experimental and CFD investigation approaches provided the highly resembled flow patterns in the front rotor's boundary layers. And at such low flow rate, the front rotor was confirmed with several well-developed back flows and secondary flow structures as previously captured by the 5-hole probe measurement.

4.3.3 Limiting streamlines of RR3 rear rotor at low flow rate

Since the rear rotor was believed to be the major reason for the sharply increased pump losses at the low flow rates Q<28L/s, its internal flow fields were well investigated in this flow range. Firstly, the limiting streamlines at Q=28L/s obtained by both investigation approaches are presented in Fig. 4-8.

At this flow rate, a rather powerful secondary flow structure can be observed covering nearly half of the RR3's suction surface as marked by ①. It aggressively rises upwards from the hub area, and resists against the passage mainstream forming a clear separation line 'A' between them. It is believed to be driven by a remarkably large pressure gradient, and also take over considerable passage content in circumferential. Combining with the flow profiles captured by the 5-hole probe at the rear rotor outlet (Fig. 4-5), this flow structure is the most likely associated with the velocity deficiencies there. Moreover, a small mass of fluid ② from the pressure surface is also found turning around the trailing edge, but is soon pushed out by the powerful secondary flow.

In addition, it's rather surprised to see the secondary flows on pressure surface as ③ and ④ near the blade root. Such two flows ③ and ④ separate at the aft part (marked by 'C') of the hub profile, and go upstream and downstream respectively. They are relatively weak and dominate only a narrow radial space around the blade hub area.

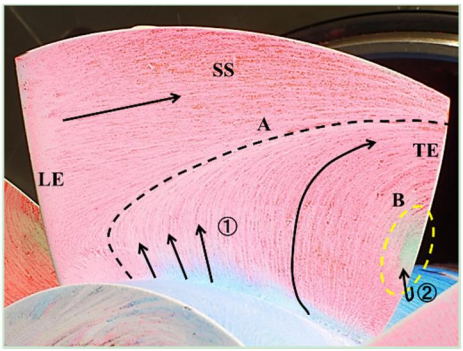

(a) RR3 rear rotor's suction surface - Exp

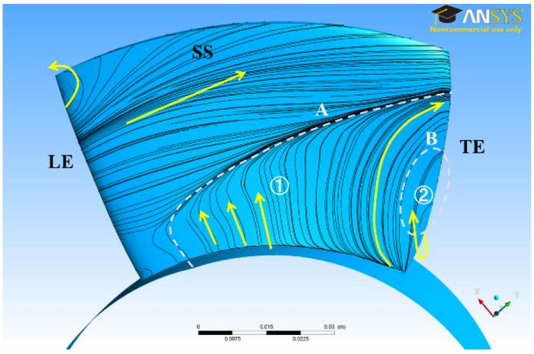

(b) RR3 rear rotor's suction surface - CFD

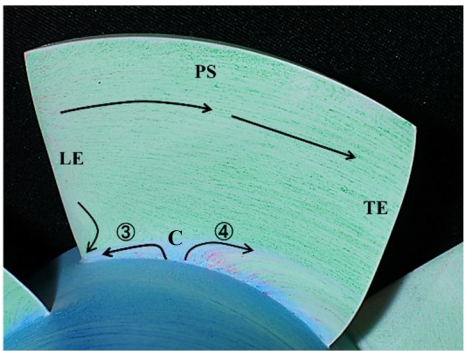

(c) RR3 rear rotor's pressure surface - Exp

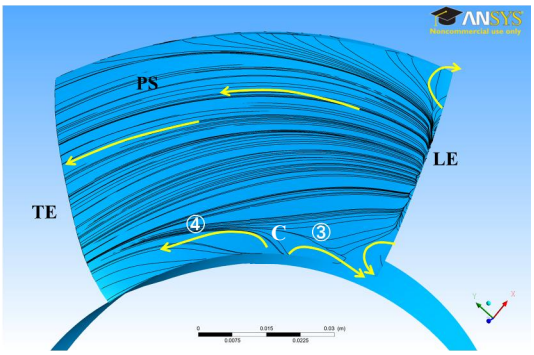

(d) RR3 rear rotor's pressure surface - CFD

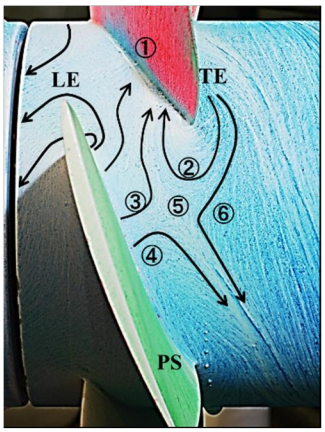

(e) RR3 rear rotor's hub surface - Exp

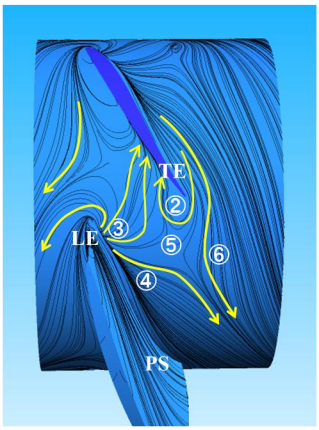

(f) RR3 rear rotor's hub surface - CFD

Fig. 4-8 Limiting streamlines on RR3 rear rotor's surface at Q=28L/s

Seen from the hub surface, the complex flow patterns described above could be better understood. Generally, compared to the front rotor, the rear rotor presents the highly complicated streamlines covering on its hub area. As measured by the 5-hole probe (Fig. 4-4),

the front rotor's hub back flow is still influential at the rear rotor's leading edge (LE). Under such low flow rate, the stagnation points on the rear rotor blades are supposed to locate more downstream from LE due to the well increased attack angles. Thus, the secondary flows ③ and ④ are recognized as the streamlines go along the blade profile of the hub section separating at the stagnation point C.

The flow ④ merges with the flow from the adjacent blade ⑥, and then continues to go downstream as a part of passage outflow. While some of flow ③ is driven to the opposite blade suction surface by the overwhelming pressure gradient, and then joins in the boundary layer flow ② near the hub surface which turns around the trailing edge of the adjacent blade. The integrated flow continues to raise radially outward on this suction surface, and eventually results in the secondary flow structure ① observed above. On the hub surface, the four flow streams (②, ③, ④ and ⑥) diverge from each other, and a clear saddle point ⑤ can been observed. The region around this point is supposed to have well reduced axial velocity and pose the significant blockage inside the flow passage.

In general, taking account of all the passage boundaries, one can obtain a full view of such significant secondary flow. By reducing the flow rate, the blade loading is consequently increased, and the pressure difference between the pressure surface (PS) and the suction surface (SS) of each blade is increased for the fore part of the blade. Moreover, the hub back flow at the front rotor's outlet makes the inlet flow rate of the rear rotor in the near hub region pertinently reduced. Hence, the adverse pressure gradient on the rear rotor's suction surface becomes remarkably significant in the near hub region, which results in the thickening of the boundary layer in the corresponding area. In such condition, the passage secondary flows emerge majorly as: 1) the boundary layer separation on the SS due to the overwhelming adverse pressure gradient, 2) the low-momentum fluid in one blade's hub boundary layer is driven to the SS of

the neighboring blade as ③, 3) the boundary layer fluid at one blade's PS turns around the trailing edge toward the SS of the same blade as ②.

Overall, with the flow rate descending to such low level less than 28 L/s, which is 40% of the design flow rate Q_d, any of these secondary flows is supposed to be remarkably developed and result in severe passage blockage. The internal flow fields as well as the pump performances in turn rapidly deteriorate as described on the performance curves in Fig. 4-3. Considering these secondary flow structures as the major loss mechanisms, the similar secondary flow structures had also been found in the RR2 rotor pair [65]. But compared with the RR2 type, the RR3 rotor pair designed with the increased attack angle (Table 3-7) has relatively larger blade loading even under the identical flow rate, and therefore suffers from the flow field and performance deterioration more significantly. On the performance curves in Fig. 4-3, it could be found that the rear rotor RR3 shows the superior head rises but the inferior hydraulic efficiencies in a rather wide partial flow range. Moreover with the flow rate further decreased, its hydraulic head starts to drop due to the highly deteriorated internal flow field.

In order to understand the rapidly reduced pump performance as well as the steeper positive slope on RR3's head curve, the experimentally obtained limiting streamlines at Q=21L/s are presented in Fig. 4-9.

By reducing the flow rate from Q=28 L/s to Q=21 L/s, the secondary flow on SS appears with the leading location more upstream, but its region is unexpectedly narrowed in spanwise, and moreover the boundary layer fluid turning around the trailing edge (in region B) becomes more significant. In other words, due to the pertinently enhanced adverse pressure gradient, the boundary layer on the suction surface separates more upstream resulting in more passage flow near the hub surface enrolled into the secondary flow structure. From the hub streamlines, such secondary flow ③ can be observed to be reinforced, and go much more upstream of the

adjacent blade's suction surface. In addition, the low-momentum region ⑤ around the saddle point also appears to be enlarged.

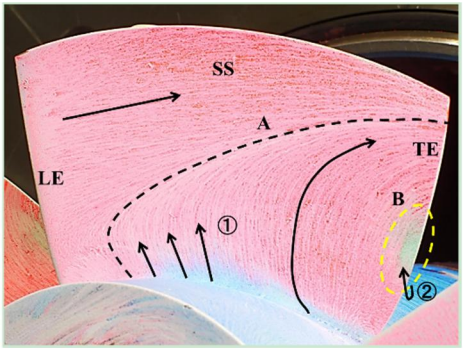

(a) RR3 rear rotor's SS at Q=28L/s

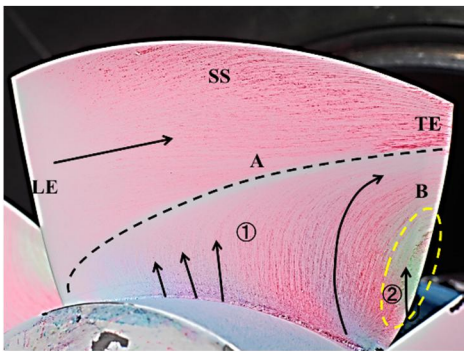

(b) RR3 rear rotor's SS at Q=21L/s

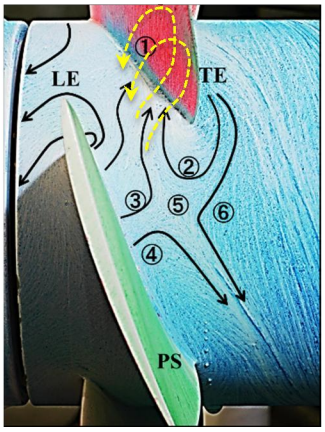

(c) RR3 rear rotor's hub surface at Q=28L/s

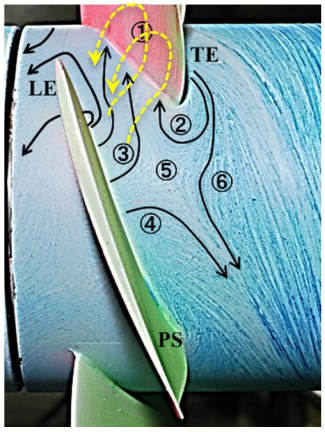

(d) RR3 rear rotor's hub surface at Q=21L/s

Fig. 4-9 Limiting streamlines on RR3 rear rotor's surface at Q=28L/s and 21L/s

4.3.4 Tip leakage vortices obtained by numerical simulations

Reproducing the detailed internal flow fields by the CFD simulations, the better understanding can be obtained for the secondary flow structures under the low flow rates. In Fig. 4-10, the contour maps of V_z and surface velocity vectors on several meridional planes inside the RR3's passage are presented.

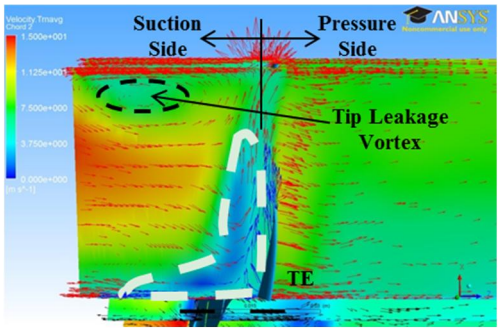

(a) RR3 rear rotor's TE at Q=28L/s

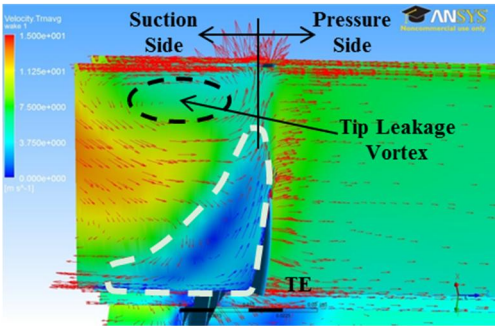

(b) RR3 rear rotor's TE at Q=21L/s

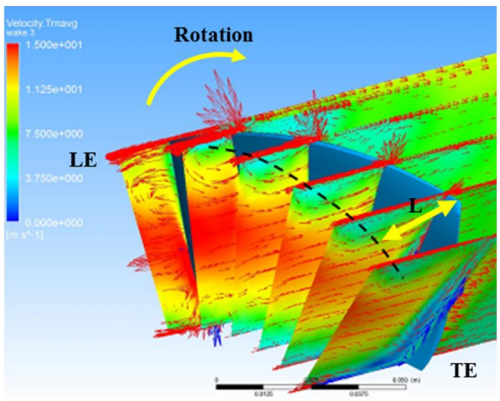

(c) RR3 rear rotor's passage at Q=28L/s

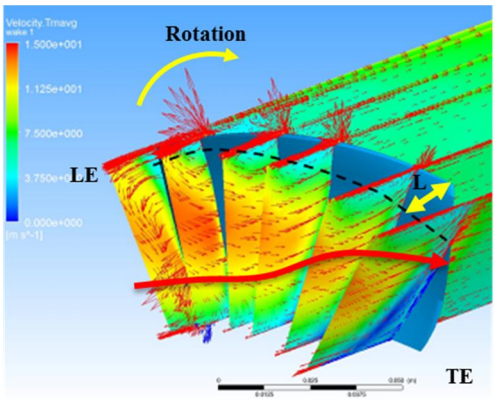

(d) RR3 rear rotor's passage at Q=21L/s

Fig. 4-10 Contour maps of V_z and surface velocity vectors on several meridional planes

On these contour maps, a large mass of low-momentum fluid can be identified with its low velocity magnitude (marked in blue). As estimated by the experiments, it majorly stacks at the hub-SS (suction surface) corner and takes the increasing volume along the chordwise direction, and it has developed into a considerable blockage by the blade trailing edge. With the calculated surface velocity vectors, the flow directions inside such fluid mass could be clearly identified as follows: the secondary flow streams originate from the hub-PS (pressure surface) area of the adjacent blade to the hub-SS region of the present blade, and then move radially upon the SS until its mid-span part, and eventually exit the flow passage.

All of these findings indicate the severely thickened and separated boundary layer at the aft part of the suction surface, and the subsequently emerged secondary flows under the significant

pressure gradient. Combining with the observations from the previous experiment results, such complex internal flow patterns and its induced severe passage blockage could be confidently validated to be the major loss mechanisms for the RR3 rear rotor in the low flow rate range.

In addition, with the CFD technology, the tip leakage vortex can also be well visualized. As shown in Fig. 4-10, it could be recognized in the near-shroud region, as the areas (marked by black dashed lines) of the relatively low velocities and the velocity vectors in circular motion. At these two flow rates, due to the significant pressure difference between the PS and SS, the tip leakage vortices emerge very close to the blade leading edge, and also pose severe blockage in the flow passages. Here, the mechanisms of this type of flow phenomenon still remains unknown, but it could be emphasized that with the increase of blade loading due to the flow rate reduction, the tip leakage vortex usually appears to be well reinforced and be more detached from the suction surface [66-69]. On the contrary, for the rear rotor of this contra-rotating axial flow pump, by reducing the flow rate from Q=28L/s to Q=21L/s, the tip leakage vortex of RR3 blade switched to be more close to the suction surface as shown in Fig. 4-10.

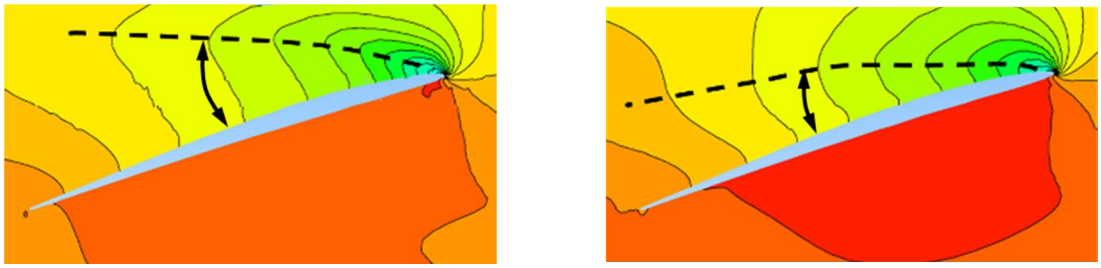

(a) At Q=28L/s (b) At Q=21L/s

Fig. 4-11 RR3 rear rotor's static pressure contours at cylindrical surface of r/r_c=0.975

The static pressure contours at the near-tip cylindrical surface in Fig. 4-11 better describe such unexpected variation. On these contours, the tip vortices could be easily recognized by the low pressure trough (marked by black dashed lines) due to the remarkable static pressure reduction in their vortex cores [68].

With the flow rate descending to $0.4Q_d$ (Q=28L/s), the blade loading especially at the tip profiles increases to a rather high level, and the tip leakage vortices are in turn significantly enhanced and remarkably detached from the suction surfaces. As shown in Fig. 4-11 (a), due to the inherent large stagger angles of the rear rotor, the more detached tip leakage vortices are capable to get out of the flow passages at this flow rate. Further reducing the flow rate to $0.3Q_d$ (Q=21L/s), it was expected that the tip leakage vortices would get more upstream, but it is interesting to see that those get back into the blade passages as illustrated in Fig. 4-11 (b), indicating the reduced blade loading in the tip region.

Combining with the V_z distributions at the rear rotor inlet (Fig. 4-4 (e)) and outlet (Fig. 4-5 (c)), one can understand better about this loading reduction. Despite of the well reduced average flow rate, RR3 shows the local flow rate increase in the near-shroud region, due to the various blockages in the lower part of the passage. Such increase generally starts from Q=42L/s. Based on these velocity distributions, the rear rotors' incidence angle distributions can be calculated and is shown in Fig. 4-12.

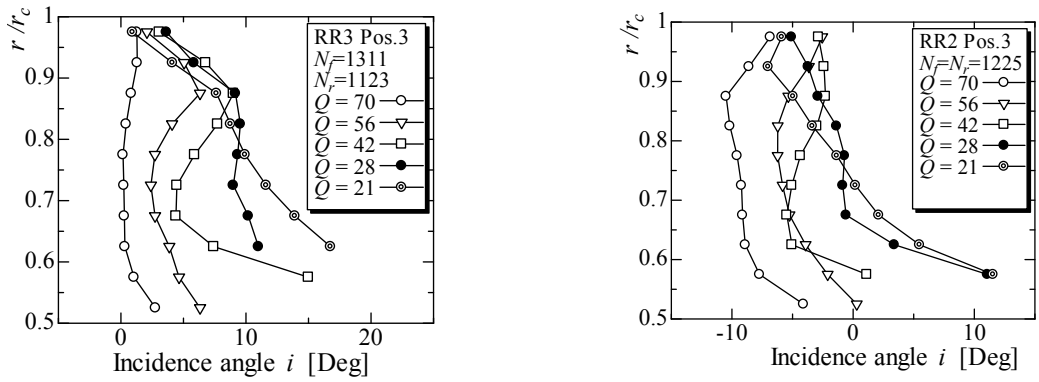

(a) RR3 (b) RR2

Fig. 4-12 Incidence angle distributions of rear rotors in RR3 and RR2 pairs

Consistent with its superior work capacity, the RR3 type presents the highly increased incidence angles in the full flow range compared to the RR2 type. Generally, the incidence

angle continuously increases with the reduction of the flow rate; while in the presence of several complex flow structures with the flow rates less than Q=42L/s, it does not follow this way. When the flow rate descends to the rather low level, the both rear rotors show the decreased incidence angles around their tip area, which implies the reduced blade loading at the corresponding locations. This coincides with the findings of the local flow rate increase, which pertinently explains the tip leakage vortex's behavior of getting back into the flow passage at Q=21L/s for the RR3 rear rotor.

4.4 Summary

By now for the RR3 rear rotor which was designed with the rather large attack angles, the existence of the significant secondary flow structures has been confirmed by both the experimental and simulation approaches. They are majorly attributed to the remarkable blade loading as well as the overwhelming pressure gradient inside the flow passage, and then result in the severe passage blockage and the deterioration of pump performances. When the pump discharge further reduces to a rather low level, the local flow rate near the tip region is sharply increased due to the serious blockage in the lower part of the flow passage, inducing the decreased blade loading at the corresponding location. The tip leakage vortex consequently gets back into the passage and poses another considerable passage blockage, resulting in more rapid pump performance deterioration as well as the remarkable positive slope of the head curve.

5 Rotor-rotor interactions in new contra-rotating rotors

As mentioned in the introduction, the rotor-rotor combinations are usually characterized by the relatively significant interactions between two blade rows, and their suppressions have become one of the important design factors for various types of contra-rotating rotor-rotor applications. In the design stage of the present new contra-rotating axial flow pump, the optimization of the blade-to-blade pressure distributions as well as the suppression of the potential interactions between the two rotors are also emphasized. This chapter majorly concentrates on the experimental findings about the blade rows interactions in the newly designed contra-rotating rotor pair. As the major experimental approaches in the blade rows interaction investigations, the casing wall static pressure measurement methods are firstly introduced. Then, the axial distributions of the pressure fluctuation strength of the Blade Passing Frequency (BPF) components in two types of contra-rotating rotor pairs are presented. And moreover, the pressure fluctuation modes with the frequencies both synchronous and non-synchronous to the BPF components are discussed. By transferring the casing wall pressure data sampled in time domain into space domain, the ensemble averaged blade-to-blade pressure distributions at the blade tip of two contra-rotating rotors are studied, and the associated blade loading curves are presented.

5.1 Casing wall static pressure measurements

5.1.1 Overview of casing wall pressure measurement experiments

Due to its close proximity to the blade tip, the casing wall has long been known for its informative pressure field data, and the various internal flow properties could be investigated from them. By means of the frequency spectrum analyses on the pressure data measured at the

casing wall, Kameier, F. et al. investigated the tip clearance noises and associated rotating instabilities for the axial flow turbomachines [70]. Yamamoto, A. et al. researched the tip leakage flow and the rotor-stator interactions inside an axial flow turbine by measuring the casing wall pressure distribution using high response pressure transducers [71].

In the present chapter, the blade rows interactions and the associated flow field properties are well investigated by taking advantage of the pressure measured on the pump casing wall. Two measurement methods were employed respectively for the pressure fluctuation investigation and the establishment of the blade-to-blade pressure fields as shown in Table 5-1. Basically, they shared the sixteen major pressure taps (Ch1~16) which cover from the upstream to the downstream of the rotor pair as illustrated in Fig. 5-1, and the other five taps A1~3 and A5~6 were only adopted for the correlation analysis on pressure fluctuation modes.

Table 5-1 Two pressure measurement methods

Measurement Method	Pressure Fluctuation Measurement (PFTM)		Pressure Field Measurement (PFEM)
Purpose	BPF Distribution Investigation	Correlation Analysis	Blade-to-Blade Pressure Field Establishment
Pressure Taps	Ch1~16	A1~6	Ch1~16
Pressure Transducers	PGMC-A-200KP	PGMC-A-200KP	PGMC-A-200KP
Amplifier	DPM-603A	DPM-603A	DPM-603A
A/D Program	Continuous Sampling	Continuous Sampling	Rotor Location Triggering

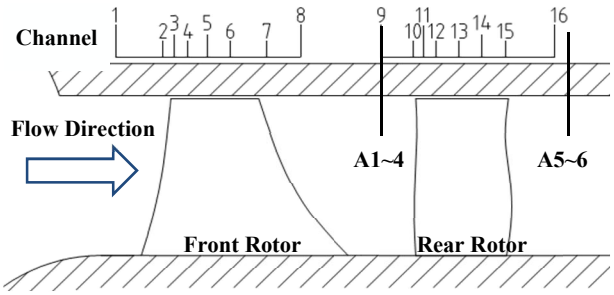

(a) Axial locations of pressure taps

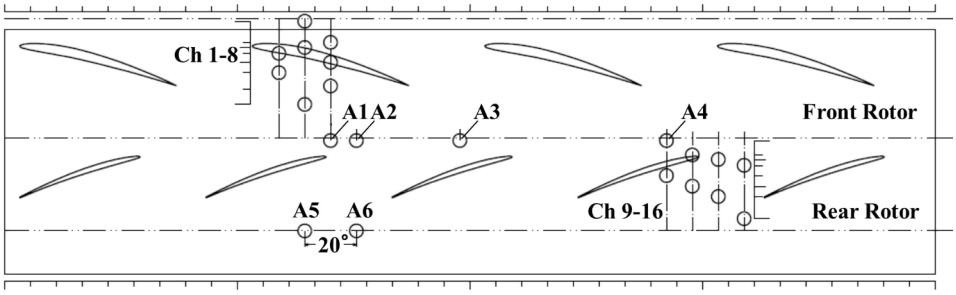

(b) Pressure taps on cylindrically developed casing wall

Fig. 5-1 Distributions of pressure taps for contra-rotating rotor pair RR3

The identical types of pressure transducers (PGMC-A-200KP) and amplifiers (DPM-603A) were used for all these measurements, but the pressure data acquisition programs for pressure fluctuation measurement (PFTM) and pressure field measurement (PFEM) were quite different in terms of trigger timing, sampling frequency, sampling number, etc. Since the amplifier DPM-603A has already been introduced in Chapter 2, here I only give the major specifications of the pressure transducer PGMC-A-200KP in Table 5-2.

Table 5-2 Pressure transducers for casing wall pressure measurements

Pressure Transducers	Model	PGMC-A-200KP
	Rated Capacity	200kPa
	Rated Output	0.6 mV/V (1200μm/m) or more

Nonlinearity	Within ±1.5% RO
Hysteresis	Within ±1.5% RO
Safe Overload Rating	150%
Safe Temperature Range	0 to 50°C

5.1.2 Pressure fluctuation measurement (PFTM)

1) The pressure measurements were firstly conducted by the continuous samplings at Ch1~16 using the strain-gage type pressure transducers. The sampling frequency f_s was determined to correspond to every 2.5 degree rotation of the front rotor which was determined with a higher rotation speed in the RR3 rotor pair, resulting in the sampling time interval as

$$\Delta t = \frac{2.5}{360} \cdot \frac{60}{N_f} = 3.18\text{e-4 second}$$

the sampling number of 8192 was adopted which had been proved sufficient for the frequency spectrum analysis.

2) In expectation of recognizing the pressure fluctuation modes induced by the rotor-rotor interactions as well as capturing the instabilities propagating in the circumferential direction, two series of pressure taps (A1-4, A5-6) with the different peripheral but the identical axial locations were prepared at two sections as shown in Fig. 5-1. The pressure data was firstly acquired at these locations with the above sampling settings, and then processed for the correlation analysis. This is a quite helpful mathematical technology to identify the pressure fluctuation modes resulted from the rotor-rotor interactions by reading their phase differences at any two peripheral locations, and the details of this method will be explained in the following sections.

5.1.3 Pressure field measurement (PFEM)

1) Measurement concept

By now, numerous researchers have experienced establishing the ensemble averaged distributions for the specific flow characteristics inside the rotating machineries by measuring them synchronized to the rotation of the rotor blade. For examples, with a counting system detecting the rotor blade positions, Ottavy, X. et al. reconstructed the velocity fields under various rotor-stator relative locations for the high speed compressors [72]. Estevadeordal, J. et al. reproduced the flow fields at the certain rotor locations in a low speed axial flow fan by means of a measurement system synchronized to the blade position [73].

Compared with the traditional rotor-stator combinations in their studies, the contra-rotating rotor-rotor case needs one stationary and two non-synchronized rotating frames to be considered, which means the measurement system located in the stationary frame relatively moves in the both two rotating frames. The data acquisition for the ensemble averaging cannot be made only synchronized to one rotating frame, but must be done with the both rotating frames tracked. In that case, the measurement should be carried out under any required spatial relationship between all three frames, to obtain the ensemble averaged flow fields at the corresponding rotor-rotor relative position.

The measurement system for the pressure field measurement (PFEM) is schematically described in Fig. 5-2. The acquisitions of analog signals are initiated by a preconditioned trigger signal, which is given as the reference for the peripheral positions of two rotors, and then are continuously carried out with a given sampling frequency at least during one revolution of the both rotors. This whole process was controlled by the A/D converter equipped in a personal computer. To obtain the blade-to-blade pressure distributions, several sets of trigger signals are required which are generated by the following way.

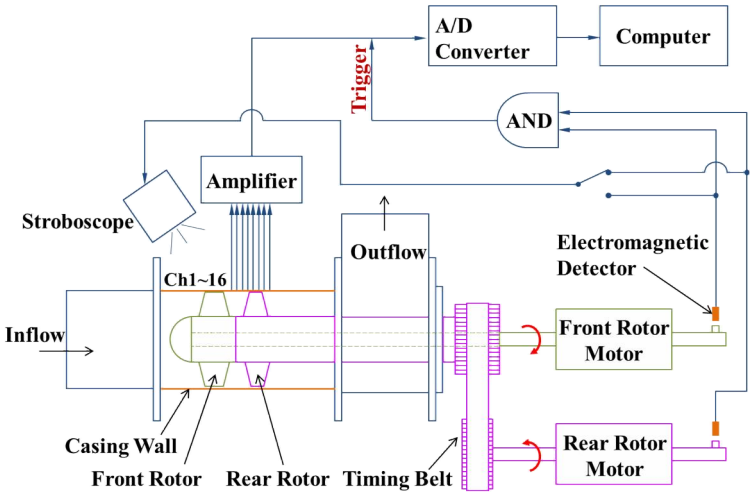

Fig. 5-2 Schematic view of measurement system for PFEM

As shown in Fig. 5-2, at the end of each shaft, an electromagnetic detector (Ono Sokki Co., Ltd, MP-981) is equipped to generate a single pulse signal per revolution of the corresponding motor, and this type of detector has also been employed for the rotor rotation speed monitor system as discussed in Chapter 2. It enables us to adjust the exact timing of pulse generation, i.e., the peripheral position of the respective rotor at arbitrary moment. By using an AND gate for two pulses generated at the preferred peripheral position of the respective rotor, one can obtain a single pulse under any known relative peripheral position between the front and rear rotors, which is then used as the trigger signal for the pressure data acquisitions.

As for the sampling frequency f_s in PFEM, the time duration of 5° relative rotation between the front and the rear rotors is considered as the sampling time interval Δt, which can be calculated as follows,

$$\Delta t = \frac{5}{360} \cdot \frac{60}{N_f + N_r} = 3.42\text{e-}4 \text{ second}$$

Since the spatial relation between the front and the rear rotors changes constantly, it is necessary to collect the data under the identical relative peripheral position $\Delta\theta$ (Fig. 5-3)

between the two rotors to obtain the ensemble averaged blade-to-blade pressure distributions. To do so, it is required to rearrange such time-dependent pressure data measured in the stationary frame, and convert them into the spatial domain by the following procedure.

2) Spatial conversion and data rearrangement

As shown in Fig. 5-3 (a), a reference line in the stationary frame is depicted as a magenta chain line. And then the each rotor's peripheral position in the stationary frame, θ_f and θ_r, can be specified at any instance from the peripheral locations of their respective blade F1 and R1 relative to the reference line, as $\theta_f(t) = \theta_{f0} + \omega_f t$ and $\theta_r(t) = \theta_{r0} - \omega_r t$, where θ_{f0} and θ_{r0} respectively represent the peripheral locations of F1 and R1 at the trigger instance, ω_f and ω_r denote the angular rotating speeds of the front and rear rotors, and t as the time duration after the trigger.

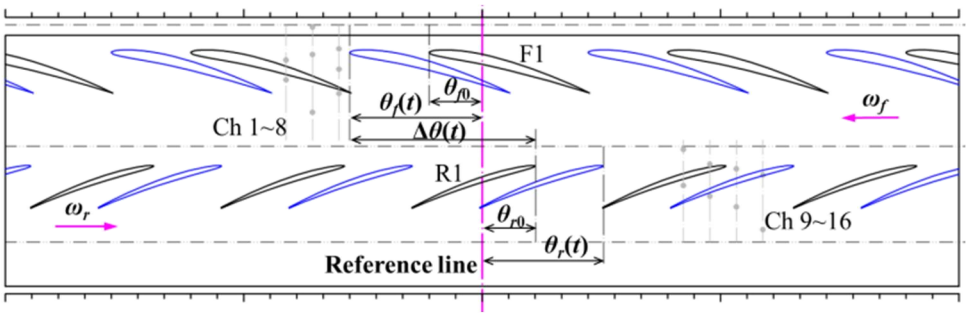

(a) Specification of relevant peripheral positions for both rotors

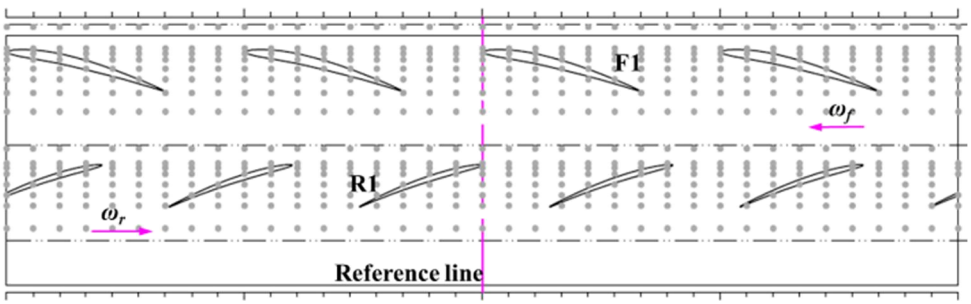

(b) Overall pressure data locations under a relative rotor-rotor position $\Delta\theta$=0

Fig. 5-3 Schematic pressure rearrange methods in PFEM

Hence, the rotor-rotor relative position $\Delta\theta(t)$ at any moment *t* is given as follows, with the rotation direction of the front (rear) rotor set as positive (negative).

$$\Delta\theta(t) = \theta_f(t) - \theta_r(t) = (\theta_{f0} - \theta_{r0}) + (\omega_f + \omega_r)t \tag{5-1}$$

One can basically specify any arbitrary values for θ_{f0} and θ_{r0} by setting the trigger pulse signals individually for the front and the rear rotors. By measuring the time-dependent pressure data with the appropriately determined values of $(\theta_{f0} - \theta_{r0})$ by Eq. (5-2), collecting the data under the identical $\Delta\theta$ but at different time *t*, and then rearranging them into the blade-to-blade domain as demonstrated in Fig. 5-3 (b) (an example for $\Delta\theta$=0), it is possible to acquire any desired blade-to-blade pressure distributions.

$$\theta_{f0} - \theta_{r0} = k(\omega_f + \omega_r)\Delta t = k\times 5^\circ \tag{5-2}$$

In Eq. (5-2), k is an integer with the condition of $k = 2n_m$ (n_m=0, 1, 2,⋯,35), so that the full blade-to-blade pressure distributions in every 10 degrees of $\Delta\theta$ could be obtained in the experiments.

3) Measurement settings for rotor pairs of two rotation speed combinations

With the above considerations, the pressure measurement experiments for the two rotor pairs RR2 and RR3 are specified with the different parameters based on their respective rotation speed combinations as listed in Table 5-3. And each measurement experiment is specified to be repeated at least 10 times for ensemble averaging.

Table 5-3 Pressure measurement settings for RR2 and RR3

	N_f[min^{-1}]	N_r[min^{-1}]	Δt[s]	n_s[-]	n_m[-]
RR2 Pair	1225	1225	3.40136 e-05	144	0 to 35
RR3 Pair	1311	1123	3.42372 e-05	156	0 to 35

5.1.4 Correlation analysis

Based on the Fourier analyses of the time-domain series pressure data $p_x(t)$ measured at the certain pressure tap A_x, as well as the certain peripheral location θ_x, the pressure spectrum $P_x(f)$ could be given as follows,

$$P_x(f) = \int_{-\infty}^{\infty} p_x(t) e^{-j2\pi f t} dt \tag{5-3}$$

To validate the propagation of the critical pressure modes in the peripheral direction, the function of cross spectrum $S_{xy}(f)$ is introduced here as Eq. (5-4).

$$S_{xy}(f) = \int_{-\infty}^{\infty} C_{xy}(\tau) e^{-j2\pi f \tau} d\tau = \lim_{T\to\infty} \frac{1}{T} P_x{}^*(f) P_y(f) \tag{5-4}$$

Based on that, the correlation between the pressure series obtained at any two locations θ_x and θ_y can be investigated. In this equation, $C_{xy}(\tau)$ represents the cross correlation function between the discrete data series p_x and p_y at the time lag τ, and * marks the conjugation of one complex. Then it can be easily understood that, for the certain pressure mode *m* with the frequency *f*, the phase angle $Q_{xy}(f)$ of the above cross spectrum $S_{xy}(f)$, as well as the phase angle difference between two complexes $P_x(f)$ and $P_y(f)$, is capable to represent its propagation speed Ω_m in the peripheral direction.

$$Q_{xy}(f) = Q_y(f) - Q_x(f) = \Omega_m \cdot \tau \tag{5-5}$$

Since *m* also indicates the number of complete waveforms in the duration of 2π, the angular location distance between two pressure taps $\Delta\theta = \theta_y - \theta_x$ could be easily linked with the phase $Q_{xy}(f)$ as the following Eq. (5-6), by which the predicted circumferential pressure modes can be validated using any two series of the pressure data sets.

$$Q_{xy}(f) = m \cdot \Delta\theta \tag{5-6}$$

As an indicator to evaluate the relation between two pressure data sets, the spectral coherence $Coh_{xy}{}^2(f)$ is also introduced as follows.

$$Coh_{xy}{}^2(f) = \frac{\left|S_{xy}(f)\right|^2}{S_{xx}(f)S_{yy}(f)} \tag{5-7}$$

5.2 Prediction of frequency modes associated with rotor-rotor interactions

The frequency spectrum analysis has long been known as a helpful mathematical technique for the flow field investigation. By transferring the time-domain series data of a certain flow property into the frequency domain, it is possible to recognize the impacts from any other physical processes by the associated frequency components. This flow property could be pressure, velocity or other typical characteristics obtained at any critical location. In the rotating machineries, the influences associated with the individual rotor can be recognized by the well-known frequency component BPF (blade passing frequency), which is determined by the blade number and rotor speed. While to understand the interactions between two blade rows, the relevant frequency components need to be carefully calculated.

In 1960s, Tyler, J. M., and Sofrin, T. G. theoretically derived the expressions for fluctuation modes associated with the rotor-stator interactions [74]. Based on their study, plenty of researchers worked out the exact frequency components, and studied the rotor-stator interaction behaviors in their specific rotating machinery cases [70, 72, 75, 76]. While for the rotor-rotor combination case, no theoretical analysis about blade rows interaction seems to be reported before. In the present researches, on the basis of such rotor-stator case, the prediction equations for the pressure fluctuation modes induced by the rotor-rotor interactions are derived as follows. These equations are believed to be also available to apply in other flow properties.

5.2.1 Derivation of frequency modes associated with rotor-rotor interactions

In a simple rotor-stator combination as schematically shown by Fig. 5-4 (a), with the stator number as '*F*' and the rotor number as '*R*', the interactions between a certain stator blade q and all the rotor blades would result in the periodic pressure fluctuations at any circumferential location θ as expressed by Eq. (5-8) [74].

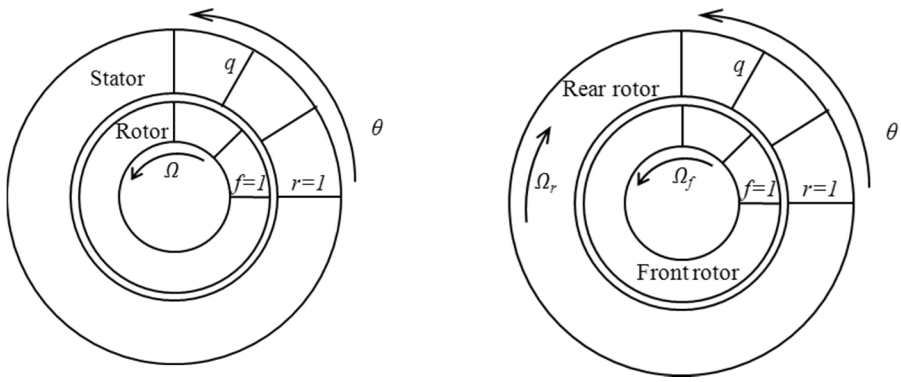

(a) Rotor-stator case (b) Rotor-rotor case

Fig. 5-4 Schematic figures accounting for the blade rows interaction

$$P_{m,n}{}^{q}(\theta,t) = a_{m,n}\cos\left[m\left(\theta - \frac{2\pi}{F}q\right) - nR\Omega(t - \frac{2\pi}{F\Omega}q)\right] \tag{5-8}$$

In this equation, m and n are the orders of the harmonic components in spatial and time domains respectively, Ω denotes the angular rotation speed of the rotor, and a for the amplitude of each mode.

Considering the influences from all the stators collectively, the pressure fluctuations at location θ could be expressed as follows,

$$P_{m,n}(\theta,t) = \sum_{q=1}^{F} P_{m,n}{}^{q}(\theta,t) = a_{m,n}\sum_{q=1}^{F}\cos\left[m\theta - nR\Omega t - (m - Rn)\frac{2\pi}{F}q\right] \tag{5-9}$$

given m, n and k as any arbitrary integers, according to the properties of trigonometric functions,

this equation could be simplified as the following form

$$P_{m,n}(\theta,t)=\begin{cases}Fa_{m,n}\cos(m\theta-nR\Omega t) & m-nR=kF\\ 0 & m-nR\neq kF\end{cases} \tag{5-10}$$

This equation physically indicates, at any peripheral location θ, only the pressure fluctuation modes with the condition of m-nR=kF could be persistent with the angular frequencies of Ω_m=$nR\Omega$, while the others all diminish to zero since the identical modes induced by the different stator blades cancel each other due to their phase differences.

In the contra-rotating rotor-rotor case, where 'F' is regarded as the front rotor blade number and 'R' as the rear rotor blade number (Fig. 5-4 (b)), setting the rotating direction of the front rotor as positive, the pressure modes associated with each rotor in its individual rotating frame could be expressed as follows.

Front rotor: $$P_{m,n}{}^{F}(\theta_F,t)=Fa_{m,n}\cos(m\theta_F-nR(-\omega_F-\omega_R)t) \tag{5-11}$$

Rear rotor: $$P_{m,k}{}^{R}(\theta_R,t)=Rb_{m,k}\cos(m\theta_R-kF(\omega_F+\omega_R)t) \tag{5-12}$$

Transferring Eqs. (5-11) and (5-12) into the stationary frame, with the relations of θ_F=θ-$\omega_F t$, and θ_R=θ+$\omega_R t$, and also given the condition of m-nR=kF, the following Eqs. (5-13) and (5-14) could be obtained,

$$P_{m,n}{}^{F}(\theta,t)=Fa_{m,n}\cos(m\theta-(kF\omega_F-nR\omega_R)t) \tag{5-13}$$

$$P_{m,k}{}^{R}(\theta,t)=Rb_{m,k}\cos(m\theta-(kF\omega_F-nR\omega_R)t) \tag{5-14}$$

As shown in Eqs. (5-13) and (5-14), for a rotating machinery with the rotor-rotor combination, at any peripheral location θ in the stationary frame, the pressure fluctuation mode m introduced by the rotor-rotor interactions appears with the angular frequencies of $kF\omega_F$-$nR\omega_R$, where m, n, k are any arbitrary integers satisfying the condition of m=nR+kF.

5.2.2 Predicted pressure modes for two rotation speed combinations

Given two rotation speed combinations of rotor pairs RR2 and RR3, and the blade number of the front and the rear rotor as 4 and 5 respectively, the rotor associated fluctuation modes which probably exist in the stationary frames are capable to be predicted. In Table 5-4, such pressure modes with low circumferential wave numbers ($|m|\leq 10$) for two speed combinations are listed, and the modes with higher m are not considered since they are believed to be with fairly weak amplitudes.

Table 5-4. Predicted fluctuation modes in two rotation speed combinations

N_f=1311 N_r=1123 (min^{-1})		$N_f = N_r$=1225 (min^{-1})	
m	Frequency	m	Frequency
-10	187.17	-10	204.17
-8	636.53	-8	653.33
-7	455.55	-7	469.58
-6	274.57	-6	285.83
-5	93.58	-5	102.08
-4	723.93	-4	735.00
-3	542.95	-3	551.25
-2	361.97	-2	367.50
-1	180.98	-1	183.75
1	630.35	1	632.92
2	449.37	2	449.17
3	268.38	3	265.42
4	87.40	4	81.67
5	717.75	5	714.58
6	536.77	6	530.83
7	355.78	7	347.08
8	174.80	8	163.33

5.3 Blade passing frequency (BPF) distribution for both rotor pairs in axial direction

As a well-known frequency component, the blade passing frequency (BPF) determined by the blade number and the rotor rotation speed is highly representative for the influences associated with any individual rotor. In Fig. 5-5, the axial distributions of the strength of the measured BPF modes for two rotor pairs RR2 and RR3 are given at the design flow rate Q=70 L/s and the off-design flow rate Q=28 L/s. In these figures, the mode of m=4 (n=0, k=1) corresponds to the BPF component of the front rotor while the mode of m=-5 (n=1, k=0) corresponds to that of the rear rotor.

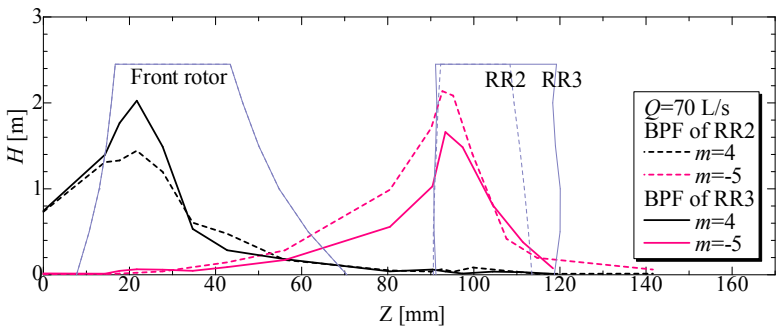

(a) At design flow rate Q=70 L/s

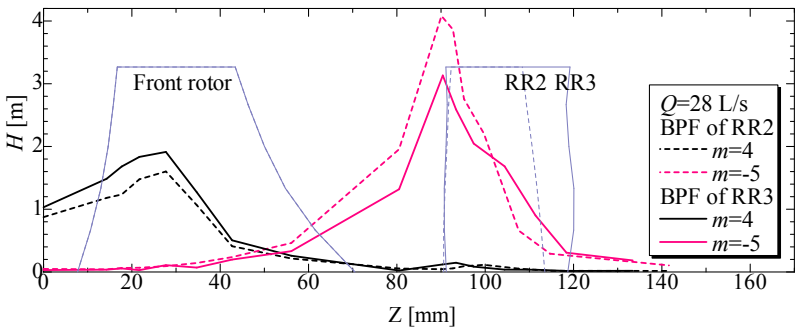

(b) At partial flow rate Q=28 L/s

Fig. 5-5 Axial distributions of the measured BPF modes for RR2 and RR3

In general, it is distinctive that the BPF mode of each rotor decays relatively slow in the upstream direction since the high blade loading basically locates at the fore part of the blade. As the previous theoretical analysis [44], the rear rotor located downstream plays a more critical role in the rotor-rotor interaction regardless of the operating flow rate, since its influences always extend deep inside the front rotor's passages while the front rotor's BPF components nearly vanish at its own trailing edge. Therefore, the RR3 type rear rotor, which has been designed with the reduced rotation speed as well as the decreased stagger angles (Table 3-7), seems to have the relieved interaction to the front rotor, since its BPF mode diminishes to the much lower level at the front rotor's trailing edge.

From the variation in the individual rotor's BPF peaks, it can also be seen the renewed work division inside the contra-rotating rotor pair RR3. Consistent with the increased blade loadings, the front rotor shows the reinforced BPF peak around its own leading edge. While for the rear rotor RR3, which offers the increased head rise at Q=70 L/s but the inferior head rise at Q=28 L/s compared to the RR2 type (Fig. 4-2), it persistently shows the well reduced BPF peak at its leading edge. Hence, one can understand that the loading situation must not be the unique reason to determine the BPF strength, and the more careful design especially the consequently reduced stagger angles must also contribute to this. Thus, the significances of the appropriate work ratio as well as the rotation speed combination in the contra-rotating rotors are once again emphasized.

5.4 Correlation analyses on pressure data obtained at various peripheral locations

5.4.1 Correlation analyses results at design condition

The pressure spectra obtained from four circumferentially located pressure taps A1~4 (rear rotor inlet section as shown in Fig. 5-1) in the RR3 rotor pair at the design flow rate are presented in Fig. 5-6.

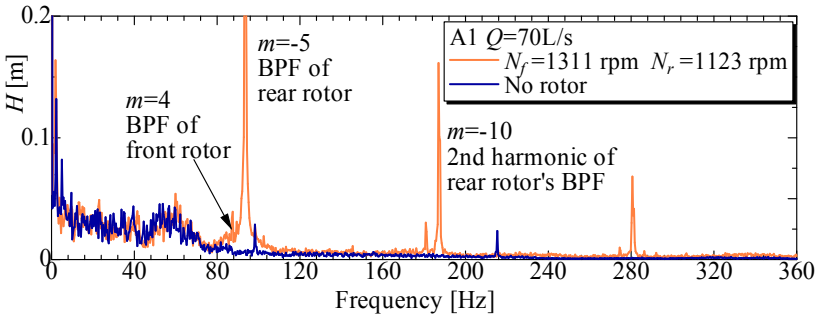

(a) A1

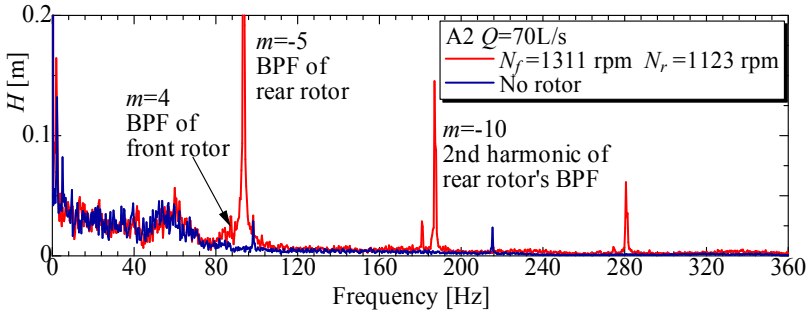

(b) A2

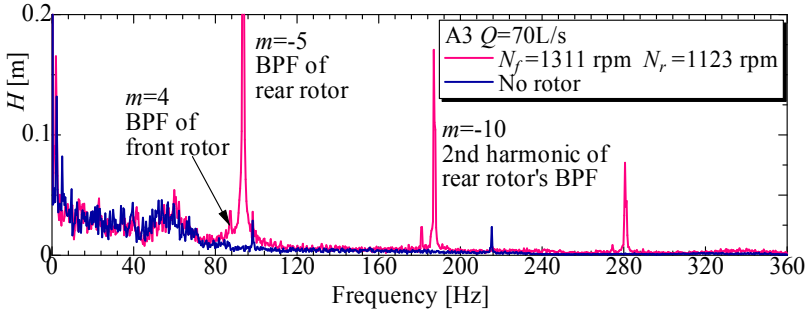

(c) A3

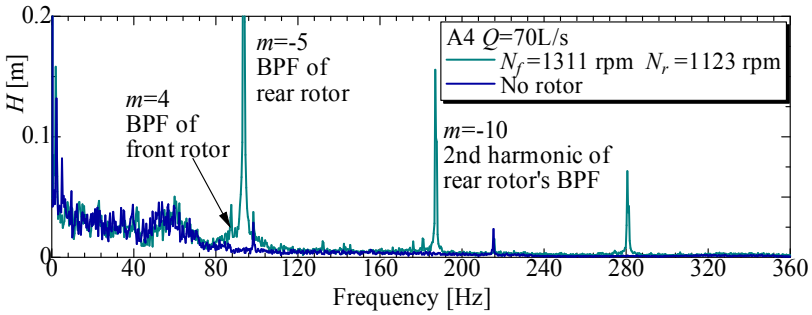

(d) A4

Fig. 5-6 Spectra of casing wall pressure obtained at the rear rotor inlet A1~4 under the design flow rate Q=70 L/s

It is clear that, at the identical axial location, the pressure frequency spectra obtained from the varied peripheral positions highly resemble with each other. These frequency spectra are generally dominated by the BPF components of two rotors, their higher harmonics, and unknown peaks with weak strengths. The intensive components with the relatively higher amplitudes in the low frequency range are believed to be the disturbances from the entire test loop system. Since with the entire testing pipe system operating in the absence of both rotors, but with the booster pump operating at the same flow rate, the fluctuation components at such low frequency range were still detected at the corresponding pressure taps as the spectrum plotted in deep blue in Fig. 5-6. At the design flow rate, such components highly resemble the low frequency modes obtained with both rotors applied. Therefore, it is confident to neglect the low frequency range ($f \leq 90$ Hz) at this flow rate and to focus on the modes described in Table 5-4 during the rotor-rotor interaction investigation.

Against the theoretically calculated pressure modes in Table 5-4, several noticeable peak components f_m (Table 5-5) in the relatively higher frequency range were found, and supposed to be associated with the individual rotor's rotation or the rotor-rotor interactions. To pertinently validate this, the mutual correlations among the identical modes f_m obtained at the different peripheral locations (A1~4) were investigated.

As introduced in Sec. 5.2.3, the cross spectrum $S_{xy}(f)$ of any two frequency series were calculated, and then their corresponding phase angles $Q_{xy}(f)$ were obtained to compare with the theoretical ones induced by such two taps' peripheral distance $m*\Delta\theta$, and moreover the spectral coherences ${Coh_{xy}}^2(f)$ were acquired. In Table 5-5, only the calculation results between A1 and A3, A3 and A4 are presented since the space limitation.

Table 5-5. Correlation analyses results for two rotation speed combinations at the design flow rate Q=70L/s

N_f=1311 N_r=1123 (min^{-1})

m	f_m	A1 and A3			A3 and A4		
		$m*\Delta\theta$	Q_{13}	Coh^2_{13}	$m*\Delta\theta$	Q_{34}	Coh^2_{34}
-10	186.9	-140	-142.2	1.00	-180	-169.2	1.00
-6	274.5	60	70.4	0.82	-180	-166.3	0.91
-5	93.7	110	109.6	1.00	-90	-86.2	1.00
-2	362.0	-100	-100.1	0.86	180	177.7	0.74
-1	181.2	-50	-40.7	0.96	-90	-81.8	0.95
2	449.5	100	13.3	0.60	180	34.4	0.86
3	268.3	-210	-153.3	0.50	-90	-75.2	0.37
4	87.5	-160	-171.3	0.81	0	-9.2	0.95
6	536.3	300	71.2	0.82	180	26.1	0.57
7	335.1	-10	-47.5	0.57	270	39.0	0.50

N_f=N_r=1225 (min^{-1})

m	f_m	A1 and A3			A3 and A4		
		$m*\Delta\theta$	Q_{13}	Coh^2_{13}	$m*\Delta\theta$	Q_{34}	Coh^2_{34}
-10	204.2	-140	-140.3	1.00	-180	-169.1	1.00
-6	285.6	60	56.1	0.88	180	178.5	0.56
-5	102.1	110	109.9	1.00	-90	-87.4	1.00
-2	367.4	-100	-85.3	0.91	180	173.1	0.93
-1	183.5	-50	-31.3	0.97	-90	-92.8	0.97
2	448.7	100	61.9	0.57	180	132.8	0.67
3	265.3	150	165.8	0.82	-90	-80.0	0.79
4	81.8	200	177.0	0.92	0	-30.9	0.95
6	530.9	300	74.5	0.76	180	-11.8	0.19
7	348.6	-10	-27.7	0.76	-90	-132.2	0.55

It can be easily seen from Table 5-5 and Fig. 5-6 that with *m* or/and frequency increasing, the corresponding modes descend to be rather weak and almost in the same level with the noise disturbances from the entire test system, and in turn the correlations between those from any two data series become too weak to be recognized.

The modes synchronous to the rear rotor rotation *m*=-5, -10, as its BPF component and 2nd order harmonic, appear with the highest amplitudes in the whole frequency range. For those components, the best consistence between the measured cross spectrum phases $Q_{xy}(f)$ and the theoretical ones were found as shown in Table 5-5, and the remarkably high correlations between any two data series were obtained with the spectral coherences ${Coh_{xy}}^2(f)$≈1. Since the mode *m*=4 synchronous to the front rotor's rotation decays rather rapidly in the downstream direction as mentioned in Fig. 5-5, it shows the cross spectrum phase more deviated from the theoretical one and slightly reduced spectral coherences compared with the stronger mode *m*=-5.

The modes with the increased *m* value or frequency, whose amplitudes are reduced to the much lower level, become quite vulnerable to the errors from either the flow instabilities or the test equipment system itself. As shown in Fig. 5-7, the mode *m*=-2 with the predicted frequency of 361.97 Hz is hardly able to be recognized merely by its amplitude.

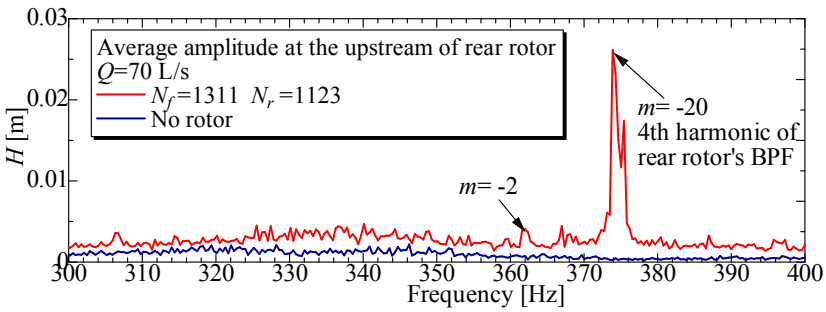

Fig. 5-7 Pressure spectrum in higher frequency range

The weakened amplitude implies the increasing relative standard deviation among the four

pressure spectra and in turn the well decreased spectral coherences. Figure 5-8 presents the averaged amplitudes and spectral coherences for the modes non-synchronous to any BPF components at the design flow rate Q=70 L/s. The data obtained from the RR3 pair with the both front and rear rotors operating at equivalent speed (N_f=N_r=1225 min^{-1}) is also plotted in this figure for the comparison. It could be seen that the spectral coherences $Coh_{xy}{}^2(f)$ generally vary in the same trend with amplitudes. Hence, the correlations are merely able to be identified confidentially for the modes with the absolute value of m below 7 or the frequency below 450 Hz.

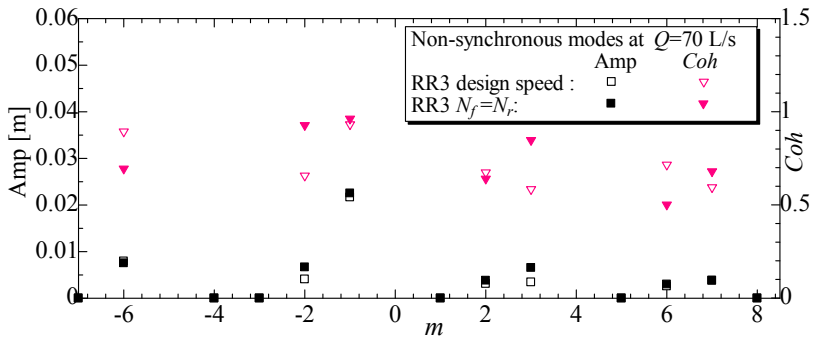

Fig. 5-8 Amplitudes and spectral coherences of the pressure modes non-synchronous to BPF components

In addition from Fig. 5-8, it can be found that the new rotation speed combination (N_f=1311 min^{-1} N_r=1123 min^{-1}) offers slightly but still noticeably lower amplitudes at most of the modes non-synchronous to the BPF components, which demonstrates the weakened rotor-rotor interactions in the rotor pair of new rotation speed combination.

5.4.2 Correlation analyses results at partial flow rate

At the critical partial flow rate Q=28L/s, it was again confirmed that the pressure spectra from the measuring locations A1~4 are quite similar, so that only the averaged results are given in Fig. 5-9. From this figure, it could be found that the amplitudes get sharply raised in the

whole frequency range in contrast with those at the design flow rate (Fig. 5-6).

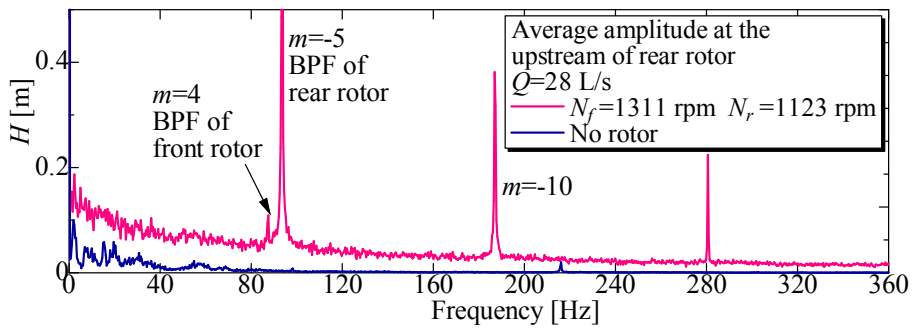

(a) Frequency range of 0~360 Hz

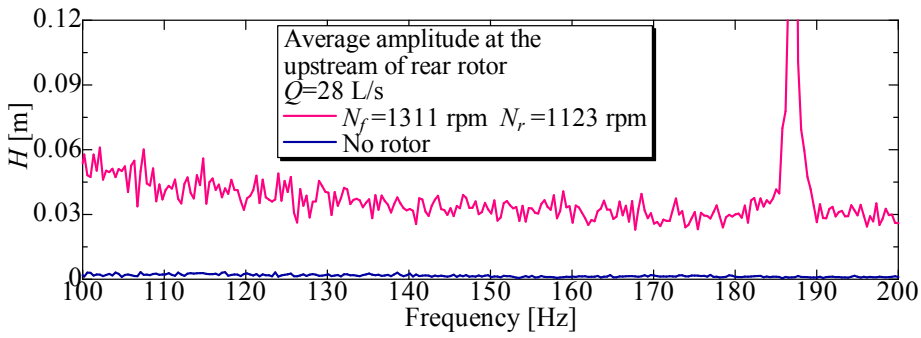

(b) Frequency range of 100~200 Hz

Fig. 5-9 Average pressure spectra at the rear rotor's inlet at Q=28L/s

From the secondary flow analyses in the previous chapter, operating at the flow rate fairly lower from the design condition, the both front and rear rotors present sharply increased head rises, and the flow patterns especially at the middle position of two blade rows consequently develop to be rather complicated with various back flows and unstable vortices. Such flow instabilities are supposed to introduce numerous disturbances as well as fluctuation modes as shown in Fig. 5-9. The modes associated with the rotor-rotor interactions are rather difficult to be recognized in almost the whole frequency range.

On the other hand, at the downstream location of the rear rotor where the flow patterns are

less complicated, the rotor-rotor interaction associated modes remain in a recognizable level. As shown in Fig. 5-10, the noises and disturbances appear with much lower strengths, so that a few of representative modes are capable to be identified.

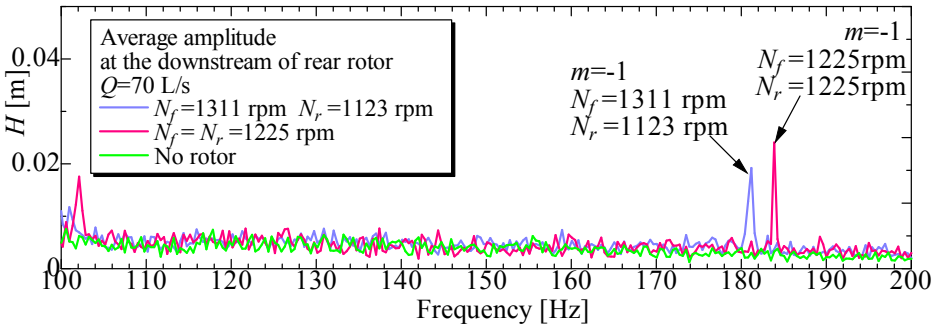

(a) Q=70L/s

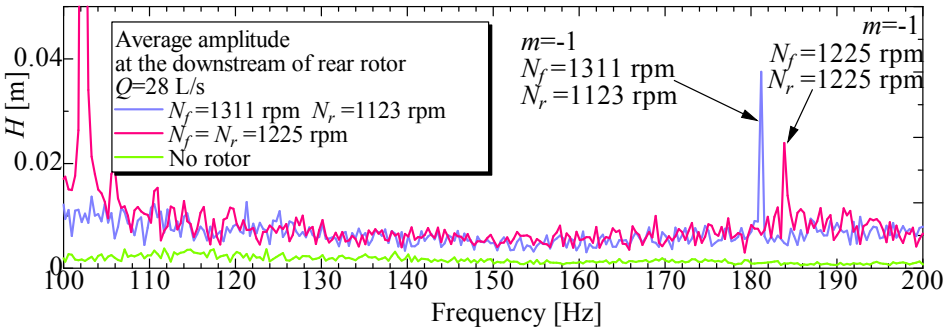

(b) Q=28L/s

Fig. 5-10 Average pressure spectra downstream of the rear rotor

In Table 5-6, such modes which could be recognized downstream of the rear rotor at the design and partial flow rates are presented.

Compared with the upstream location of the rear rotor, the downstream location can merely offer fewer modes with fairly weak amplitudes, due to being far apart from the rotor gap region where the two rotors' pressure fields mutually interfere. Generally, except for the modes m=-5 and -10 synchronous to the rear rotor's rotation, and the non-synchronous ones m=-1 and -2 with low frequencies, other modes all diminish to be unrecognizable. Nevertheless, for the case

of the partial flow rate Q=28L/s, the downstream location as shown in Fig. 5-10 (b) is still informative since the pressure spectra at the rear rotor inlet section are dominated by various disturbances resulted from the complex blade-to-blade flow structure.

Table 5-6. Correlation analyses results for two rotation speed combinations at the design and partial flow rate (obtained downstream rear rotor)

N_f=1311 N_r=1123 (min^{-1})							
m	f_m	Q = 70L/s			Q = 28L/s		
		$m*\Delta\theta$	Q_{56}	Amp	$m*\Delta\theta$	Q_{56}	Amp
-10	187.3	-160	-	-	160	109.09	0.015
-5	93.7	-100	-83.18	0.024	-100	-82.41	0.116
-2	362	-40	-18.90	0.003	-40	-35.22	0.005
-1	181.2	-20	-18.56	0.019	-20	-28.00	0.039
N_f=N_r=1225 (min^{-1})							
m	f_m	Q = 70L/s			Q = 28L/s		
		$m*\Delta\theta$	Q_{56}	Amp	$m*\Delta\theta$	Q_{56}	Amp
-10	204.6	160	117.48	0.002	160	165.17	0.014
-5	102.1	-100	-66.25	0.017	-100	-98.68	0.123
-2	367.8	-40	-24.56	0.003	-40	-31.23	0.003
-1	183.9	-20	-19.90	0.024	-20	-23.77	0.027

Overall, it can be learned from the respective amplitudes of the modes m=-1 and -2 obtained at the design flow rate Q=70L/s, the rotor-rotor interactions in the equal rotation speed combination appear to be slightly but still noticeably stronger. This further implies the effectiveness of the different-speed design methodology under the design condition. However, in contrast, at the partial flow rate Q=28L/s, the corresponding modes obtained in the different

rotation speed combination appear with relatively higher strengths as plotted in Fig. 5-10 (b). According to the performance studies in the previous chapter, with the flow rate reduced to a rather low level, the RR3 rear rotor shows the very high loading situation, and in turn suffers from fairly severe secondary flows inside its flow passage, which probably reinforce the interactions between two blade rows.

5.5 Blade-to-blade pressure distribution in both rotor pairs

Based on the measurement method, the pressure field measurement (PFEM) introduced in Sec. 5.1.3, the blade-to-blade pressure contours under various rotor-rotor relative positions were obtained for both RR2 and RR3 rotor pairs. To better understand the two rotor pairs' pressure field properties, all the pressure data was converted into the hydraulic head H [m] relative to the static pressure measured at the pump inlet section, and all contours were drawn with the reference line (the magenta chain line in Fig. 5-3) set as Z-axis (longitude 0º) at the left boundary of the figure.

5.5.1 Pressure distributions in both rotor pairs at design condition

Figure 5-11 represents the blade-to-blade distributions of casing wall static head H_s for the two rotor pairs RR2 and RR3, under the relative position of $\Delta\theta$=50° at their respective design conditions.

As described in the previous sections, the head division in the rotor pair RR3 was renewed as H_f=2.15m and H_r=1.85m to reduce the potential impacts from the rear rotor to the front rotor. Consistent with the design expectation, from the contour levels marked by color and number in Fig. 5-11 (a), it can be easily seen that, the front rotor shows the reinforced high pressure regions while the rear rotor presents the weakened low pressure regions in the RR3 rotor pair. As one of the essential results of the reduced rotation speed design, the lower stagger angles of

the RR3 rear rotor do not appear to obviously contribute in reducing the interferences between two blade rows' pressure regions. This is perhaps due to the head rises of the both front and rear rotors are still in a relatively low level at the design condition.

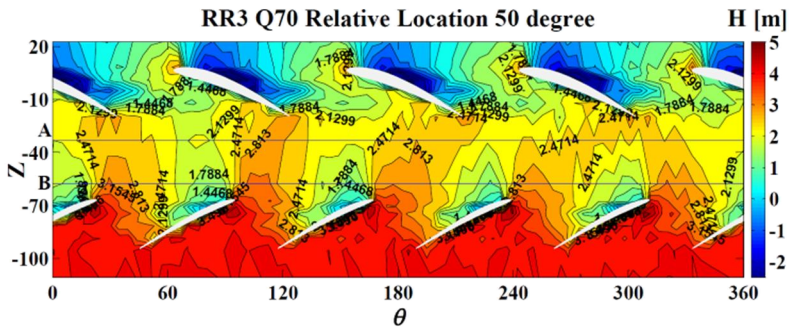

(a) Pressure distribution of RR3 pair at $\Delta\theta$=50º

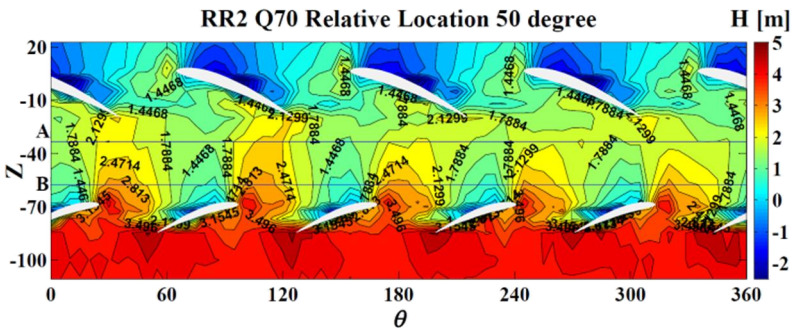

(b) Pressure distribution of RR2 pair at $\Delta\theta$=50º

Fig. 5-11 Pressure distribution of two rotor pairs at certain relative angular position $\Delta\theta$=50º under design condition

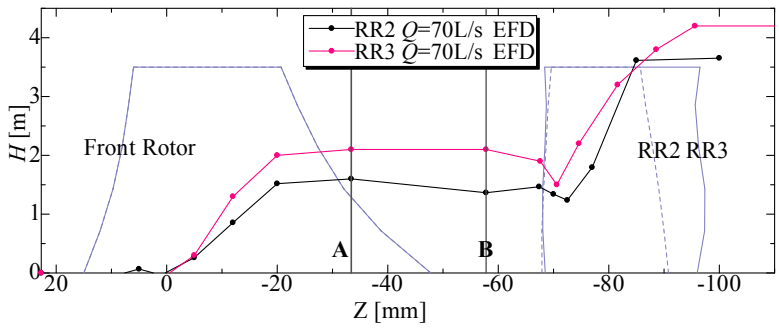

Fig. 5-12 Axial distribution of averaged casing wall pressure for two rotor pairs under design condition

Since the high pressure regions offered by the front rotor in two rotor pairs remain in quite different levels, their blade-to-blade pressure field properties cannot be well understood just by comparing Fig. 5-11 (a) and (b). The axial distributions of the averaged casing wall static head are given in Fig. 5-12. Between the sections 'A' and 'B' (marked by dark blue lines in Fig. 5-11), the circumferentially averaged casing wall static head was found to be decreasing in the rotor-rotor gap region of the RR2 rotor pair, while no obvious pressure change was observed for the RR3 rotor pair. Considering this pressure decrease as the influences from the low pressure regions of the downstream rear rotor, the RR3 pair is believed to have weakened blade rows interactions at the design flow rate.

As mentioned in Chapter 3, under the design condition, the tip sections of the RR2 blades were found with negative incidence angles and stagnation points located at the suction surfaces, which was known as fairly unfavorable for the cavitation performances [5]. From Fig. 5-11 (b), although the stagnation points of the RR2 profiles are insufficiently clear to be recognized, such deficiencies could be identified by the aft-loading situation of those profiles.

With the consideration of the improved cavitation performances, the positive incidence angle was emphasized in the design of RR3's profiles. As shown in Fig. 5-11 (a), the RR3 profiles appear with the lowest and the highest pressure regions oppositely located at the suction and the pressure surfaces near the leading edge, implying that the RR3 rear rotor meets such a design expectation of loading at the fore part of the profile.

5.5.2 Pressure distributions in both rotor pairs at partial flow rate

As shown in Fig. 5-13, the differences in pressure field of two rotor pairs grow more significant at the off design flow rate of Q=28L/s. From the respective performance curves (Fig. 4-2), it could be seen that, at this flow rate, the head rise of the rear rotor goes up to a fairly

higher level compared with that of the front rotor in the RR2 combination, while the head rises offered by the two rotors are still comparable in the RR3 pair.

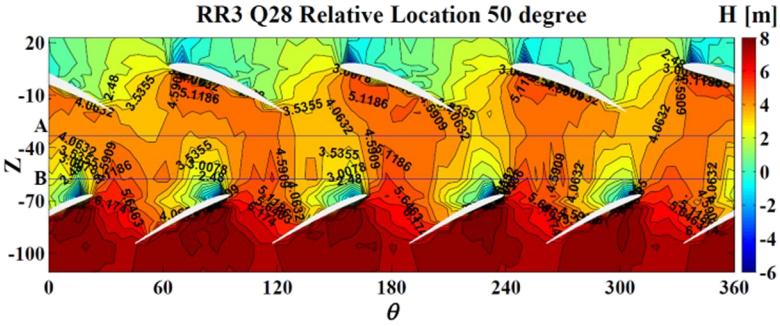

(a) Pressure distribution of RR3 pair at $\Delta\theta$=50º

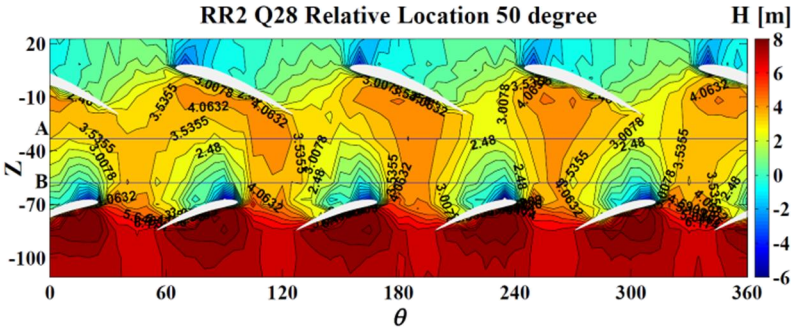

(b) Pressure distribution of RR2 pair at $\Delta\theta$=50º

Fig. 5-13 Pressure distribution of two rotor pairs at certain relative angular position $\Delta\theta$=50º at Q=28L/s

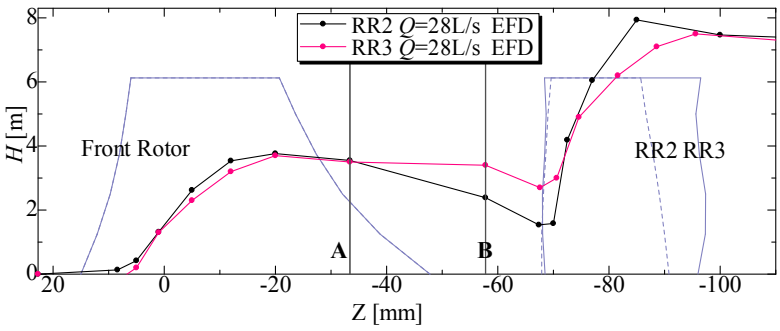

Fig. 5-14 Axial distribution of averaged casing wall pressure for two rotor pairs at partial flow rate Q=28L/s

Consistent with the performance properties described above, in the RR2 rotor pair given by Fig. 5-13 (b), the front rotor shows the weakened and vulnerable high pressure fields while the rear rotor presents the rather strong low pressure fields. In addition, with its high stagger angle the rear rotor RR2's low pressure fields appear to be straightly towards upstream, resulting in the significant impacts on the front rotor's high pressure fields. Hence, the RR2 pair's pressure field between the two blade rows is majorly dominated by the low pressure regions of the rear rotor, and the front rotor's high pressure regions are limited in the narrow ranges very close to its pressure surfaces during the rear rotor blade passing. Consequently in the RR2 rotor pair, at such low flow rate, the front rotor suffers from the significantly fluctuated blade loading, and the averaged static pressure was believed to be remarkably decreasing from the front rotor's trailing edge to the rear rotor's leading edge. This remarkable static pressure reduction was then confirmed in the axial distributions of peripherally averaged casing wall static head as shown in Fig. 5-14.

In contrast, according to the performance curves, with the redesigned rotation speed combination in the RR3 pair, the front rotor persistently offered superior head rise for almost the whole flow range. Therefore as shown in Fig. 5-13 (a), the pressure field between the two blade rows in the RR3 rotor pair is apparently dominated by the high pressure regions of the front rotor, and the rear rotor shows the remarkably shrunk low pressure regions in contrast with the RR2 type rear rotor. Furthermore, as one of the essential results from the reduced rotation speed design, the smaller stagger angles of RR3 leads to the low pressure regions more towards its own blade passages, which pertinently depresses the interactions between the pressure fields of the two blade rows. In Fig. 5-14, the circumferentially averaged static head in the RR3 rotor pair shows a slight decreasing tendency from the section 'A' to 'B' while a significant pressure reduction is found in the corresponding locations of the RR2 rotor pair.

Generally, with various benefits from the reduced rotation speed design, the pressure field between the two blade rows in the RR3 rotor pair suffers from less pressure variation and be capable to remain on a relatively high pressure level regardless of the operating flow rate.

5.6 Extractions of blade loading curves

Ordinarily, the actual pressure distribution at the exact blade tip profile usually deviates from that evaluated without the consideration of the tip leakage flow. Numerous researchers have confirmed that the tip leakage flow remarkably accelerates around the corner between the pressure side and the tip surface where it enters into the tip gap [67, 68], and this acceleration results in a significant static pressure reduction at the corresponding position. In Fig. 5-15, the distributions for the static pressure and relative velocity along several streamlines through the tip gap of RR3 rear rotor obtained by the unsteady numerical simulations are presented. As described by other researchers, the fluid shows the remarkable velocity increase and pressure reduction when it turns around the corner between the pressure side and the tip surface due to the sharp curvature there.

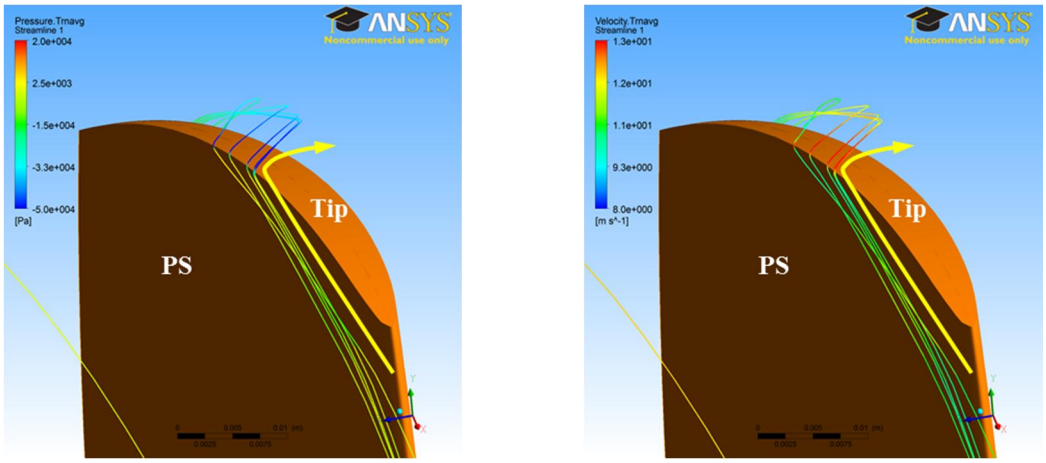

(a) Static pressure distribution along streamlines

(b) Relative velocity distribution along streamlines

Fig. 5-15 Distributions of pressure and velocity along several streamlines through tip gap

Such pressure deficiency is also influential to the static pressure distribution on the casing wall. As shown in Fig. 5-16, the obvious pressure reduction starting from the pressure surface side of the rotor blade profile could be observed as region 'D'. Thus, by the measured casing wall static pressure contour map, the loading curves of blade tip profile with and without the consideration of tip leakage flow were supposed to be obtained by the different estimation methods.

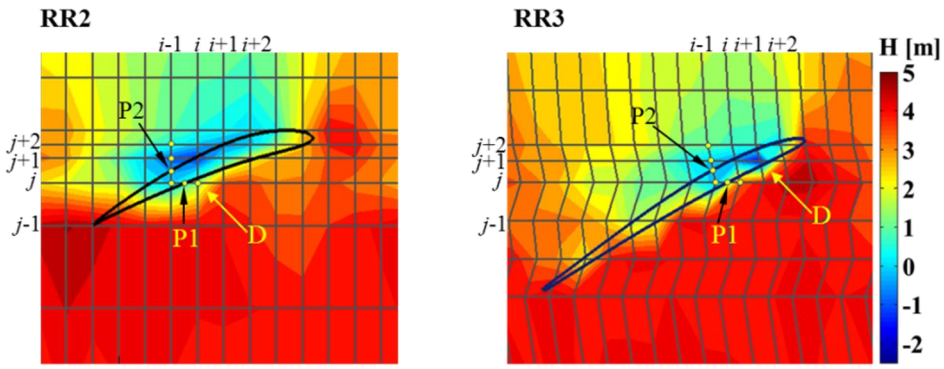

(a) RR2 measuring mesh (b) RR3 measuring mesh

Fig. 5-16 Pressure measuring meshes for two rear rotors

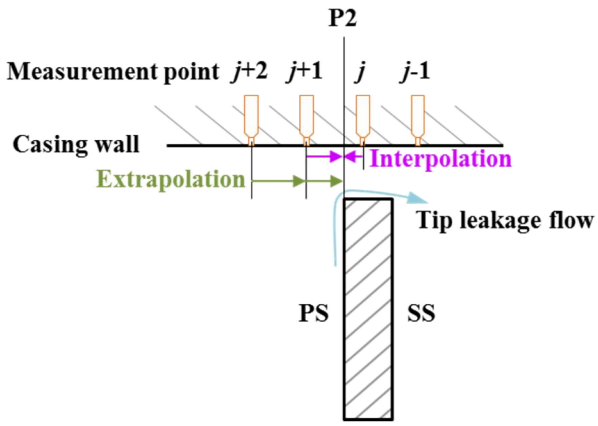

Fig. 5-17 Two methods to extract the blade loading curves

In the present studies, without the consideration of tip leakage flow, the static pressures at the points on the blade tip profile were estimated by the extrapolation method to establish the loading curves of blade tip section. The inherent loading properties of the newly designed blade profile could be better understood with the loading curves experimentally obtained in this way. And moreover, to evaluate the blade tip section's loading situation with the influences from the tip leakage flow, the interpolation method was applied. As schematically shown in Fig. 5-17, in the extrapolation method, the pressure at the certain point 'P2' on blade tip profile was derived by two mesh nodes P(j+2) and P(j+1) at its single side (passage side). While in the interpolation method, two mesh nodes P(j+1) and P(j) at two sides of this point were adopted. These two methods will be further elaborated combining with the measurement meshes in Fig. 5-16.

As shown in Fig.5-16, for the interpolation method, the static pressure at a certain location 'P1' intersected by the blade profile and the measuring mesh is obtained from the linear interpolation using two adjacent nodes P(j, i-1) and P(j, i), which are respectively located at its two sides. The pressure deficiency induced by the tip leakage flow could be therefore reflected. Due to the large stagger angle and moreover the rather low thickness of the blade tip profile, the extrapolation is more rational to be carried out using the nodes located in the axial direction. Hence besides by the interpolation method, the pressure at the location 'P2' could be obtained by the linear extrapolation using the two nodes P(j+2, i-1) and P(j+1, i-1) which are both located at the flow passage side. The inherent loading properties of the blade profile could be estimated in the extrapolation method since the adopted mesh nodes are both located in the main passage flow territory.

Figure 5-18 shows the pressure coefficient C_p distributions along the chord (x/l) for the blade tip profiles of two rear rotors at the design flow rate. They were evaluated by the above extrapolation and interpolation methods, and directly obtained at the near tip section ($r = 0.98r_c$)

and the casing wall by the unsteady numerical simulations.

The pressure coefficient C_p is herein defined as

$$C_p(x/l) = \frac{p(x/l) - p_{in}}{\rho {U_t}^2/2}$$

where p_{in} is the averaged static pressure measured at the rear rotor inlet section, U_t is the peripheral velocity of the blade tip.

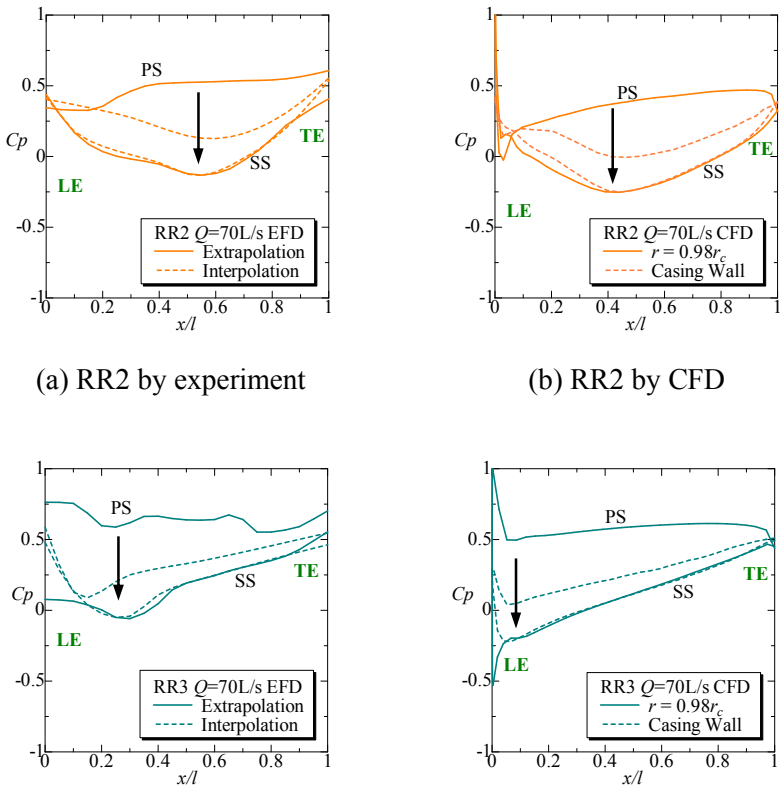

(a) RR2 by experiment (b) RR2 by CFD

(c) RR3 by experiment (d) RR3 by CFD

Fig. 5-18 Loading curves of two type rear rotors obtained by experiment and CFD approaches

Since the measurement meshes were relatively coarse in the axial direction and the blade tip profiles especially for the RR3 type were designed with rather low thickness, the loading curves predicted by the extrapolation approaches appeared to be highly fluctuated, and be not able to recognize the critical pressure gradient at the leading edge. Nevertheless, the pressure variation

tendencies on two blade sides offered by the extrapolation method and obtained at the near tip section ($r = 0.98r_c$) by the numerical simulations are quite similar, since they both avoided the influences from the tip leakage flow. With the consideration of the tip leakage flow, the loading curves obtained by the interpolation method and acquired at the casing wall by the numerical simulations were found to well coincide with each other.

Overall, the inherent loading properties of the rotor blade tip profile were believed to be generally captured by the extraction from the measured blade-to-blade pressure distributions using the extrapolation method. From both experimental and numerical approaches, the pressure deficiencies induced by the tip leakage flow were well reproduced, and the most significant pressure reduction was found at the location with maximum loading as marked by the black arrows.

As observed on the pressure contours in the previous sections, designed with the positive incidence angle the newly designed RR3 rear rotor presents a fore-loading situation, while RR2 type shows an aft-loading status which was known as fairly unfavorable for the cavitation performances. And for the RR2 rear rotor, both the experimental and the numerical results show that the pressure on SS exceeds that on PS in a narrow region around the leading edge as shown in Fig. 5-18 (a) and (b), pertinently indicating the stagnation point located on the suction surface. Hence as predicted during the cavitation studies by means of $NPSH_r$ (Sec. 3.3.3), the pressure surface is likely to suffer cavitation in such region in the case that the ambient pressure reduces to a rather low level.

The RR3 rear rotor designed with the attack angle α around 8° at the tip shows extremely high loading at the leading edge according to the CFD results (Fig. 5-18 (d)), as the loading curves obtained from the similar airfoils under the attack angle of such large value [77, 78]. Ascribing the loading curve fluctuation to the errors induced by extrapolation, it is believed that

the loading curves of the RR3's tip profile highly resemble those obtained by the CFD, and the pressure on the RR3 blade's suction surface is supposed to also increase monotonously along the chord. Therefore, although the relatively lower pressure at its leading edge is observed (on suction surface as Fig. 5-18 (d)), which implies possibly earlier cavitation inception in contrast with the RR2 blades under an equal ambient pressure, the RR3 rear rotor is still believed to be superior in cavitation performances since the cavitation can be well limited on the suction surface.

5.7 Summary

In this chapter, the investigations of the rotor-rotor interactions in two types of contra-rotating rotor pairs were discussed, and the associated various pressure measurement approaches and the data processing methods were also introduced.

With the continuous casing wall static pressure measurements and the subsequent frequency spectrum analyses, the blade passing frequency (BPF) components of the individual rotor and the pressure modes associated with both rotors' rotation were recognized. Considering from the strengths of the corresponding BPF modes, the rear rotor designed with the reduced rotation speed as well as the decreased stagger angles presented relatively weaker impacts on the front rotor both at the design and off design conditions. At the design flow rate, the pressure modes associated with the rotor-rotor interactions were also found to be relieved in the contra-rotating rotor pairs with the different-speed design method applied.

With the pressure measurement concept taking account of the revolutions of both front and rear rotors simultaneously, the casing wall pressure data sampled in time domain was transferred into space domain successfully, and the ensemble averaged blade-to-blade pressure distributions under different operation conditions were obtained. Designed with the renewed work division

between the front and rear rotors, the new rotor pair RR3 showed the enhanced high pressure regions of the front rotor and the weakened low pressure regions of the rear rotor at various operation conditions. As one of the essential results of the reduced rotation speed design, the lower stagger angle of the RR3 rear rotor resulted in the low pressure regions more towards its own blade passages especially at the partial flow rate. All of these indicated the relieved potential interactions between two blade rows in the contra-rotating rotors with different-speed design method applied.

Moreover, as one of the important design expectations, the superior cavitation performances were confirmed for the newly designed RR3 rear rotor, of which the favorable blade fore-loading situation could be observed from the pressure distribution contours and the blade loading curves extracted from the casing wall pressure measurement results.

6 Conclusions

Based on all the findings about the prototype contra-rotating axial flow pump with the equal-speed rotors, this thesis primarily discussed the possibilities to improve the hydraulic performances of the contra-rotating axial flow pump by rearranging the work division as well as the rotation speed combination in the contra-rotating rotor pair.

As a determination method for the rotor-rotor speed combination in the contra-rotating axial flow pump, the different-speed design method was proposed in expectation of the improved cavitation performances as well as the relieved rotor-rotor interactions, and to better satisfy the pump design specifications. Combining with several other design considerations (optimized inflow distribution model, positive incidence angle, secondary flow suppression, etc.), a new rear rotor was designed to work with the former front rotor (employed in the equal-speed prototype rotor pair RR2) at the renewed rotation speed combination. And the investigations on the relevant performances of the new contra-rotating rotor pair were subsequently carried out, which could be majorly concluded as follows:

1) Based on the consideration of cavitation performance improvements, the different-speed design method resulted in the reduced rotation speed and therefore the reduced stagger angle for the rear rotor, which was also considered to be beneficial to weaken the rotor-rotor interactions. Designed with the positive incidence angle and the variable maximum camber location, the new rear rotor presented the stagger angles smaller in the hub region but larger in the tip region, which was confirmed to be beneficial in terms of the work capacity (high hydraulic head rise) and moreover the cavitation performances by the unsteady CFD simulations at the design flow rate.

2) Working at the redesigned rotation speed combination, the contra-rotating rotor pair RR3, which consisted of the front rotor applied in the prototype contra-rotating axial flow pump and the newly designed rear rotor, was then confirmed to highly satisfy the design specification (H_d=4.0 m) with a relatively superior efficiency by both the experimental and simulation approaches. But a more pronounced positive slope was observed on its head curve in the rather low flow rate range, which was believed to be ascribed to the newly designed rear rotor since the similar head deficiency was also found on its individual head curve.

3) The different-speed design method also resulted in the work division between the new contra-rotating rotors quite different from that between the equal-speed contra-rotating rotors. The front rotor persistently offered the higher head rise over the rear rotor for almost the whole flow range in the RR3 pair, while in the RR2 pair its head rise was exceeded by that of the rear rotor in the full partial flow range.

4) From the internal flow structure investigations by the 5-hole probe measurements, the rear rotor was confirmed to be effective to suppress front rotor's hub back flow, which was typical and almost inevitable at the rotor outlet of axial flow pumps under rather low flow rates, and the reason for the RR3's inferior hydraulic performances in the rather low flow rate range was believed to lie in its outflow condition.

5) With the multi-color oil-film method adopted to visualize the limiting streamlines in the rotors' boundary layers, the existence of significant secondary flow structures was confirmed in the rear rotors at the low flow rates. They were majorly attributed to the remarkable blade loading as well as the overwhelming pressure gradient inside the flow passage, and then resulted in the severe passage blockage and the deterioration of pump performances. When the pump discharge was reduced to a rather low level, the local flow rate near the tip region was sharply increased due to the serious blockage in the lower part of the flow passage, inducing the

decreased blade loading at the corresponding location. The tip leakage vortex consequently got back into the passage and posed another considerable passage blockage, resulting in the more rapid pump performance deterioration as well as the remarkable positive slope on the head curve.

6) With the continuous casing wall static pressure measurements and the subsequent frequency spectrum analyses, the blade passing frequency (BPF) components of the individual rotors and the pressure modes associated with both rotors' rotations were recognized. Considering from the strengths of the corresponding BPF modes, the rear rotor designed with the reduced rotation speed as well as the decreased stagger angles presented relatively weaker impacts on the front rotor both at the design and off design conditions. At the design flow rate, the pressure modes associated with the rotor-rotor interactions were also found to be relieved in the contra-rotating rotor pairs with the different-speed design method applied.

7) By the pressure measurement concept taking account of the revolutions of both front and rear rotors simultaneously, the casing wall pressure data sampled in time domain was transferred into space domain successfully, and the ensemble averaged blade-to-blade pressure distributions under different operation conditions were obtained. Designed with the renewed work division between the front and rear rotors, the new rotor pair RR3 showed the enhanced high pressure regions of the front rotor and the weakened low pressure regions of the rear rotor at various operation conditions. As one of the essential results of the reduced rotation speed design, the lower stagger angle of the RR3 rear rotor resulted in the low pressure regions more towards its own blade passages especially at the partial flow rate. All of these indicated the relieved potential interactions between two blade rows in the contra-rotating rotors with different-speed design method applied.

8) As one of the important design expectations, the superior cavitation performances was

identified for the newly designed RR3 rear rotor, and the favorable blade fore-loading situation could be observed from the blade-to-blade pressure distribution contours and the blade loading curves extracted from the casing wall pressure measurement results.

In general, with the rotation speed combination determined based on the cavitation performance improvement for the rear rotor, the contra-rotating axial flow pump with different-speed rotors presented the more reasonable work division between front and rear rotors in the whole flow rate range, which is highly beneficial to optimize the blade-to-blade pressure field distributions and suppress the blade rows interactions.

Nevertheless, the positive incidence angle which was known to be favorable to the cavitation performances, also resulted in the rather large attack angle for the newly designed rear rotor, which was believed to be responsible for the rear rotor's significant secondary flow structures in the rather low flow rate range. But as another highlight of the contra-rotating axial flow pump, the individual rotational speed control of each rotor was believed to be effective to optimize the flow velocity distributions, relieve the secondary flow structures and consequently improve the pump performances at the off design condition. This remains as one of the essential research topics for the contra-rotating axial flow pumps.

In addition, due to the significant secondary flow structures and consequent losses in the rather low flow rate range, the loading distributions along blade span would be emphasized in the design of the next generation rear rotor. To relieve the thickening of the boundary layer which developed on the blade suction surface as well as on the rotor hub, as one of the essential decisive parameters to the loading situation, the design incidence angle might also be determined to be variable along the blade span for the better compromise between the cavitation performance improvement and the secondary flow suppression. This remains as another important topic for the design of the contra-rotating axial flow pumps.

Acknowledgement

I have to say it is a long and tough journey to finish a doctor thesis, especially for me who is not so well grounded in the knowledge related to the present research topics. It seems to have been done in two months, but I have never ceased to prepare for it in my last three years. I used to be tied, frustrated, depressed and even burst into tears, but eventually I am so glad to get through all of these. In this memorable experience, there are so many people generously supporting me all the time, and I cannot speak too highly of the unstinting help I received from them.

Firstly, I want to express my gratitude to Professor Akinori Furukawa, who offered me such precious opportunity to study in this outstanding university and encouraged me to advance in my research career. I cannot forget my first presentation as a PhD. student of Kyushu University in 26th IAHR, where Professor Furukawa helped me to open my eyes and understand further about life. And I am deeply grateful of all the help and supports from my present supervisor Professor Satoshi Watanabe, who inspired me with his research enthusiasm and hardworking every day. He always carefully gives me generous guidance and suggestions about my research, and shows great patience and tolerance to my carelessness and mistakes. As a good time manager, he takes care of our schedules all the time, and prompted me to finish all my papers making my graduation possible. And I also want to express my gratitude to the co-examiner of this thesis Professor Masato Furukawa, the suggestions and comments from him are rather valuable and instructive for me.

I also want to say thanks to all the members of our contra-rotating axial flow pump group, Mr. Simpei Momosaki, Mr. Toshiki Imanishi, Mr. Hiroaki Yoshimura, Mr. Hironori Honda, Mr. Tomoki Tsuneda and other seniors, whose hardworking promoted this research topic

continuously advancing. And I would like to express sincere gratitude to Mr. Kusuo Okuma on behalf of our research group. His genuine and continuous support made our all experimental findings possible. I also owe my sincere gratitude to Professor Shinichi Tsuda and all the members in our Flow Control Systems Laboratory. They are all my good friends in Japan, who are always so nice to me and give me a hand anytime when I needed.

Moreover, I feel deeply indebted to my family far in China. My parents are always fully supportive to my every decision and navigate my life with their excellent personalities, and my younger sister takes care of everything at our home during my oversea study. And my thanks also would go to Mr. Brown and every friend of mine, all the warm from you makes me stronger and grown up.

I cannot address everyone I would like to express gratitude to in this paper, but every tiny thing we went through together would become an important part of my life, and would be remembered by me forever.

Cao Linlin

2014-07-09

References

[1] Logan Jr, E. (1993). Turbomachinery: Basic Theory and Applications. CRC Press.

[2] Turton, R. K. (1995). Principles of Turbomachinery. Cambridge University Press.

[3] Gorla, R. S. and Khan, A. A. (2003). Turbomachinery: Design and Theory. CRC Press.

[4] Dixon, S. L. (2005). Fluid Mechanics and Thermodynamics of Turbomachinery. Butterworth -Heinemann.

[5] Brennen, C. E. (2011). Hydrodynamics of Pumps. Cambridge University Press.

[6] Toetz, D. W. (1977). Effects of Lake Mixing with an Axial Flow Pump on Water Chemistry and Phytoplankton. Hydrobiologia, 55(2), pp. 129-138.

[7] Lawson, R. and Anderson, M. A. (2007). Stratification and Mixing in Lake Elsinore, California: an Assessment of Axial Flow Pumps for Improving Water Quality in a Shallow Eutrophic Lake. Water Research, 41(19), pp. 4457-4467.

[8] Li, M. X. (2003). Research on the Structure Design of Large Pump for the South to North Water Transfer Project. Drainage and Irrigation Machinery, 21(3), pp. 1-5.

[9] Liu, C. (2003). Hydraulic Performance Assess Target Research of Low-Head Pump Equipment in South-North Water Transfer Project. Drainage and Irrigation Machinery, 21(6), pp. 2-5.

[10] Gao, H., Lin, W. L. and Ye, F. M. (2005). CFD Investigation of Global Performance and Three Dimensional Flows in a Water-Jet Axial Flow Pump. Proceedings of ASME 2005 Fluids Engineering Division Summer Meeting, pp. 1573-1581.

[11] Gao, H., Lin, W. L. and Du, Z. H. (2008). Numerical Flow and Performance Analysis of a Water-Jet Axial Flow Pump. Ocean Engineering, 35(16), pp. 1604-1614.

[12] Wieselthaler, G. M., Schima, H., Hiesmayr, M., Pacher, R., Laufer, G., Noon, G. P., DeBakey, M. and Wolner, E. (2000). First Clinical Experience with the DeBakey VAD Continuous-Axial-Flow Pump for Bridge to Transplantation. Circulation, 101(4), pp. 356-359.

[13] Mitamura, Y., Nakamura, H., Okamoto, E., Yozu, R., Kawada, S. and Kim, D. W. (1999). Development of the Valvo Pump: an Axial Flow Pump Implanted at the Heart Valve Position. Artificial Organs, 23(6), pp. 566-571.

[14] Brennen, C. E. (2013). Cavitation and Bubble Dynamics. Cambridge University Press.

[15] Saito, Y. and Sato, K. (2003). Cavitation Bubble Collapse and Impact in the Wake of a Circular Cylinder. Proceedings of the Fifth International Symposium on Cavitation (CAV2003), Cav03-GS-11-004.

[16] Xu, J., Tan, C. Q., Chen, H. S., Zhu, Y. L. and Zhang, D. Y. (2009). Influence of Tip Clearance on Performance of a Contra-Rotating Fan, Journal of Thermal Science, 18(3), pp. 207-214.

[17] Li, Q. B., Piechna, J. and Müller, N. (2011). Design of a Novel Axial Impeller as a Part of Counter-Rotating Axial Compressor to Compress Water Vapor as Refrigerant. Applied Energy, 88(9), pp. 3156-3168.

[18] Grassi, D., Brizzolara, S., Viviani, M., Savio, L. and Caviglia, S. (2011). Design and Analysis of Counter-Rotating Propellers-Comparison of Numerical and Experimental Results. Journal of Hydrodynamics, 22(5), pp. 570-576.

[19] Sharma, P. B., Jain, Y. P. and Pundhir, D. S. (1988). A Study of Some Factors Affecting the Performance of a Contra-Rotating Axial Compressor Stage. Proceedings of the Institution of Mechanical Engineers, Part A: Journal of Power and Energy, 202(1), pp. 15-21.

[20] Sharma, P. B., Pundhir, D. S. and Chaudhry, K. K. (1991). A Study of Aeroacoustic Performance of a Contra-Rotating Axial Flow Compressor Stage. Defence Science Journal, 41(2), pp. 165-180.

[21] Pundhir, D. S. and Sharma, P. B. (1992). A Study of Aerodynamic Performance of a Contra Rotating Axial Compressor Stage. Defence Science Journal, 42(3), pp. 191-199.

[22] Chen, Y. Y., Liu, B., Xuan, Y. and Xiang, X. R. (2008). A Study of Speed Ratio Affecting the Performance of a Contra-Rotating Axial Compressor. Proceedings of the Institution of Mechanical Engineers, Part G: Journal of Aerospace Engineering, 222(7), pp. 985-991.

[23] Knapke, R. D., Turner, M. G., List, M. G., Galbraith, D. S., Beach, T. and Merchant, A. A. (2008). Time Accurate Simulations of a Counter-Rotating Aspirated Compressor. Proceedings of ASME Turbo Expo 2008: Power for Land, Sea, and Air, pp. 481-496.

[24] Schimming, P. (2003). Counter Rotating Fans – an Aircraft Propulsion for the Future? Journal of Thermal Science, 12(2), pp. 97-103.

[25] Lengyel-Kampmann, T., Bischoff, A., Meyer, R. and Nicke, E. (2012). Design of an Economical Counter Rotating Fan: Comparison of the Calculated and Measured Steady and Unsteady Results. Proceedings of ASME Turbo Expo 2012: Turbine Technical Conference and Exposition, pp. 323-336.

[26] Hanson, D. B. (1985). Noise of Counter-Rotation Propellers. Journal of Aircraft, 22(7), pp. 609-617.

[27] Hubbard, H. H., (1948). Sound from Dual-Rotating and Multiple Single-Rotating Propellers. NACA TN 1654.

[28] Woodward, R. P. (1990). Noise of a Simulated Installed Model Counter Rotation Propeller at Angle-of-Attack and Takeoff/Approach Conditions. AIAA Paper No. 1990-0283.

[29] Woodward, R. P. (1992). Noise of Two High-Speed Model Counter-Rotation Propellers at Takeoff/Approach Conditions. Journal of Aircraft, 29(4), pp. 679-685.

[30] Polacsek, C. and Barrier, R. (2007). Numerical Simulation of Counter-Rotating Fan Aeroacoustics. AIAA Paper No. 2007-3680.

[31] Peters, A. and Spakovszky, Z. S. (2012). Rotor Interaction Noise in Counter-Rotating Propfan Propulsion Systems. ASME, Journal of Turbomachinery, 134(1), 011002.

[32] Schnell, R., Yin, J., Voss, C. and Nicke, E. (2012). Assessment and Optimization of the Aerodynamic and Acoustic Characteristics of a Counter Rotating Open Rotor. ASME, Journal of Turbomachinery, 134(6), 061016.

[33] Blandeau, V. P., Joseph, P. F. and Tester, B. J. (2009). Broadband Noise Prediction from Rotor-Wake Interaction in Contra-Rotating Propfans. AIAA Paper No. 2009-3137.

[34] Shigemitsu, T., Fukutomi, J. and Okabe, Y. (2010). Performance and Flow Condition of Small-Sized Axial Fan and Adoption of Contra-Rotating Rotors. Journal of Thermal Science, 19(1), pp. 1-6.

[35] Nouri, H., Ravelet, F., Bakir, F., Sarraf, C. and Rey, R. (2012). Design and Experimental Validation of a Ducted Counter-Rotating Axial-Flow Fans System. ASME, Journal of Fluids Engineering, 134(10), 104504.

[36] Chen, B. Y. –H. and Reed, A. M. (1990). A Design Method and an Application for Contrarotating Propellers. DTIC-90/003. David Taylor Research Centre, Bethesda, U. S. A.

[37] Van Gunsteren, L. A. (1971). Application of Momentum Theory in Counterrotating Propeller Design. International Shipbuilding Progress, 18(206), pp. 359-372.

[38] Caster, E. B. and LaFone, T. A. (1975). A Computer Program for the Preliminary Design of Contrarotating Propellers. David W. Taylor Naval Ship Research and Development Centre. No. SPD-596-01.

[39] Chen, B. Y. -H. and Reed, A. M. (1988). A Lifting-Surface Program for Contrarotating Propellers. Symposium on Hydrodynamic Performance Enhancement for Marine Applications, NUSC, Newport, RI, pp. 57-68.

[40] Sasaki, N., Murakami, M., Nozawa, K., Soejima, S., Shiraki, A., Aono, T., Fujimoto, T., Funeno. I., Ishii, N. and Onogi, H. (1998). Design System for Optimum Contra-Rotating Propellers. Journal of Marine Science and Technology, 3(1), pp. 3-21.

[41] Laskos, D. (2010). Design and Cavitation Performance of Contra-Rotating Propellers. Master Thesis, Massachusetts Institute of Technology.

[42] Furukawa, A., Cao, Y., Okuma, K. and Watanabe, S. (2000). Experimental Study of Pump Characteristics of Contra-Rotating Axial Flow Pump. Proceedings of 2nd International Symposium on Fluid Machinery and Fluid Engineering, Beijing, China, pp. 245-252.

[43] Kanemoto, T., Kimura, S., Ohba, S. and Satoh, M. (2000). Smart Control of Axial Flow Pump Performances by Means of Counter-Rotating Type: (1st Report, Counter-Rotating Type and Performances) [in Japanese], 66(651), pp. 2927-2933.

[44] Shigemitsu, T., Takano, T., Furukawa, A., Okuma, K. and Watanabe, S. (2005). Pressure Measurement on Casing Wall and Blade Rows Interaction of Contra-Rotating Axial Flow Pump. Journal of Thermal Science, 14(2), pp. 142-149.

[45] Furukawa, A., Shigemitsu, T. and Watanabe, S. (2007). Performance Test and Flow Measurement of Contra-Rotating Axial Flow Pump. Journal of Thermal Science, 16(1), pp. 7-13.

[46] Momosaki, S., Usami, S., Okuma, K., Watanabe, S. and Furukawa, A. (2010). Experimental Study on Rotational Speed Control of Contra-Rotating Axial Flow Pump. Proceedings of 3rd Asian Joint Workshop on Thermophysics and Fluid Science, Matsue, Japan.

[47] Momosaki, S., Usami, S., Watanabe, S. and Furukawa, A. (2010). Numerical Simulation of Internal Flow in a Contra-Rotating Axial Flow Pump. IOP Conference Series: Earth and Environmental Science, 12(1), Paper No. 012046.

[48] Yamashita, S., Watanabe, S., Okuma, K., Shirasawa, K. and Furukawa, A. (2007). Flow Measurement at Partial Flow Rate with LDV around Rear Rotor of Contra-Rotating Axial Flow Pump. Proceedings of ASME/JSME 5th Joint Fluids Engineering Conference, Paper No. FEDSM2007-37467, pp. 909-914.

[49] Shigemitsu, T. (2005). Researches on the Internal Flow Properties and High Efficiency Design of the Contra-Rotating Axial Flow Pump [in Japanese]. Doctor Thesis, Kyushu University.

[50] Baker, R. C. (2005). Flow Measurement Handbook: Industrial Designs, Operating Principles, Performance, and Applications. Cambridge University Press.

[51] JISB8302-1990. Measurement Methods of Pump Discharge.

[52] Tropea, C., Yarin, A. L. and Foss, J. F. (Editors) (2007). Springer Handbook of Experimental Fluid Mechanics (Vol. 1). Springer.

[53] Treaster, A. L. and Yocum, A. M. (1978). The Calibration and Application of Five-Hole Probes. No. TM 78-10, Applied Research Laboratory, the Pennsylvania State University.

[54] Momosaki, S. (2011). Researches on the Internal Flow Structure and Different Rotational Speed Design of the Contra-Rotating Axial Flow Pump [in Japanese]. Master Thesis, Kyushu University.

[55] ANSYS, Inc. (2012). ANSYS CFX Introduction (Release 14.0).

[56] ANSYS, Inc. (2012). ANSYS CFX-Solver Modeling Guide (Release 14.0).

[57] Lighthill, M. J. (1945). A New Method of Two-Dimensional Aerodynamics Design. In RandM1111, Aeronautical Research Council.

[58] Ishihara, T. and Tahara, H. (1952). On Characteristics of Axial Flow Pump [in Japanese]. Transactions of the Japan Society of Mechanical Engineers, 18(66), pp. 131-136.

[59] Meauze, G. (1982). An Inverse Time Marching Method for the Definition of Cascade Geometry. Journal for Engineering for Power, 104(3), pp. 650-656.

[60] Zangeneh, M. (1991). A Compressible Three-Dimensional Design Method for Radial and Mixed Flow Turbomachinery Blades. International Journal for Numerical Methods in Fluids, 13(5), pp. 599-624.

[61] Zangeneh, M., Goto, A. and Harada, H. (1998). On the Design Criteria for Suppression of Secondary Flows in Centrifugal and Mixed Flow Impellers. ASME, Journal of Turbomachinery, 120(4), pp. 723-735.

[62] Nishiyama, T. (1998). Aerofoil Flow Dynamics [in Japanese]. Nikkan Kogyo Shimbun.

[63] Goto, A., Nohmi, M., Sakurai, T. and Sogawa, Y. (2002). Hydrodynamic Design System for Pumps Based on 3-D CAD, CFD, and Inverse Design Method. ASME, Journal of Fluids Engineering, 124(2), pp. 329-335.

[64] Goto, A. and Zangeneh, M. (2002). Hydrodynamic Design of Pump Diffuser Using Inverse Design Method and CFD. ASME, Journal of Fluids Engineering, 124(2), pp. 319-328.

[65] Watanabe, S., Momosaki, S., Usami, S. and Furukawa, A. (2011). Internal Flow and Limiting Streamlines Observations of Contra-Rotating Axial Flow Pump at Partial Flow Rate. International Journal of Fluid Machinery and Systems, 4(2), pp. 235-242.

[66] Tallman, J. and Lakshminarayana, B. (2001). Numerical Simulation of Tip Leakage Flows in Axial Flow Turbines, with Emphasis on Flow Physics: Part I—Effect of Tip Clearance Height. ASME, Journal of Turbomachinery, 123(2), pp. 314-323.

[67] Tallman, J. and Lakshminarayana, B. (2001). Numerical Simulation of Tip Leakage Flows in Axial Flow Turbines, with Emphasis on Flow Physics: Part II—Effect of Outer Casing Relative Motion. ASME, Journal of Turbomachinery, 123(2), pp. 324-333.

[68] Xiao, X. W., McCarter, A. A. and Lakshminarayana, B. (2001). Tip Clearance Effects in a Turbine Rotor: Part I—Pressure Field and Loss. ASME, Journal of Turbomachinery, 123(2), pp. 296-304.

[69] McCarter, A. A., Xiao, X. W. and Lakshminarayana, B. (2001). Tip Clearance Effects in a Turbine Rotor: Part II—Velocity Field and Flow Physics. ASME, Journal of Turbomachinery, 123(2), pp. 305-313.

[70] Kameier, F. and Neise, W. (1997). Rotating Blade Flow Instability as a Source of Noise in Axial Turbomachines. Journal of Sound and Vibration, 203(5), pp. 833-853.

[71] Yamamoto, A., Matsunuma, T., Ikeuchi, K. and Outa, E. (1994). Unsteady Endwall/ Tip-Clearance Flows and Losses due to Turbine Rotor-Stator Interaction. ASME Paper No. 94-GT-461.

[72] Ottavy, X., Trébinjac, I., Vouillarmet, A. and Arnaud, D. (2003). Laser Measurements in High Speed Compressors for Rotor-Stator Interaction Analysis. Journal of Thermal Science, 12(4), pp. 310-317.

[73] Estevadeordal, J., Gogineni, S., Copenhaver, W., Bloch, G. and Brendel, M. (2000). Flow Field in a Low-Speed Axial Fan: a DPIV Investigation. Experimental Thermal and Fluid science, 23(1), pp.11-21.

[74] Tyler, J. M. and Sofrin, T. G. (1962). Axial Flow Compressor Noise Studies. Transactions of the Society of Automotive Engineers, 70, pp. 309-332.

[75] Zobeiri, A., Kueny, J. L., Farhat, M. and Avellan, F. (2006). Pump-Turbine Rotor-Stator Interactions in Generating Mode: Pressure Fluctuation in Distributor Channel. Proceedings of 23th IAHR symposium, pp. 1-10.

[76] Rodriguez, C. G., Egusquiza, E. and Santos, I. F. (2007). Frequencies in the Vibration Induced by the Rotor Stator Interaction in a Centrifugal Pump Turbine. ASME, Journal of Fluids Engineering, 129(11), pp. 1428-1435.

[77] Shur, M., Spalart, P. R., Strelets, M. and Travin, A. (1999). Detached-Eddy Simulation of an Airfoil at High Angle of Attack. Engineering Turbulence Modeling and Experiments, 4, pp. 669-678.

[78] Jang, C. S., Ross, J. C. and Cummings, R. M. (1998). Numerical Investigation of an Airfoil with a Gurney Flap. Aircraft Design, 1(2), pp. 75-88.

List of publications in journals/conference proceedings

Linlin Cao, Satoshi Watanabe, Simpei Momosaki, Toshiki Imanishi, Akinori Furukawa. (2013). Low Speed Design of Rear Rotor in Contra-Rotating Axial Flow Pump, International Journal of Fluid Machinery and Systems, 6(2), pp. 105-112.

Linlin Cao, Satoshi Watanabe, Toshiki Imanishi, Hiroaki Yoshimura, Akinori Furukawa. (2013). Experimental Analysis of Flow Structure in Contra-Rotating Axial Flow Pump Designed with Different Rotational Speed Concept, Journal of Thermal Science, 22(4), pp. 345-351.

Linlin Cao, Satoshi Watanabe, Toshiki Imanishi, Hiroaki Yoshimura, Akinori Furukawa. (2013). Blade Rows Interaction in Contra-Rotating Axial Flow Pump Designed with Different Rotational Speed Concept, IOP Conference Series: Materials Science and Engineering, 52(2), 022004. IOP Publishing.

Linlin Cao, Satoshi Watanabe, Hironori Honda, Hiroaki Yoshimura, Akinori Furukawa. (2014). Experimental Investigation of Blade-To-Blade Pressure Distribution in Contra-Rotating Axial Flow Pump, International Journal of Fluid Machinery and Systems, 7(3) (in press).

Linlin Cao, Hironori Honda, Hiroaki Yoshimura, Satoshi Watanabe, Akinori Furukawa. (2014). Experimental Investigation of Blade Rows Interactions in Contra-Rotating Axial Flow Pump, Proceedings of ASME 2014 4th Joint US-European Fluids Engineering Division Summer Meeting, Chicago, Illinois, FEDSM2014-21901 (in press).